1990

Microstructural evolution and control in the directional solidification of Fe-C-Si alloys

Jang-Sik Park
Iowa State University

Order Number 9100492

Microstructural evolution and control in the directional solidification of Fe-C-Si alloys

Park, Jang-Sik, Ph.D.

Iowa State University, 1990

U·M·I
300 N. Zeeb Rd.
Ann Arbor, MI 48106

Microstructural evolution and control in the directional solidification of Fe-C-Si alloys

by

Jang-Sik Park

A Dissertation Submitted to the
Graduate Faculty in Partial Fulfillment of the
Requirements for the Degree of
DOCTOR OF PHILOSOPHY

Department : Materials Science and Engineering
Major : Metallurgy

Approved :

Signature was redacted for privacy.

In Charge of Major Work

Signature was redacted for privacy.

For the Major Department

Signature was redacted for privacy.

For the Graduate College

Iowa State University
Ames, Iowa

1990

TABLE OF CONTENTS

GENERAL INTRODUCTION

There are four main types of cast irons each of which is characterized by a distinctive microstructure; gray, ductile, white and malleable cast iron. Cast irons are essentially ternary alloys of Fe-C-Si of near eutectic composition. The microstructure of cast irons, consisting of a carbon-rich phase in an iron-rich phase, is determined by the type of the C-rich phase. The C-rich phase is graphite in all of the cast irons except white iron, where it is Fe_3C. With the exception of the malleable iron where the graphite is formed by heat treatment in the solid state, the structure control of cast iron is mostly accomplished during the solidification. In general, the solidification rate determines the way the C is precipitated out of the molten cast iron; Fe_3C at high rates and graphite at low rates. The transition rate shows a variation depending on the melt chemistry. For example, the Si added in cast iron substantially raises the solidification rate required to produce white iron and encourages the precipitation of graphite over the Fe_3C in solidification. When the cast iron solidifies by precipitating the C in the form of graphite, the graphite phase takes on various morphologies according to the solidification velocity, temperature gradient and chemical composition. If the cast iron melt is specially treated by a small amount of either Mg or Ce the graphite is formed in the shape of spheres and the iron so produced is usually called ductile cast iron. Without such special melt-treatment, the formation of flake graphite dominates over Fe_3C formation during solidification, thereby producing the gray cast iron. The flake graphite is precipitated in the form of either coarse type A at low solidification rates or fine type D at high rates. When the gray iron contains less impurities such as S and Te, coral graphite starts to precipitate, replacing the type D graphite which appears in commercial purity cast irons. The coral graphite has the fine size as type D but appears as more of a highly branched rod structure as opposed to a branched plate structure of type D

graphite. The solidification microstructure of cast iron is, therefore, strongly affected by the solidification conditions and chemical compositions.

This study focuses its effort on evaluating the effect of the elements S, Te, H and O on structure control in the directional solidification of Fe-C-Si alloys. The introduction of directional solidification techniques provides a close control over solidification atmosphere, velocity and composition, and the effect of trace elements under various solidification conditions can be better investigated. In Part I of this study, the S addition is applied to the parent high purity alloys in order to examine the effect caused by the S on the solidification microstructure. In the course of this study, it has been discovered that enriching the solidification atmosphere with hydrogen or oxygen gases apparently increases the activity of the corresponding element in molten cast iron and produces some interesting effects on the transition rates between the various graphite morphologies.

The mechanism by which the trace elements produce such a dramatic effect on the structure of cast iron has often been postulated to involve the selective adsorption of these elements during growth into the liquid, thereby reducing growth rate and allowing a different growth form to dominate. Part II of this study has utilized scanning Auger spectroscopy to study this possibility. The Auger study examines the iron/graphite interface exposed on the fracture surface of the Fe-C-Si alloys directionally solidified in Part I.

The morphological selection of graphite is in many respects considered to be determined by the growth behavior of graphite itself, although the presence of the metal phase, austenite, is not to be neglected. As an initial step to understand the growth behavior of graphite in the presence of S or Te, the graphite crystals themselves grown at various solidification velocities, were carefully examined in Part III of this study by optical microscopy, transmission and scanning electron microscopy. Several studies have already

demonstrated in type A flake graphite the occurrence of structural defects such as twin boundaries and rotation stacking faults around a specific direction of graphite crystals, and the fault formation is believed to play an important role in graphite growth. This study extends the investigation to other structures such as type D flake and coral graphite.

The experimental results in Part I, suggesting that the interaction between H and O plays an important role in modifying the microstructure in gray solidification, initiated another set of interesting experiments. It has long been an unsolved problem to explain how the H improves the ability of Te to suppress the formation of gray structures. In view of the tendency of Te to react with O, it also seems necessary to investigate the possible interaction of H with O which may reduce the O activity in the white solidification of Te-added Fe-C-Si alloys. In experiments with no control over the solidification atmosphere, it is extremely difficult to estimate the effects caused by these reactive gaseous elements, O and H, dissolved in melt. In Part IV of the present study, directional solidification studies were done under controlled H_2 and O_2 conditions to study the H_2 effect.

PART I. EFFECT OF S, H AND O ON STRUCTURE CONTROL IN THE DIRECTIONAL SOLIDIFICATION OF Fe-C-Si ALLOYS

INTRODUCTION

The elements S, H and O, although present in trace amount, exert a powerful influence on cast iron microstructures and their presence is difficult to avoid in the solidification of cast iron. It has long been an important subject in cast iron solidification to understand how those trace elements bring about the structural modification. In more conventional experiments where cast iron solidification proceeds by nucleation and growth of eutectic cells, the S increases the eutectic cell number and the spacing between graphite flakes (1,2). The coarser structure is, in general, attributed to the increased cell number in high S alloys which reduces the actual cell growth rate. Because of its small distribution coefficient in austenite, S is also known to increase the melt undercooling. The effect of H and O was also examined in conventional experiments (1,3). Hydrogen shows an effect similar to S in coarsening the gray structures. Hydrogen, however, has no effect on the eutectic cell number. The effect of O has been usually considered by focusing its influence on the nucleation characteristics. It was reported that the increased O content in cast iron melt increases the eutectic cell number. Oxygen is also known to promote the formation of coral graphite (4). It is difficult in conventional casting experiments to gain a true appreciation of the effect of the trace elements on structure control. Solidification microstructures in castings depend heavily on nucleation characteristics as well as on growth. The trace elements in cast iron usually have influences on both nucleation and growth, and the effect of each individual element can be appreciated only if its effect on both stages of solidification, nucleation and growth, is independently investigated. It is also necessary to investigate the effect of a given element separately as well as in connection with other elements through the strict control over the solidification conditions.

With the introduction of directional solidification techniques which provide a close control over solidification atmosphere, velocity and composition, the effect of minor

elements under different solidification conditions could be investigated in a more systematic way. In directional solidification more attention can be paid to growth effects since nucleation characteristics are not important when the eutectic growth occurs maintaining a planar interface. In addition, control of the solidification atmosphere makes it possible to examine the mutual interaction of the trace elements with the reactive gaseous elements O and H. There have been quite a few experimental results reported of the effect of S on structure in the directional solidification of cast iron (5,6,7). However, reported attempts are very rare of the role played by H and O in directional solidification. The present study is to investigate the effect of S and H and their interaction with O on the microstructural modifications in the gray structures of Fe-3.4C-2Si alloys utilizing the directional solidification techniques.

It has been established in the previous studies that the S addition induces type D graphite at higher solidification velocities instead of coral graphite which occurs in high purity Fe-C-Si alloys (8). Experimental results of the S effect , however, do not agree on the spacing between graphite flakes. Sayama and coworkers (7) found a remarkable decrease in intergraphite spacing when a small amount of S is added, but no more change upon further increasing the S content. Their experiments were carried out directionally in air. The possible decrease in the interfacial energy due to the S presence was considered to be responsible for the decrease in graphite spacing. They also observed that the S addition increases the branching frequency of graphite. The experimental results reported by Nieswaag and Zuithoff (5) contradict with those by Sayama and coworkers. They found coarsening in the gray structure of type A flake graphite when S is added up to 0.02 wt. %, above which the coarsening effect levels off. The S effect was strictly distinguished in type A and D structures. The amount of S addition has a negligible effect on type D as long as the alloy contains sufficient S content to produce the D graphite instead of coral at higher

rates. Their experiments were performed under an Ar environment. The coarsening of type A gray structure in S-added alloys was explained by assuming that the branching ability of graphite flakes would be reduced due to the S presence. On the other hand, Lux and Kurz (6) reported that S has no significant effect on the graphite spacing. Recently Magnin and Kurz (9) observed a significant increase in the graphite spacing in Fe-C alloys containing 100 ppm S.

It appears that the previous experimental results were obtained and interpreted with not much consideration on the effect of O. The present study produced an indication that O could play an important role in control of the microstructures in the directional solidification of Fe-C-Si alloys. This study was successful in raising the O or H content in the melt by enriching the solidification atmosphere with the gaseous element of interest. It was verified through the control of the alloy composition and solidification atmosphere that the O interacts with the trace element S, and also that the increased H content causes the O effect to be less pronounced by probably reducing the O activity in the melt. The experimental results obtained from directional solidification will be presented first to see the microstructural modifications induced by S and H. The Auger fracture analysis with the directionally solidified samples will be subsequently presented in Part II to discuss the possible S-O interaction. Another experimental results suggesting the H-O interaction will also be provided in Part IV.

EXPERIMENTAL TECHNIQUE

Alloys were made to a target composition of Fe-3.4 wt. % C-2.0 wt. % Si with and without 0.02 wt. % S, using Glidden electrolytic iron, specified 99.9 % Fe, a semiconductor grade Si and spectrographic grade carbon rod. A 1 to 1.5 kg master alloy of Fe-C-Si or Fe-C-Si-S was first prepared by chill casting from an Al_2O_3 crucible (Norton AN299A, 99.5 % Al_2O_3). Complete liquid mixing was produced by using 3 kHz induction heating with a power surge to 1550°C followed by cooling to pour from a 100°C superheat under an Ar atmosphere.

Rods for directional solidification were prepared as follows. The master alloys were placed in Al_2O_3 crucible and heated with the 3 kHz induction power converter under vacuum to 1000°C, and Ar was admitted to a pressure of 684 torr. The charge was then melted and held for approximately 10 min. at 100°C superheat. Then a vertical array of 9 quartz tubes of 4.5 mm inside diameters were lowered so that their bottom ends penetrated well below the melt surface. The upper ends of the tubes were sealed into a fixture with an epoxy cement and connected to a vacuum pump through a quick release valve. Immediately after lowering into the melt the quick release valve was opened causing the melt to be drawn up into the 9 quartz tubes to a height of about 40 cm. The rods were then raised above the melt surface and solidified.

The directional solidification experiments were carried out in hard fired high purity Al_2O_3 tubes of 5 mm inside diameter in the arrangements shown schematically in Fig. 1. The lower end of the Al_2O_3 tube was closed and the upper end was O-ring sealed to a head which allowed vacuum/atmosphere control and a vertical thermocouple or probe to be inserted into the melt. The Pt/Rh resistance wound furnace melted the alloy down to a point near the top of the copper cooling finger assembly. The carriage supporting the furnace plus cooling assembly was moved upward on three ball bushing guided rods

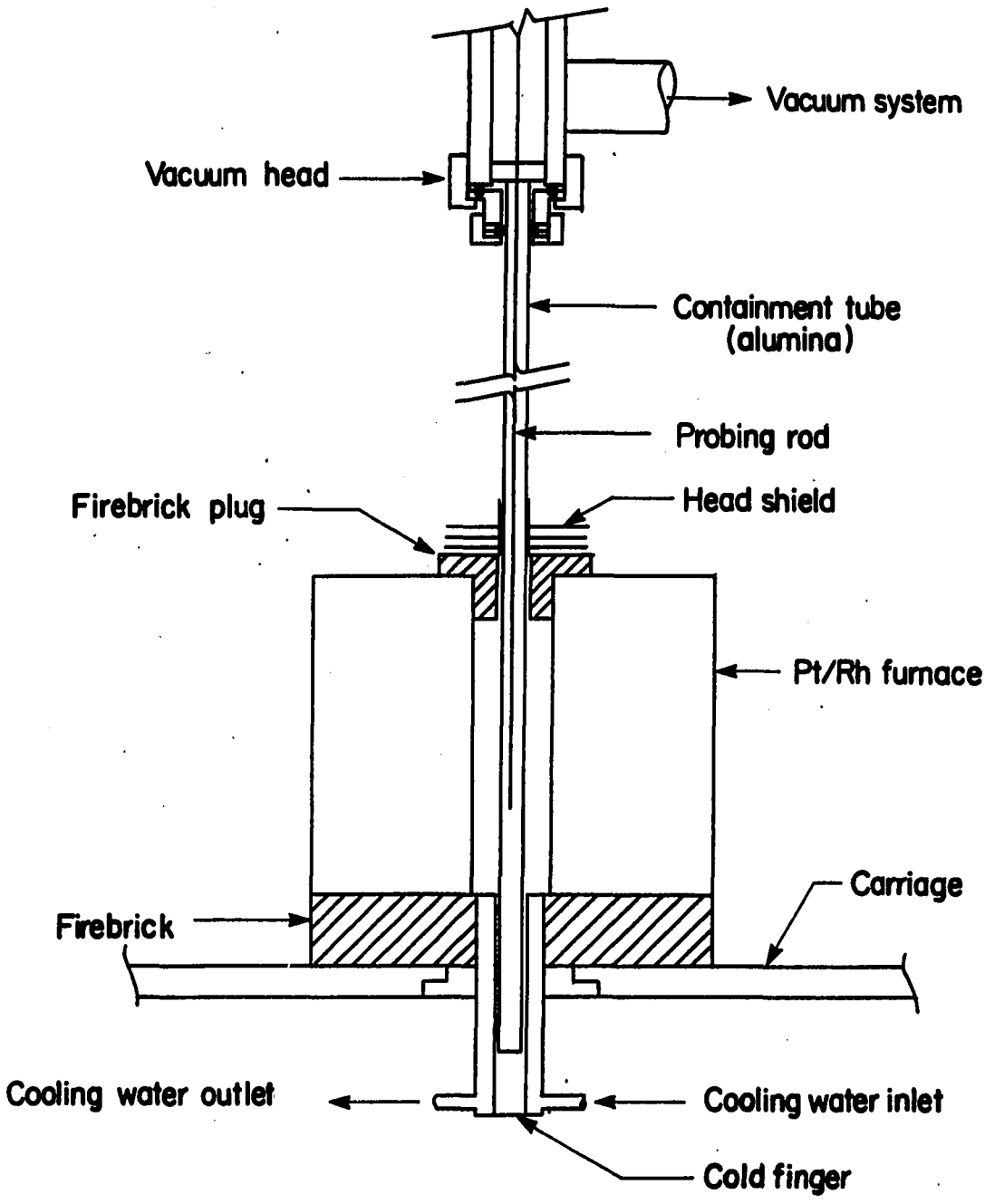

Figure 1. Schematic diagram of directional solidification arrangement

driven from below by two symmetrically placed ball screw rods which were turned by a synchronous stepper motor using a belt drive. The rate of motion was computer controlled.

Considerable difficulty was encountered with cavity porosity which resulted from bubble formation when the charge rods initially melted within the Al_2O_3 tube. This problem was reduced by the following procedure. After melting the alloy down to the desired point under 690 torr Ar, which required a furnace temperature of 1450°C, a thin, 1.5 mm diameter, Al_2O_3 tube was slowly lowered to the melt interface and raised again. Repeating this procedure twice at 10 min. interval was effective at reducing porosity. Several experiments were also done in which this procedure was carried out under vacuum followed by introduction of Ar. This technique provided vacuum degassing of the melt, but it was only nominally superior for eliminating cavity porosity, and was much more difficult to perform without tube breakage due to liquid metal blow-up into the cold portions of the Al_2O_3 tube when the vacuum was applied.

Experiments were also performed under controlled atmospheres of 10 volume % H_2 or O_2 plus balance Ar instead of pure Ar to investigate the effect of the increased H or O content on the solidification microstructure.

An experiment consisted of initial melt down followed by probing and then a 10 min. hold to stabilize the initial interface position. Three types of experiments were carried out, acceleration, deceleration and temperature profile experiments. In the acceleration experiments the velocity was started at 1 um/s and then accelerated in steps up to 100 um/s. The experiments were terminated by loosening the holding ring at the top of the Al_2O_3 containment tube and dropping the tube into a vertical chamber containing flowing water which produced a rapid quench. After breaking away the Al_2O_3 tube a flat was ground longitudinally on the samples using a surface grinding machine. Metallographic polishing

and etching revealed the location of the interfaces where the rate was increased stepwise and using these as fiducial marks the solidification velocity at any region was determined from the record of the carriage velocity. Differences in initial and final interface positions for each solidification rate agreed reasonably well with differences in initial and final carriage positions for the given rate. The deceleration experiments began by starting the experiments at velocities of around 100 um/s and then reducing the velocity in steps down to 1 um/s. The temperature profile experiments were done at constant velocity. The thermocouples were made from Pt-6 % Rh/Pt-30 % Rh wire of 127 um in diam. contained in 1.5 mm O.D. Al_2O_3 tubes. The output of the thermocouple was continuously recorded both on a chart recorder and by a digital voltmeter connected to a data acquisition system, as the solid/liquid region passed the thermocouple tip. The temperature gradients in the solid and liquid were evaluated by measuring the slope of the temperature curve at the interface.

RESULTS

The effect of S and the two reactive gaseous elements H and O on structure control, particularly on graphite morphologies, was investigated in the directional solidification of Fe-3.4C-2Si alloys. The S effect was evaluated by comparing the resulting graphite morphologies solidified from two alloys differing only in the S content, alloys of high purity with no intentional S addition and alloys with the addition of 0.02 wt.% S. Chemical compositions were evaluated by several techniques. Spark source mass spectrometry determined the major impurity elements in the high purity alloys to have the following average values; Ge-0.005, Ni-0.003, Co-0.002, S-0.002, Cu-0.002 and P-0.002 wt.%. Carbon was determined by combustion analysis to vary from 3.28 to 3.39 wt.%, which is a bit lower than the target composition of 3.4 wt.%. The Si content was determined by wet chemical analysis to be constant at 1.98 wt.% (target composition = 2.0 wt.%). The S content in the S-added alloys was also determined by wet chemical analysis in two directionally solidified rods to have the average value of 0.026 wt.% (target composition = 0.02 wt.%). The effect of H or O on the graphite morphologies of the high purity and the S-added alloys was evaluated by increasing the H_2 or O_2 concentration in the solidification atmosphere. The H_2- or O_2-rich atmosphere was provided by filling the sample containment tube with 10 volume % H_2 or O_2 plus balance Ar gases when the furnace temperature reached 1000°C. Most experiments in the present study were carried out under pure Ar gas atmosphere.

Table 1 presents the results obtained from experiments with the high purity alloys in the deceleration of solidification velocities. Consider experiment JP1-17-2 run under pure Ar atmosphere to illustrate the rate sequence information. The controlled solidification was begun at 100 um/s for 20 mm and then the rate was decreased in steps down to 1 um/s after a certain length, indicated in the parentheses, was solidified at the given rate. The

Table 1. Experimental results with Fe-3.4C-2Si alloys in the deceleration of solidification velocities

Expt.#	Rate Sequence Information Rate in um/s (Run Dist. in mm)	Atmosphere	Coral⇒A Tran.[um/s]
JP1-17-1	10(25)-5(25)-2.5(20)-1(20)	10% H_2+Ar	>10
JP1-17-2	100(20)-50(20)-10(20)-5(20)-2.5(20)-1(10)	Ar	2.5
JP1-17-3	50(20)-10(20)-5(20)-2.5(15)-1(10)	Ar	2.5
S00-1	50(25)-10(25)-5(25)-2.5(22)	10% H_2+Ar	10-50
S00-2	50(25)-10(25)-5(25)-2.5(20)	Ar	2.5
S00-3	100(15)-50(15)-10(20)-5(20)-2.5(15)-1(10)	10% H_2+Ar	10-50
S00-10	150(20)-100(20)-50(15)-10(15)-5(15)-2.5(15)-1(10)	10% O_2+Ar	1

Table 2. Experimental results with Fe-3.4C-2Si alloys in the acceleration of solidification velocities

Expt.#	Rate Sequence Information Rate in um/s (Run Dist. in mm)	Atmosphere	A⇒Coral Tran.[um/s]
JP1-17-4	1(15)-2.5(15)-5(20)-50(20)	Ar	2.5-5
JP1-17-5	1(15)-2.5(15)-5(20)-50(20)	Ar	2.5-5
S00-4	1(10)-2.5(20)-5(15)-10(15)-50(20)-100(20)	Ar	2.5-5
S00-5	1(10)-2.5(20)-5(15)-10(15)-50(20)-100(20)	Ar	2.5
S00-8	1(10)-2.5(20)-5(20)-10(15)-20(15)-50(15)-100(20)	10% H_2+Ar	20-50
S00-9	1(10)-2.5(20)-5(15)-10(15)-50(20)-100(20)	10% O_2+Ar	1-2.5

deceleration in rates induced the change in graphite morphologies from fine coral to coarse type A, at 2.5 um/s in this experiment. In all experiments with high purity alloys, the graphite took on the coral morphology at high solidification velocities, which transformed into type A flake graphite upon decreasing the velocity. Table 1 shows that the alloys undergo the coral⇒A transition consistently at 2.5 um/s in experiments run under the pure Ar atmosphere, experiments JP1-17-2 and 3 and S00-2, where pure Ar is used to fill the tube. When the atmosphere is enriched in O_2 concentration in experiment S00-10, the type A graphite formation is suppressed and the coral⇒A transition occurs at 1 um/s. On the contrary, the introduction of H_2-rich gases into the atmosphere is shown in experiments JP1-17-1, S00-1 and S00-3 to promote substantially the formation of type A graphite and the coral⇒A transition consistently occurs while the rate is decelerated from 50 to 10 um/s.

The experimental results with high purity alloys in acceleration of the solidification velocities are presented in Table 2. In acceleration experiments, for instance in experiment S00-4, the solidification was begun at 1um/s for 10 mm and then the rate was stepwise increased up to 100 um/s after a certain length, as indicated in the parentheses, was solidified. Therefore, type A graphite was first induced at lower rates and then transformed into coral morphology upon increasing the rates, at 2.5-5 um/s in this experiment. The effect of H or O on graphite morphologies in acceleration experiments is in general similar to that in deceleration experiments. Under pure Ar atmosphere, experiments JP1-17-4, JP1-17-5, S00-4 and 5, the alloys undergo the A⇒coral transition at 2.5-5 um/s. The O-rich atmosphere, experiment S00-9, suppresses the A formation and the transition occurs at 1-2.5 um/s. The atmosphere rich in H_2, however, promotes the A growth and raises the A⇒coral transition up to 20-50 um/s in experiment S00-8.

The S effect in deceleration experiments on the transition of graphite morphologies can be seen in Table 3. The transition in S-added alloys with the decreasing velocities

Table 3. Experimental results with Fe-3.4C-2Si-0.02S alloys in the deceleration of solidification velocities

Expt.#	Rate Sequence Information Rate in um/s (Run Dist. in mm)	Atmosphere	D⇒A Tran.[um/s]
S02-1	100(15)-50(15)-10(15)-5(15)-2.5(15)-1(10)	Ar	10-50
S02-3	100(15)-50(15)-10(15)-5(15)-2.5(15)-1(10)	Ar	10-50
S02-5	50(15)-40(15)-30(15)-20(15)-10(15)-5(15)	Ar	10-20
S02-6	100(15)-50(20)-30(15)-10(15)-5(15)-2.5(20)-1(10)	10% H_2+Ar	30
S02-10	100(20)-30(20)-20(15)-10(15)-5(15)-2.5(15)	10% H_2+Ar	20-30

Table 4. Experimental results with Fe-3.4C-2Si-0.02S alloys in the acceleration of solidification velocities

Expt.#	Rate Sequence Information Rate in um/s (Run Dist. in mm)	Atmosphere	A⇒D Tran.[um/s]
S02-2	1(10)-2.5(15)-5(15)-10(15)-50(15)-100(10)	Ar	>50
S02-4	5(5)-1(10)-2.5(15)-5(15)-10(15)-50(15)-100(15)	Ar	>50
S02-7	1(10)-2.5(20)-5(20)-10(15)-20(15)-50(15)-100(20)	10% H_2+Ar	>50
S02-9	1(10)-2.5(15)-5(15)-10(15)-20(20)-50(20)-100(20)	10% O_2+Ar	20-50

occurs between type D and A flake graphite instead of between coral and A which occurs in high purity alloys. The fine type D graphite initially induced at high rates transformed into coarse type A while the rate was decreased from 50 to 10 um/s under pure Ar atmosphere, experiments S02-1 and 3. The D⇒A transition rate under pure Ar atmosphere was more accurately determined in experiment S02-5 to be $10 < V_{D-A} < 20$ um/s. When the solidification occurred under H-rich atmosphere, experiments S02-6 and 10, the D⇒A transition occurred at 20-30 um/s. The results in acceleration experiments with the S-added alloys are presented in Table 4. Type A graphite was initially solidified and then it transformed into type D graphite with the increasing rate. Table 4 shows that the experiments were performed under three different solidification atmospheres, pure Ar, H-rich and O-rich. The A⇒D transition in both pure Ar , experiments S02-2 and 4, and H-rich atmosphere, experiment S02-7, occurred while the solidification velocity was accelerated from 50 to 100 um/s. When the O_2 gas was introduced, experiment S02-9, the alloys underwent the A⇒D transition at a little slower rate, 20-50 um/s. It appears that in S-added alloys the solidification atmosphere does not affect the graphite morphologies so much as in high purity alloys.

Table 5 summarizes the transition rates in six different conditions in deceleration and acceleration experiments using the data in Tables 1-4. Here the transition is between type A and coral in high purity alloys and between type A and D in S-added alloys. It is seen from Table 5 that the type A growth is maintained at higher solidification rates in the presence of S or H than in their absence. In deceleration experiments, type A graphite can grow up to 10-20 um/s in the presence of either element and up to 20-30 um/s when both elements were present simultaneously. In high purity alloys, however, type A stops growing at 2.5 um/s when solidified under pure Ar atmosphere. It is seen in acceleration experiments that type A can grow even at higher rates up to 20-50 um/s when S or H is

present compared to 2.5-5 um/s in high purity alloys under pure Ar atmosphere. In contrast to the effect of S or H, the increase in O content under O-rich atmosphere is shown in Table 5 to promote coral graphite down to 1 um/s. Type A graphite grows only at rates slower than 2.5 um/s. In S-added alloys, however, the O does not have a noticeable influence on graphite growth.

Table 5 Maximum rate [um/s] of type A growth versus alloy composition and solidification atmosphere

Composition	Atmosphere	In deceleration	In acceleration
High purity	10% O_2+Ar	1	1 - 2.5
	Ar	2.5	2.5 - 5
	10% H_2+Ar	10 - 20	20 - 50
0.02 wt.% S addition	10% O_2+Ar	N.I.[a]	20 - 50
	Ar	10 - 20	50
	10% H_2+Ar	20-30	50

[a]Not investigated.

Graphite morphologies in alloys with no S addition solidified at low and high rates under pure Ar atmosphere are presented in Fig. 2a and b. Type A flake graphite, Fig. 2a, growing at low rates transforms into coral graphite, Fig. 2b, at rates above 2.5 um/s in high purity alloys. In S added alloys, however, the transition is not between type A and coral but between type A and type D graphite. Figure 3 shows the type D undercooled graphite in S-added alloys solidified at 100 um/s under pure Ar atmosphere. Figures 4a-d present graphite morphologies solidified at 2.5 um/s in acceleration experiments under four

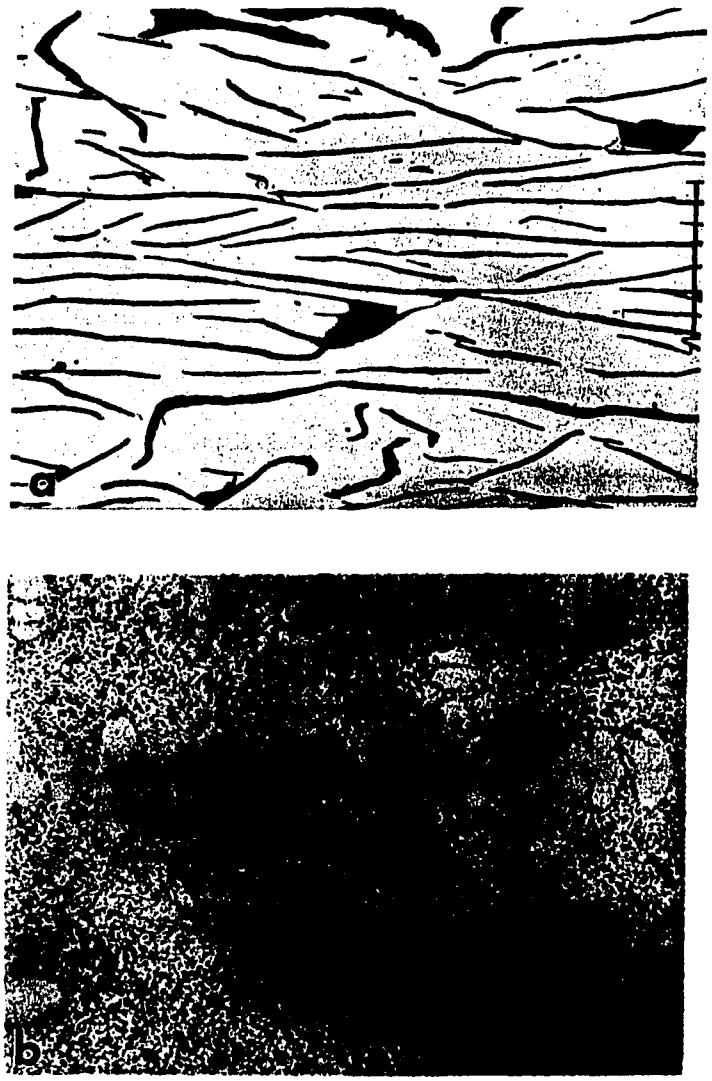

Figure 2. Optical Micrograph of graphite morphology in longitudinal section solidified from high purity alloys, (a) type A flake, 1 um/s, 100X, as polished, (b) coral graphite, 5 um/s, 100X, as polished. Solidification direction to the right

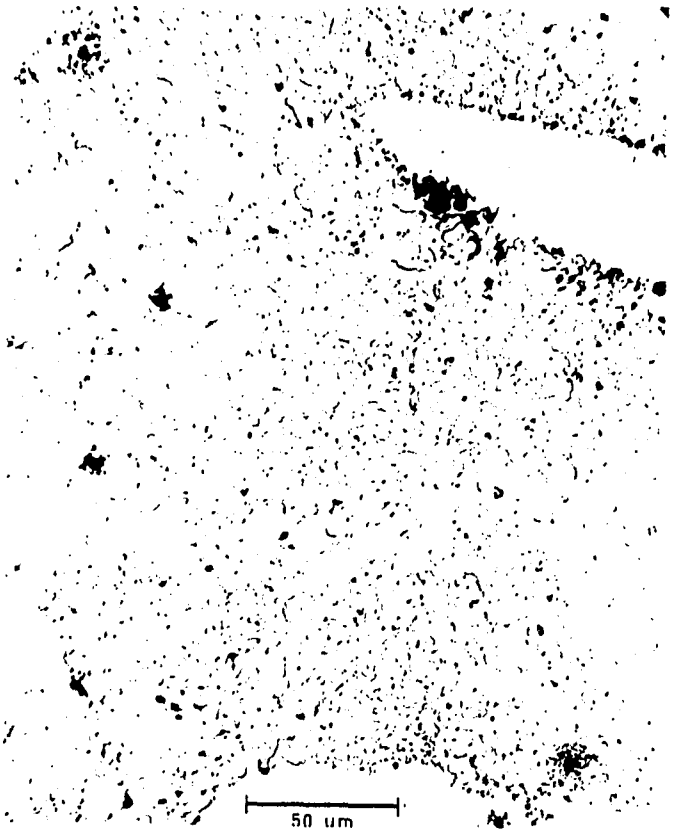

Figure 3. Optical micrograph of type D flake graphite in transverse section solidified at 100 um/s from S-added alloys, 500X, as polished

Figure 4. Optical micrograph of graphite morphologies in transverse section solidified at 2.5 um/s, 80X, as polished, (a) high purity under pure Ar atm., (b) high purity under 10% H_2+Ar atm., (c) S-added under pure Ar atm., (d) S-added under 10% H_2+Ar atm

different conditions. Another effect either S or H has on the gray structure is the coarsening in intergraphite spacing as can be seen in Figs. 4. The simultaneous presence of S and H causes type A growth to be maintained at slightly higher rates than the separate presence of either element. But the transition on increasing the velocity is between type A and D graphite, not coral.

Another set of experiments was carried out in order to investigate the degree of cooperation between iron and graphite in the solidification of flake graphite eutectic. Literature studies (10,11,12) often claim that the type A flake graphite grows ahead of the neighboring austenite iron phase whereas the theoretical work (13,14) currently available for the solidification of gray eutectic is based on a strict coupling of the three phases, iron, graphite and melt, at least, at the triple junctions. In these experiments, a radial-array water jet cold finger is used instead of the water cooled tube-in-tube cold finger which was mostly used in the rest of the experiments. The radial-array water jet cold finger uses a double o-ring to seal the alumina containment tube as it passes into the cold finger. An array of eight holes, arranged in a radial configuration, are directed to the center of the cold finger where the alumina tube passes. Water under pressure is forced through the holes and impinges on the surface of the alumina tube. In order to ensure a good quenching, a lever system is attached to the carriage and the carriage is raised rapidly upward in one quick motion, thereby plunging the solidification front into the water-spray zone. In experiments where the tube-in-tube cold finger is used, quenching is accomplished by dropping the alumina tube into the water quench bath positioned roughly 50 cm below. Accordingly, it is probable that the frozen interface does not represent the true solidification front because of the movement which may alter the condition at the front. In the new technique, it is the cold finger that moves in quenching, eliminating movement of the tube containing a solidifying sample. The quench interface morphology in three experiments

looked qualitatively the same and the typical result is shown in Figs. 5. Figure 5a shows the frozen solidification front at low magnification. The sample was growing at 1 um/s when it was quenched by the spraying water. A high magnification picture taken at area A of Fig. 5a is shown in Fig. 5b. Two interesting facts are observed. The flake is completely enveloped by the iron phase and the iron is pearlitic in structure at the boundaries facing the quenched structures. It seems likely that the complete enveloping of the growing flake by the iron phase has occurred as a result of the quenching effect since it is generally accepted that the flake graphite is developed directly from molten iron, not by diffusion through the solid iron phase. This view is supported by Fig. 5c, a higher magnification picture of area B of Fig. 5a. Area B is one of the proeutectic austenite dendrite arms growing ahead of the general growth front in alloys of hypoeutectic composition. The dendrite also shows the presence of pearlite structure at the boundaries facing the quenched white structure. In addition, small Fe_3C plates, which must have been formed on quenching, are observed to penetrate the dendrite at the boundaries. Figure 5d, a blow-up of the upper left corner of the dendrite, gives a better presentation of the Fe_3C plates, showing penetrations of 18-21 um into the iron phase. This suggests that the iron growth fronts have advanced around 20 um during quenching. (Note that the interface between the quenched melt and the iron phase appears to provide a good nucleation site for pearlite, inducing the pearlite growth inward around the boundary until it is stopped by the growing martensite.) There does not seem to be any method of evaluating how far the graphite flakes advance during the quench. Because of the faceted nature of the graphite growth front it seems unlikely that the flakes would grow as much as the iron during the quench. If, for example, the flakes only advanced 1 or 2 um on quenching, then the 20 um iron advance would be adequate to enclose the growth tips of the flakes, even if they protruded ahead of the iron phase by 10 to 15 um. Hence, the present quenching technique

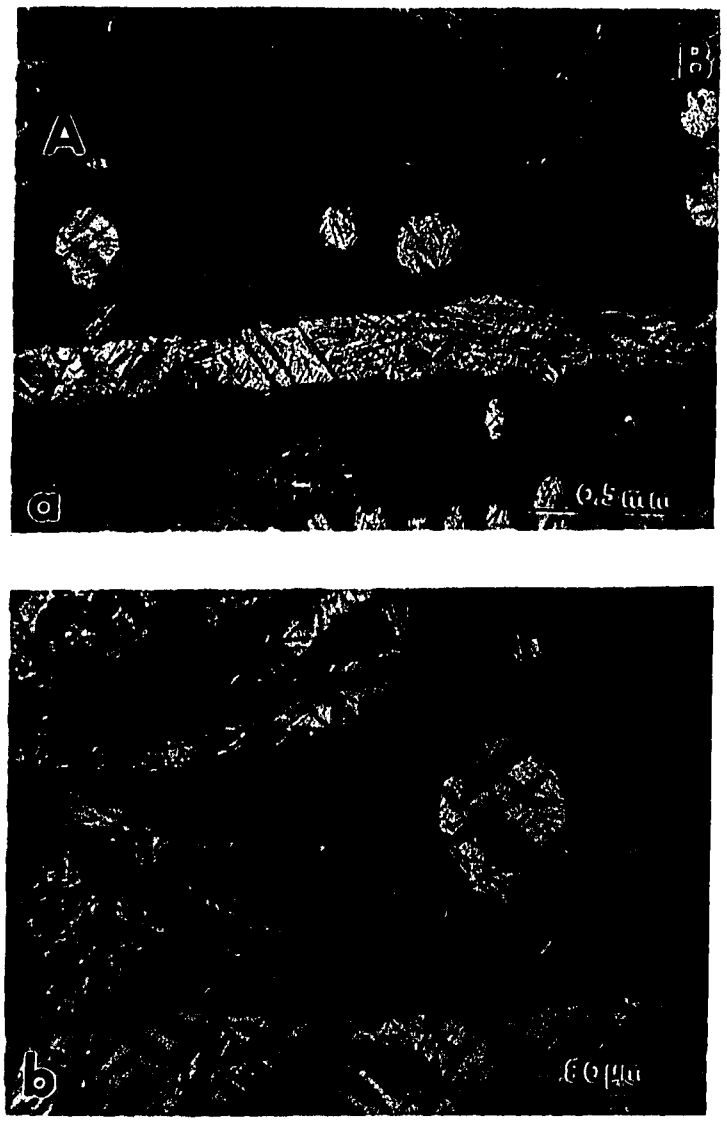

Figure 5. Optical micrographs of quenched solidification front of type A graphite cast iron. Solidification direction to the right, rate=1um/s, nital etch. (a) 50X, (b) region A of (a), 200X

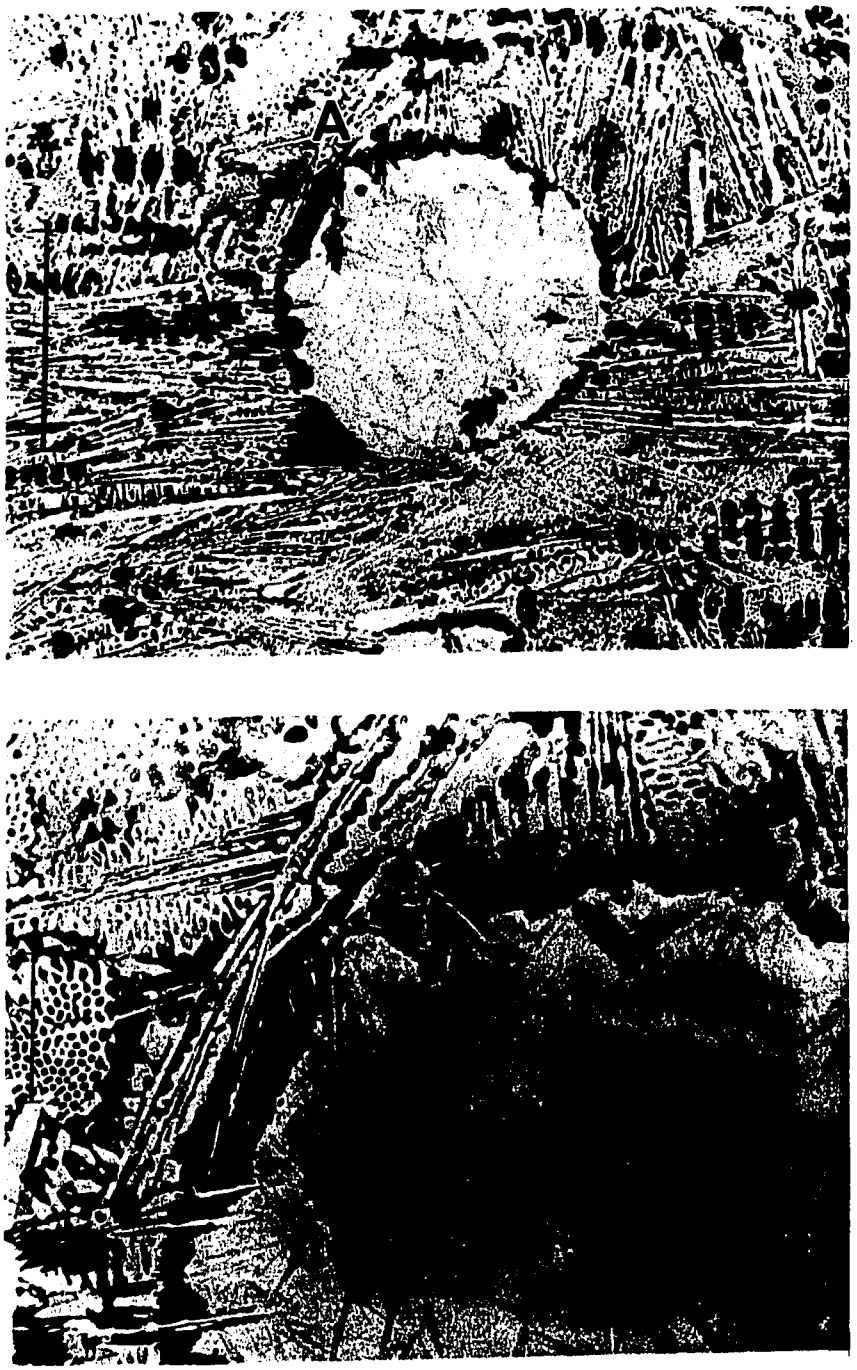

Figure 5. (continued) (c) region B of (a), 200X, (d) region A of (c), 800X

is not fast enough to settle the question of whether or not type A flakes grow in front of the iron phase or are coupled closely to it.

The result of temperature profiling experiments is summarized in Table 6. The temperature gradients in the liquid and solid at the solid/liquid interface solidifying at a given velocity are given in Table 6 with the furnace temperature stabilized at 1450°C. Assuming a unidirectional heat flow, which is a reasonable assumption for the directional solidification apparatus utilized in this study, the gradient in the liquid (G_l) is coupled to that in the solid (G_S) through the heat flux balance equation

$$k_S G_S = k_l G_l + L\rho V \qquad (1)$$

where L is the latent heat per unit mass, ρ is the density, V is the solidification velocity, and k_S and k_l are the thermal conductivities of the solid and liquid, respectively. Therefore the temperature gradient in the liquid at the interface is given as,

$$G_l = \frac{k_S}{k_l} G_S - \frac{L\rho V}{k_l} \qquad (2)$$

Equation (2) states that the gradients in liquid and solid are in general determined by the thermal conductivity ratio, $\frac{k_S}{k_l}$, at low solidification velocities where the latent heat effect represented by the last term in Eqn. (2) is negligible. The data in Table 6 were determined from measuring the slope of the temperature curve traced both on a chart recorder and by a data acquisition system, such as those presented in Figs. 6a and b, respectively. The curves in Figs. 6 show an apparent break in slope at around 1120°C as indicated by an arrow, locating the solid/liquid interface. The gradual, instead of a sharp, break in slope is understood if the thermocouple probe size, 1.2 mm in diam., and the interface morphology, which is dendritic at 100 um/s, are taken into account. However, the slope change at the interface is not that apparent in Figs. 7a and b, which were obtained at a low solidification rate, 5um/s, although a change, which is barely noticeable, has occurred at around 1127°C as indicated by an arrow. Equation (2) suggests that if the thermal

Table 6. Temperature gradient in liquid [G_l] and in solid [G_s] near the freezing solid/liquid interface versus solidification velocity [V] with the furnace temperature stabilized at 1450°C

V[um/s]	Expt.#	G_l[°C/cm]	G_s[°C/cm]
1	S00-13	86	86
	S00-15	93	93
5	S00-13	77	95
	S00-14	74	94
	S00-15	79	91
10	S00-13	79	89
	S00-14	75	93
	S00-15	86	99
20	S00-13	78	98
	S00-15	81	106
	S00-16	74	109
50	S00-15	64	95
	S00-16	64	95
75	S00-15	63	98
	S00-16	59	97
100	S00-15	64	122
	S00-16	62	119

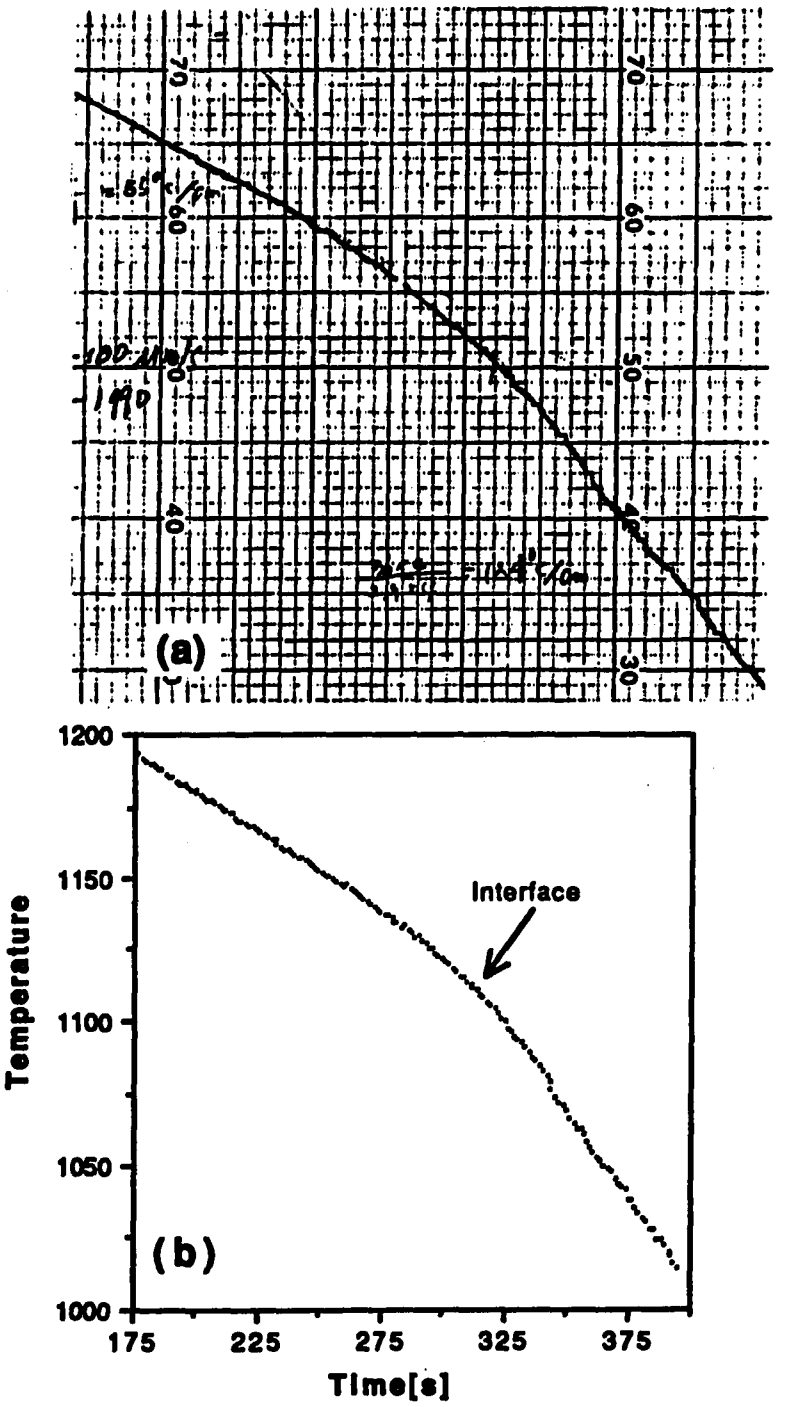

Figure 6. Result of the temperature profile experiment. Rate=100 um/s. (a) on a chart recorder, (b) on a data acquisition system

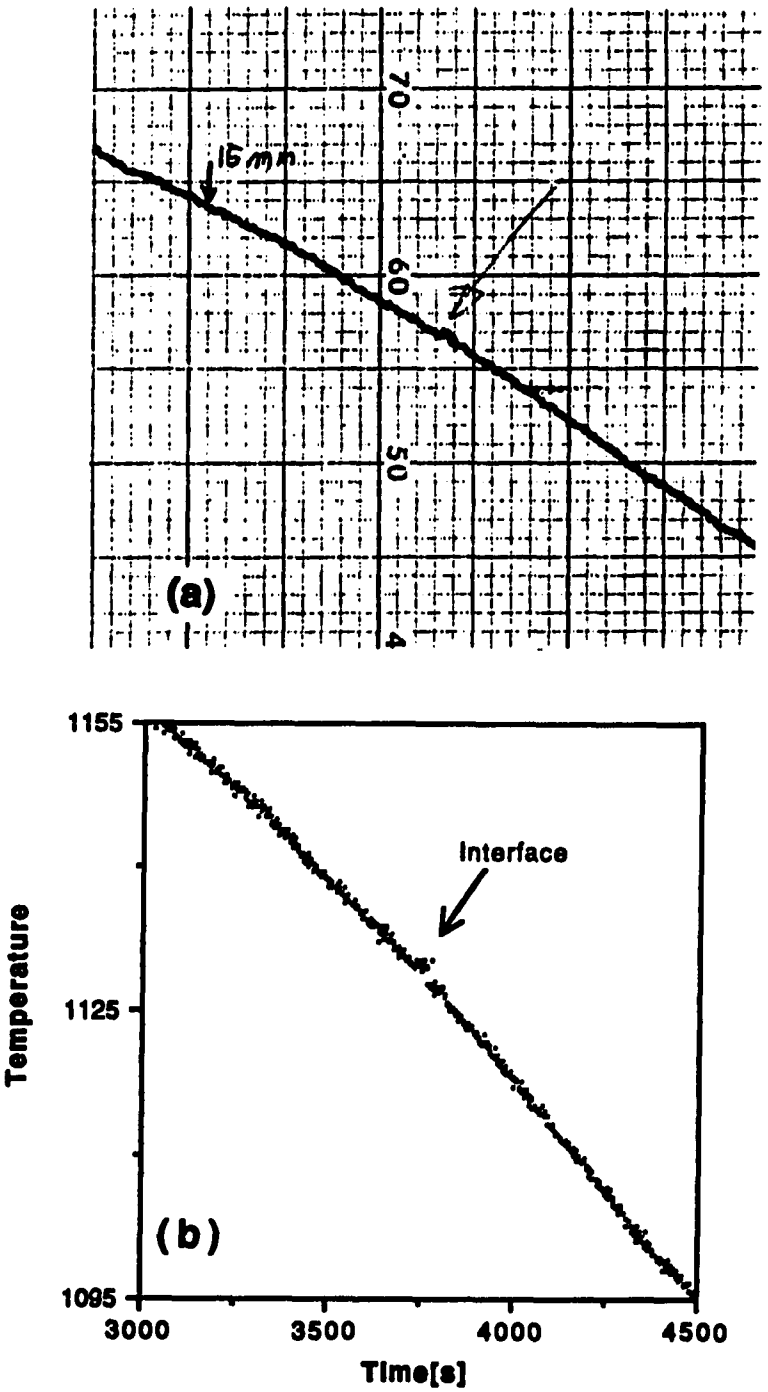

Figure 7. Result of the temperature profile experiment. Rate=5 um/s. (a) on a chart recorder, (b) on a data acquisition system

conductivity in the solid is not much different from that in the liquid, the gradient will not show any substantial difference in solid and liquid when the solidification occurs at a low velocity, generating little latent heat. The thermal conductivity of solid cast iron containing 3.1 % C and 1.8 % Si is reported to be around 0.3 w/cm ^{O}K at 1200 ^{O}K (15), which is close to the value of pure iron (16) or low carbon steel (17) at the same temperature. If it is assumed that the thermal conductivity of cast iron in liquid state is also close to that of pure iron, which is known to be 0.26 w/cm ^{O}K (18), the thermal conductivity ratio of cast iron in the solid and in the liquid is close to unity and no noticeable change in temperature gradient is predicted at a low solidification velocity. The data in Table 6 show that the temperature gradient at the solid/liquid interface undergoes a big change at a solidification rate of 50 um/s and above, apparently because of the increasing latent heat effect. It is seen from Table 6 that for the present directional solidification apparatus with the furnace temperature stabilized at 1450°C, the temperature gradient in molten iron ahead of the advancing solid/liquid interface ranges from 75 to 85 °C/cm at the velocity range of 1 to 20 um/s, and approximately 63 °C/cm at the range of 50 to 100 um/s. In addition, the present temperature profile experiment produced a result suggesting that the the thermal conductivity of Fe-3.4C-2Si alloys is approximately the same in both the solid and liquid states, placing the conductivity in the liquid state in the neighborhood of 0.3 w/cm ^{O}K.

DISCUSSION

The experimental results show that the effect of S in the gray solidification of Fe-C-Si alloys is demonstrated by coarsening of the intergraphite spacing in type A structures and the increase in the highest solidification rate at which type A graphite can grow. Sulfur is observed to induce type D graphite at high rates instead of coral graphite which occurs in high purity alloys. Type A graphite grows in S-added alloys up to 10-20 um/s in deceleration experiments and at even higher rates (>50 um/s) in acceleration experiments. Hydrogen has a similar effect to S in gray solidification. It increases the spacing between graphite flakes in type A structures and allows the type A growth at higher rates. Type A graphite grows up to 10-20 um/s in deceleration experiments and up to 20-50 um/s in acceleration experiments. Hydrogen, however, has no effect on the graphite morphology at high rates, i.e., coral graphite still grows even in the H presence. This indicates the important role played by S in promoting the flake growth mode. The effect of O is most pronounced in high purity alloys. Table 1 shows that the type A growth occurs only at 1-2.5 um/s when 10 % O_2 plus Ar is introduced to enrich the solidification atmosphere with O_2. The type A growth is also suppressed down to 5 um/s in high purity alloys under the pure Ar atmosphere even without the deliberate O_2 enrichment. The O presence is inevitable in cast iron solidification, and evidence is observed in Part IV that the pure Ar atmosphere may provide an O activity higher than expected.

It is, therefore, apparent that the elements S and H act in such a way as to oppose the effect caused by O in the gray solidification of Fe-C-Si alloys. The high O content suppresses the growth of flake graphite in high purity alloys and the flake growth is allowed only at extremely low rates. When a small amount of S is added to the high purity alloys, the type A flake growth is greatly promoted at a high rate, and the flake growth is maintained in the form of type D structure upon further increasing the rate. The type D

graphite is verified in Part III to be crystallographically identical and show a similar growth behavior to type A. The increased H_2 partial pressure in the solidification atmosphere produces an effect similar to the S addition on type A growth in the solidification of high purity alloys. A large effect on the structure of cast iron, caused by only trace levels of an element, is in most cases associated with its effect on interface chemistry at the solidification front. The increased H_2 or O_2 partial pressure in solidification atmosphere, therefore, appears to raise the activity of the corresponding element in the molten cast iron which may thereby affect the melt chemistry at the growth front. With regard to the S, it has long been argued that the S enrichment in the melt near the solidification front is responsible for its effect on structure control. The mechanism by which the trace elements, S and O, produce such a dramatic effect on the structure of cast iron has often been postulated to involve the selective adsorption of these elements during growth into the liquid, thereby reducing the local growth rate and allowing a different growth form to dominate. Part II of this study has utilized scanning Auger spectroscopy to study this possibility.

CONCLUSIONS

1. Directional solidification experiments have established that the addition of 0.02 wt. % S to an Fe-3.4 C-2 Si alloy allows the growth of type A graphite at solidification rates up to 10-20 um/s in deceleration and up to 50 um/s in acceleration experiments. These numbers compare to solidification rates of 2.5 to 5 um/s for both transitions when no S is used.

2. The S addition causes the spacing between graphite flakes to be coarser in type A gray structure, and it produces type D graphite, rather than coral graphite, at high solidification rates.

3. It has been also established that the control of the solidification atmosphere with a H_2 gas has a substantial effect on the microstructure solidified from a high purity gray cast iron, which is similar to the S addition. Hydrogen induces coarsening of the intergraphite spacing in type A structures and allows type A growth at higher rates up to 10-20 um/s in deceleration and up to 20-50 um/s in acceleration experiments. Without the S addition, however, coral graphite grows at a higher rate even under the H-rich atmosphere.

4. Effect of the increased O content is most clearly demonstrated in the solidification of high purity Fe-C-Si alloys under 10% O_2 + Ar atmosphere. The type A growth is suppressed and occurs only at solidification rates of 1-2.5 um/s. The experimental conditions of high purity alloys plus pure Ar atmosphere also appears to provide a relatively high O activity in melt, and the type A growth occurs only at rates 5 um/s or below.

5. The interface quench experiment produces strong evidence that the austenite iron phase grows a significant amount during the fastest quenching used here. Consequently, it

is not possible to determine if the graphite leads the iron at the growth front from the fastest quenching experiments.

6. The temperature profile experiments produced a result suggesting that the thermal conductivity of Fe-3.4C-2Si alloys is approximately the same in both the solid and liquid states near the solid/liquid interface, placing the conductivity in liquid state in the neighborhood of 0.3 W/cm ^{o}K at around 1150°C.

REFERENCES

1. Oldfield, W. "Recent Research on Cast Iron", H. D. Merchant eds., Gordon and Breach Sci. Publ., London, 1968, 347.

2. Garber, S. JISI, Dec., 1955, 181, 291.

3. Hughes, I. C. H. AFS Trans., 1969, 77, 121.

4. Bhavsar, R. D.; Blake, N. W.; Ghoreshy, N.; Smith, R. W. "The Physical Metallurgy of Cast Iron", 3rd Intl. Symp., Stockholm, Sweden, 1984, 77.

5. Nieswaag, H.; Zuithoff, A. J. "The Metallurgy of Cast Iron", B. Lux et al. eds., Georgi, St. Saphorin, 1975, 327.

6. Lux, B.; Kurz, W. "The Solidification of Metals", ISI Publ. 110, 1967, 193.

7. Sayama, Y.; Sato, W.; Ohira, G. J. Cryst. Growth, 1974, 22, 272.

8. Lux, B. Giesserei Forschung, 1967, 19, 141.

9. Magnin, P.; Kurz, W. Met. Trans., 1988, 19A, 1965.

10. Hultgren, A.; Lindblom, G.; Rudberg, E. J.I.S.I., 1954, 176, 365.

11. Fredriksson, H.; Wetterfall, S. E. "The Metallurgy of Cast Iron", B. Lux et al. eds., Georgi, St. Saphorin, 1975, 277.

12. Jones, L. L. M. S. Dissertation, Iowa St. Univ., Iowa, U.S.A., 1985.

13. Fisher, D. J.; Kurz, W. Acta Met., 1980, 28, 777.

14. Magnin, P.; Kurz, W. Acta Met., 1987, 35, 1119.

15. Goldsmith, A.; Waterman, T. E.; Hirschhorn, H. J. "Handbook of Thermophysical Properties of Solid Materials-Revised Edition-Volume II : Alloys", The Macmillan Co., New York, N.Y., 1961, 63.

16. Powel, R. W.; Ho, C. Y.; Liley, P. E. "Handbook of Chemistry and Physics 67th Edition", R. C. Weast eds., CRC Press, Boca Raton, Florida, 1986-87, E-9.

17. Goldsmith, A.; Waterman, T. E.; Hirschhorn, H. J. "Handbook of Thermophysical Properties of Solid Materials-Revised Edition-Volume II : Alloys", The Macmillan Co., New York, N.Y., 1961, 37.

18. Ostrovskii, O. I.; Ermachenkov, V. A.; Grigoryan, V. A.; Borovskii, O. B.; Merkulov, E. N. Zavod.Lab., 45 (11) (Engl. Trans.), 1260, 1980.

PART II. AUGER FRACTURE ANALYSIS ON Fe-3.4C-2Si ALLOYS WITH AND WITHOUT THE ADDITION OF 0.02 % S

INTRODUCTION

The directional solidification studies in part I demonstrated that a small amount of S (200 ppm) in an Fe-C-Si alloy induced significant modifications in solidification microstructures of gray cast iron. In high purity alloys with no deliberate S addition, the growth of type A flake graphite is greatly suppressed and allowed only at very low rates, a few um/s, above which coral graphite starts to appear in the solidification microstructure. The S addition promotes the growth of type A flake graphite at an order of magnitude higher velocities and produces type D graphite upon further increasing the velocity. In addition, the spacing between graphite flakes becomes coarser in type A graphite on S addition.

It has been traditionally believed that the formation of flake type graphite in cast iron solidification is induced by the presence of impurities called growth modifiers. The most technically interesting impurities are S and O, and their presence is hard to avoid in cast iron melt. In view of the powerful effect achieved with the trace amount, most studies have been concerned about the adsorption behavior of the impurities at the growth front, particularly at the iron/graphite interface and/or within the graphite phase, in order to understand their effect on structure control. Johnson and Smartt (1) studied type A flake and nodular cast iron fracture surfaces using a scanning Auger microscope (SAM). They reported that S and O were adsorbed at iron/graphite interfaces in A graphite cast iron but that in nodular cast iron the interface was free of impurity elements. They concluded that the adsorbed impurities poison the growth sites on the basal plane and thereby stabilize the interface, resulting in the development of flakes. Francis (2), however, was skeptical about the validity of Johnson and Smartt's conclusion by pointing out the fact that the segregation they observed at the iron/graphite interfaces were probably formed after solidification in solid state. Francis examined the chemistry of graphite which had been

extracted from matrix using acid in an effort to investigate the incorporation of the growth modifiers into the graphite. He observed a high concentration of O in solution in type A graphite but very little S. In nodular graphite, he found no O or S in solution in graphite. He made a suggestion that O and S are the major growth modifiers inducing flake graphite. Franklin and Stark (3) introduced secondary ion mass spectrometry (SIMS) in order to study the graphite chemistry, taking advantage of its elemental sensitivity and elemental resolving power. Although they could not obtain quantitative information of the elemental concentration because of the matrix dependency of the elemental sensitivity in SIMS, they could obtain an indication of the relative proportions of the elements present within graphite. They found in type A graphite that S is segregated mainly at the interfaces between graphite crystal layers and that O is evenly distributed throughout the graphite flakes. The S segregation was concluded to encourage the extended interfaces characteristic of flake graphite through a reduction in the interfacial energy. The O was considered to adsorb on the prism plane promoting a high interface mobility. The alloys chosen for the previous studies were of typical commercial purity containing a significant amount of S (0.02-0.133 wt.% in type A gray iron and >0.015 wt.% in nodular iron except one sample, 0.004 wt.%, of Johnson and Smartt's experiment), in addition to other minor elements. Alloys of different compositions were used to obtain cast irons of two different graphite morphologies, type A flake and nodular. Samples were all solidified in conventional casting experiments and no specification was given of the solidification conditions such as velocity, atmosphere and temperature gradient.

The present study utilized the SAM in order to investigate the effect of S and O on the structure control in gray cast iron. Alloys of Fe-3.4C-2Si were prepared with and without the addition of 0.02 wt.% S. Cast irons of three different graphite morphologies, type A and D flake and coral, were solidified in Part I using directional solidification

techniques which provide a close control over solidification atmosphere, velocity and temperature gradient. In the solidification of gray cast iron, coarse type A flake graphite transforms to fine type D in S-added alloys but to coral graphite in high purity alloys upon increasing the velocity. The variation in the adsorption behavior of the S and O could be examined as a function of solidification velocity and graphite morphology in a single sample of the same composition. The effect of the S addition on the adsorption characteristics was also investigated using alloys solidified at the same conditions except for the difference in S content.

EXPERIMENTAL TECHNIQUE

Cast irons of type A and coral graphite were directionally solidified from the alloys made to a target composition of Fe-3.4C-2Si. The addition of 0.02 wt.% S was applied to the parent alloy in order to obtain type D graphite. Details of the alloy preparation and the solidification experiments are included in Part I.

The 5 mm diam. directionally solidified rods of Part I had a longitudinal flat ground on one side for microstructural examination. A V-notch was filed into the sample at right angles to the rod axis. A sample was placed in the UHV chamber of a PHI Model 600 scanning Auger microscope (SAM) and broken in the liquid nitrogen cooled fracture stage at an indicated pressure of 2×10^{-10} torr. The fracture surface originated at the base of the V-notch and propagated transverse to the rod axis across the diameter of the sample rod. Studies were done on rods possessing three different graphite morphologies, type A and D flake graphite and coral graphite. Commercial samples of type A and D graphite, prepared by John Deere Foundry at Waterloo in Iowa, were also investigated. The commercial type A samples were poured from inoculated iron, which is used in actual production. In order to obtain the required type D structure, some samples were taken directly out of a holding furnace and specifically not inoculated. Results of the chemical analysis for both samples are given in Table 1.

The SAM was equipped with a secondary electron detector so that secondary electron images (SEI) could be produced just as in a scanning electron microscope (SEM). It was also provided with an Ar ion sputter gun so that surfaces could be depth profiled. After samples were examined in the SAM they were removed and additional examination of the fracture surfaces was done in a standard SEM which provided improved image resolution.

Table 1. Result of chemical analysis on commercial samples [wt. %][a]

Element	Inoculated	Not inoculated
C	3.40	3.38
Si	1.91	1.78
P	0.04	0.03
S	0.07	0.06
Mn	0.58	0.55
Ni	0.12	0.07
Cr	0.22	0.22
Mo	0.05	0.01
Cu	0.18	0.17
Al	0.001	0.003
Sn	0.021	0.016
Ti	0.021	0.022

[a]Analyzed and provided by John Deere Co.

RESULTS

The results obtained from a sample of type A structure are presented in Figs. 1. The sample was solidified from the S-added alloys at 2.5 um/s in Experiment S02-4 of Part I. Figure 1a shows the surface topography as seen in an SEI image taken in SAM and Fig. 1b shows the O (510 eV) Auger map of the same area. The bright area in the SEI image shows fine markings on the surface which are delineated by the light areas in the O Auger map, Fig. 1b. The light areas of Fig. 1b are high in O. The corresponding Auger maps for S (152 eV) and Fe (46 eV) are given in Figs. 1c and d, respectively. By placing a transparency over Fig. 1b, tracing out the dark regions, and then laying it on Figs. 1c and d, it will be seen that both S and Fe occur in the same regions, and these regions are low in O. The O and S Auger maps show that the two elements occupy regions that are mutually exclusive. This result was consistently found at the many different locations which were examined. The Auger spectra taken at point 1 in a high O area and point 2 in a high S area are shown in Figs. 2a and b, respectively. The spectra confirm the results of the Auger map analysis in that the regions high in S is low in O and vice versa. The signal intensity of C is low in both spectra and about the same level as that in Fig. 2c, a spectrum taken in an austenite dendrite stem. This indicates that the areas high in either S or O contain about the same level of C as the iron matrix. When interpreting these spectra, it is important to realize that the depth from which an Auger electron can escape and be detected is a strong function of its inelastic mean free path λ. For example, the intensity I(d) of a matrix iron Auger electron emerging through an overlying material of thickness d is given as

$$I(d)/I(0) = \exp [-d/(\lambda\cos\theta)] \qquad (1)$$

where I(0) is the intensity with d=0 and, for the cylindrical mirror analyzer detector used here, $\cos\theta=0.74$. Values of λ depend on the energy of the Auger electrons E and are given by (4)

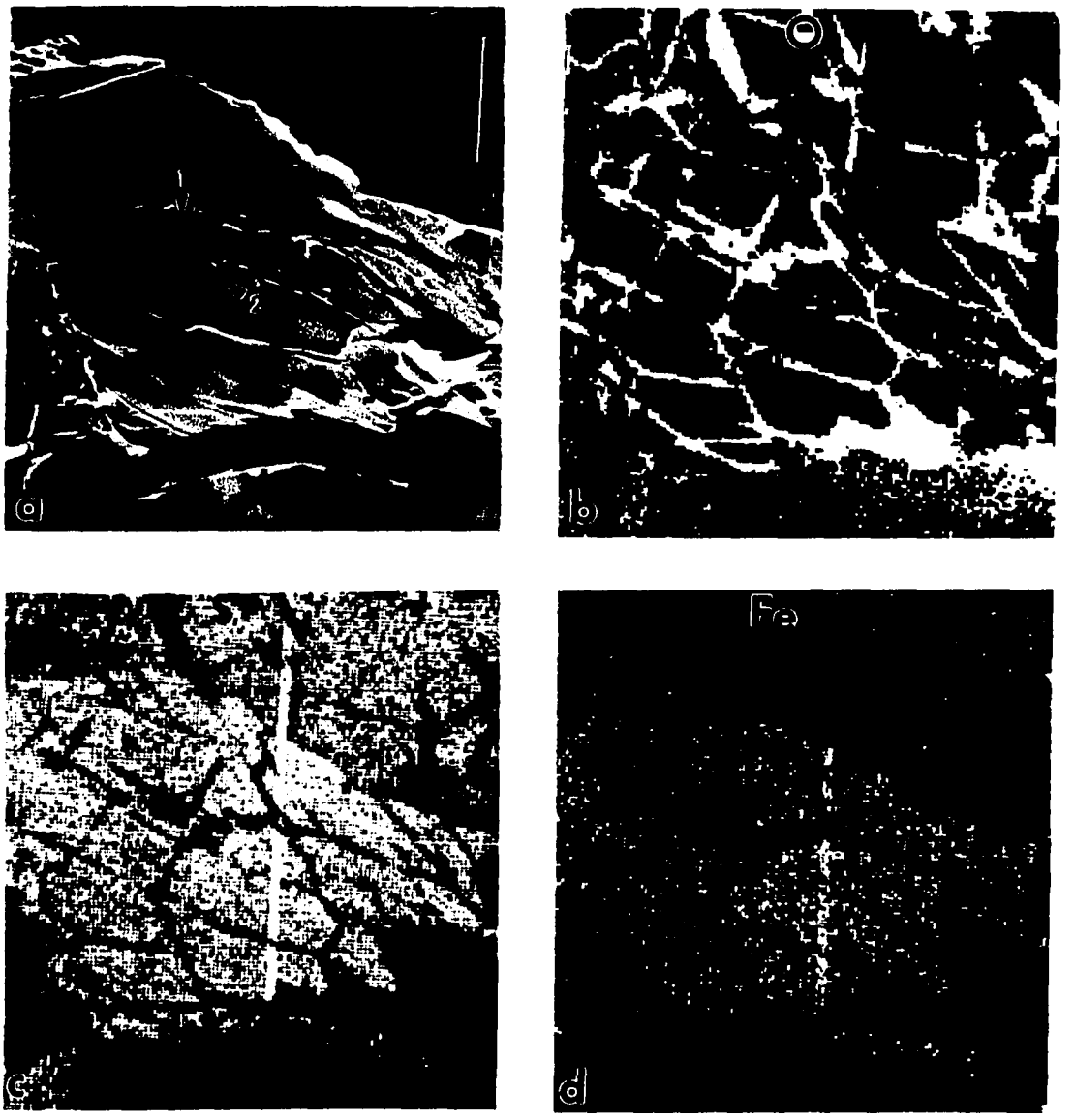

Figure 1. Auger analysis of type A gray iron fracture surface of Experiment S02-4, rate=2.5 um/s. (a) SEI image, (b), (c), (d) Auger elemental maps for O(510 eV), S(152 eV), and Fe(46 eV), respectively

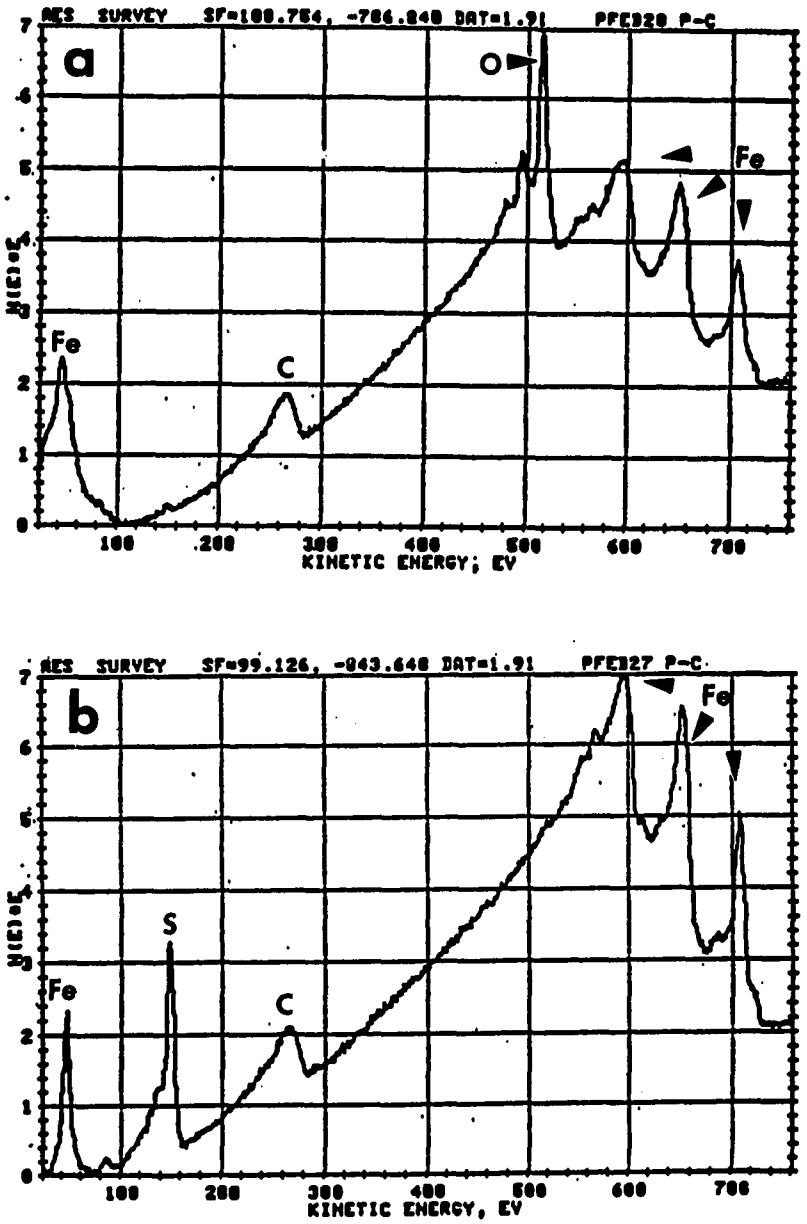

Figure 2. Auger spot analysis. (a), (b) Auger spectrum of point 1 and 2 in Fig. 1a, respectively, before sputtering

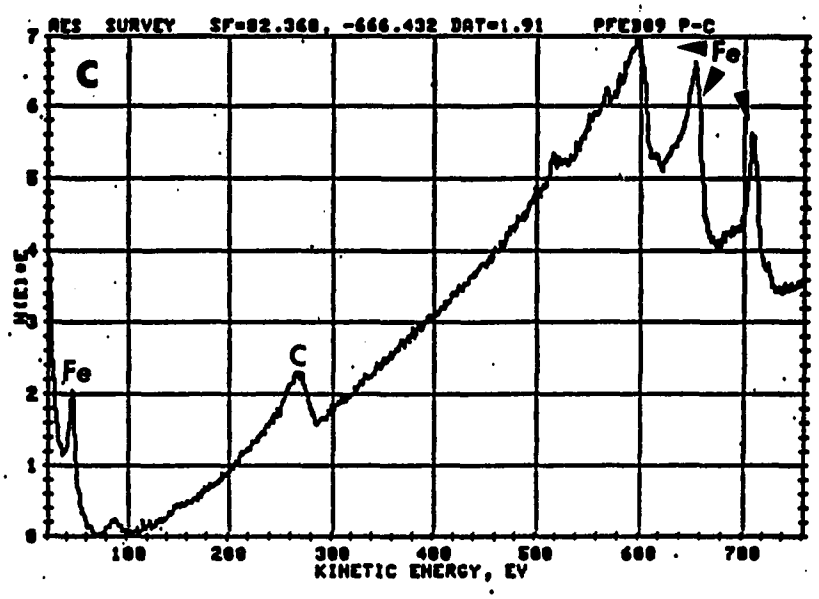

Figure 2. (continued) (c) Auger spectrum of a point on bulk iron fracture surface

$$\lambda = 538/E^2 + 0.41\ (aE)^{1/2}\ \text{[monolayer]} \qquad (2)$$

where E is in electron volts and a is the thickness of an overlying monolayer in nm. For the case of S coverage on top of iron matrix, equations (1) and (2) predict that one overlying monolayer will reduce the intensity of the low energy Fe (46) peak by 54 %, whereas the high energy Fe (703 eV) peak is reduced by only 20 %. Therefore, the Fe (46) peak is most sensitive to overlays of S or O. Figures 2d and e give the Auger spectrum from point 1 and 2, respectively, after sputtering with 3 kV Ar ions. It is seen that the O or the S signal is gone, indicating that either element was covering the iron matrix and has been sputtered away. An interesting fact to be noticed in the spectrum, Fig. 2a, taken from a high O area is that the low energy Fe (46) signal has a peak at 42.5 eV, not at 46.5 eV as can be verified in Fig. 2f. It is seen from Fig. 2c, a spectrum taken from a fractured dendrite stem, that the low energy Fe electrons generated from elemental Fe should have a peak at around 46 eV. The energy shift of about 4 eV occurs when a pure element is oxidized and indicates that the iron in the O-rich regions of Fig. 1a is present in the form of iron oxide. This means that a layer of iron oxide is covering the matrix iron in the O-rich regions. The spectrum, Fig. 2d, taken from the same area after sputtering has the low energy Fe peak at 46 eV, indicating that the signal is now coming from the elemental matrix iron. No such shift in energy is observed in the spectrum, Fig. 2b, taken from the S-rich area. The S-rich area, therefore, appears to be covered by elemental S. It should be mentioned at this point that the low energy Fe Auger map shown in Fig. 1d was taken by use of the Auger electrons generated from the Fe in elemental form having a peak at 46 eV. Therefore, the areas covered by iron oxide, the O-rich area, turned out to be dark in the low energy Fe map.

The Auger sputtering analysis was carried out on the area including points 1 and 2 shown in Fig. 1a and the results are presented in Figs. 3 and 4. The intensities of the

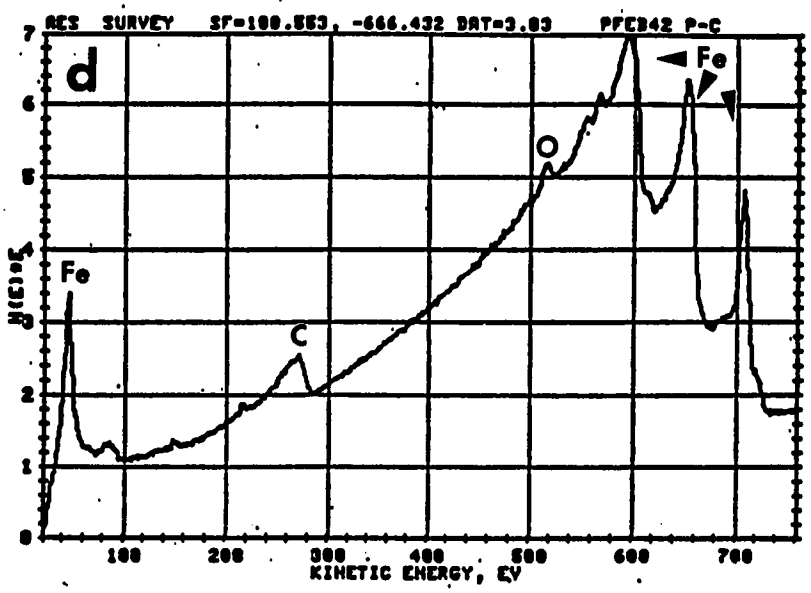

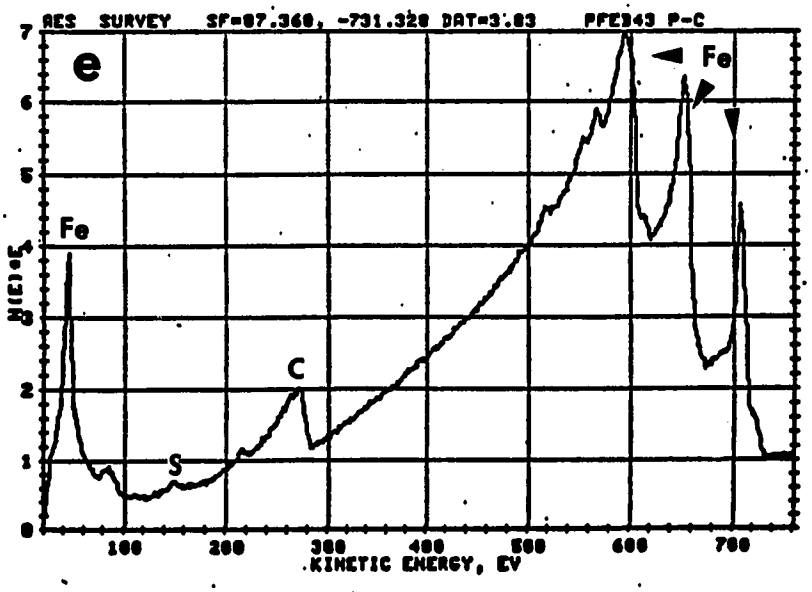

Figure 2. (continued) (d), (e) Auger spectrum of point 1 and 2 in Fig. 1a, respectively, after 40 min sputter cleaning with 3 kV Ar ions

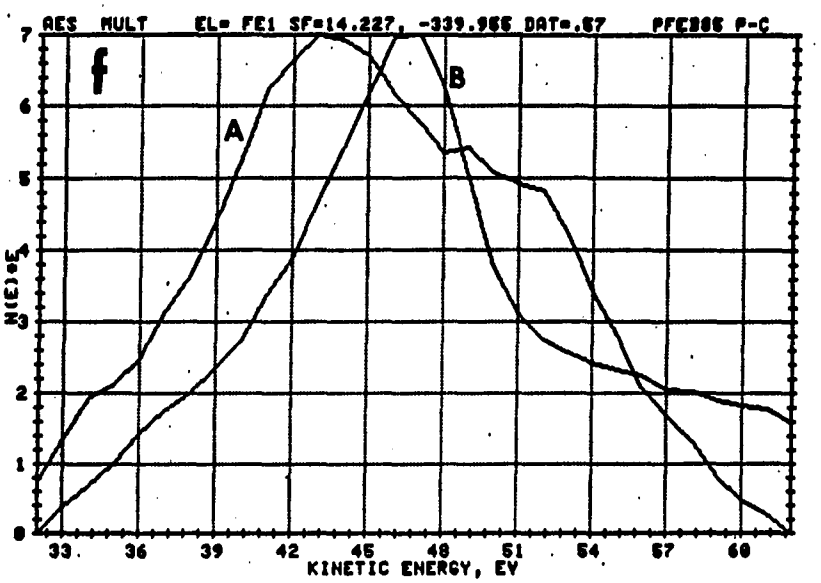

Figure 2. (continued) (f) Auger spectrum showing the low energy Fe(46 eV) peaks of point 1 in Fig. 1a before (line A) and after (line B) the sputter cleaning of oxide layer

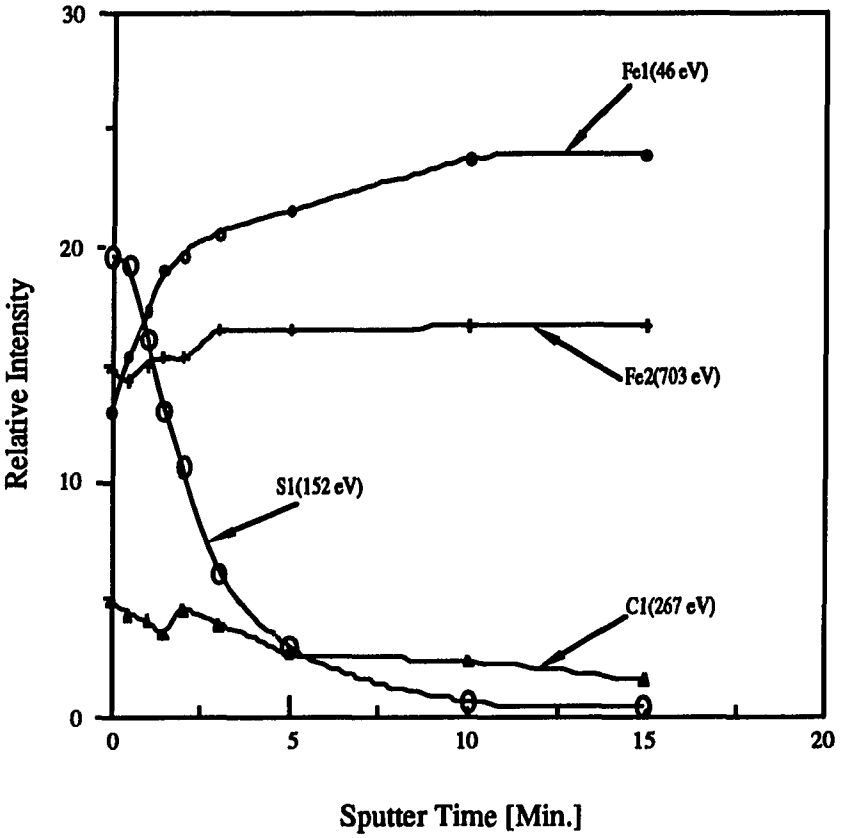

Figure 3. Auger depth profiling analysis on point 2 of Fig. 1a (S-rich region)

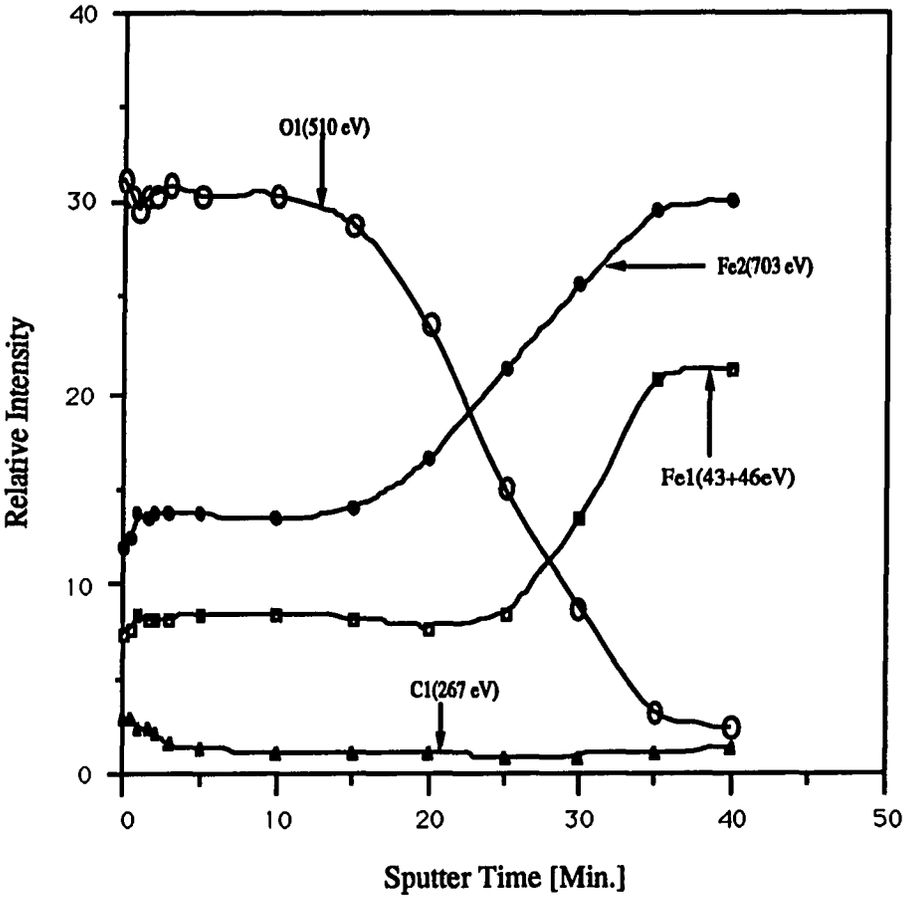

Figure 4. Auger depth profiling analysis on point 1 of Fig. 1a (O-rich region)

Auger peaks were evaluated by taking the first derivative of the N(E)E curves and evaluating the peak-to-peak height at the four signals of interest, where Fe1=Fe (43+46 eV), Fe2=Fe (703 eV) and C1=C (267 eV) plus either O1=O (510 eV) at point 1 or S1=S (152 eV) at point 2. The change in the signal intensities by sputtering on point 2, the S-rich area, is presented in Fig. 3. At this location, the Fe (46) signal rises as the S is sputtered off and it is possible to determine the thickness of the S layer from the data of Fig. 3. The value of I(d) for the Fe (46) signal is found at time zero, and the values of I(0) at time = 15 minutes, after the Fe (46) intensity saturates. From these data, the value of d was determined using equations (1) and (2) to be 2.36 Å. This value is quite close to a S monolayer thickness, 2.95Å, and so it is concluded that the S-rich regions are covered with close to a monolayer of S. The result of sputtering on point 1, the O-rich area, is given in Fig. 4. In contrast to the S-rich area where sputtering produced an immediate change in the signal intensities, the sputtering on this location did not bring about any significant alteration in intensities until the area has been sputtered a certain amount of time. The high energy Fe (703 eV) signal starts to rise when the O (510 eV) intensity starts to decrease after 10 min. sputtering. The low energy Fe (46) signal remains the same for 25 min. sputtering until it starts to rise. The Fe1 (46) and the Fe2 (703) signals reach the saturation at the same time as the O is almost gone after 35 min. sputtering. The variations in the signal intensity with the sputtering can be explained as follows. The initial period of sputtering causing no change in the signal intensity indicates that the oxide layer provides more than a monolayer coverage. If the oxide overlay is much thicker than the escape depth of an Auger electron emerging through the layer, there will be no change in the relative intensities since they will be mostly determined by the electrons generated within the overlay. When the overlay is sputtered off and its thickness comes to fall in the neighborhood of the escape depth, then the electrons generated below the overlay are able

to escape and be detected to commence changes in the relative intensity. Figure 4 shows that this happened after 15 min. sputtering. When the top oxide layer is thinned by sputtering, generation of the O Auger electrons is reduced and more Fe electrons can escape the overlay to be detected. As formerly mentioned, since the low energy Fe peak is most sensitive to overlays because of its short inelastic mean free path the oxide layer should be more sputtered off until the low energy Fe Auger electrons generated below can emerge on the surface and be detected to increase the signal intensity. The Fe (46) signal starts to rise 25 minutes after sputtering and saturates at 35 min. sputtering. Therefore, if the escape depth of low energy Fe Auger electrons in iron oxide is assumed to be approximately two monolayers, it would take 10 minutes to sputter off the one monolayer iron oxide. Accordingly, it can be estimated for the present case that the oxide layer provides 6 or 8 monolayer coverage on the iron matrix since the total of 35 minutes was elapsed to sputter clean the overlay.

A type A sample solidified at a higher rate 10 um/s from S-added alloys was also analyzed and the result is presented in Figs. 5. Figure 5a is an SEI image of the area analyzed and Figs. 5b, c and d show, respectively, the S (152 eV), C (267 eV) and Fe (650 eV) Auger maps of the same area. The fracture surface seen in the SEI image, Fig. 5a, has fine markings like those observed in the 2.5 um/s type A sample. The Auger maps, however, shows no hint of O adsorption in this sample. The S Auger map, Fig. 5b, indicates that the fracture surface is mostly covered with S and a few dark regions in the S map are shown in the C map, Fig. 5c, to be occupied by small pieces of graphite. The Fe (650) map, Fig. 5d, shows that both S and Fe occur in the same regions, and the regions high in C are low in Fe. The Auger spectra taken at point 1 in a S-rich area and point 2 in a C-rich area are presented in Figs. 6a and b. The relative signal intensities in Fig. 6a are about the same as those in Fig. 2b, taken from a S-rich area of the 2.5 um/s sample, and

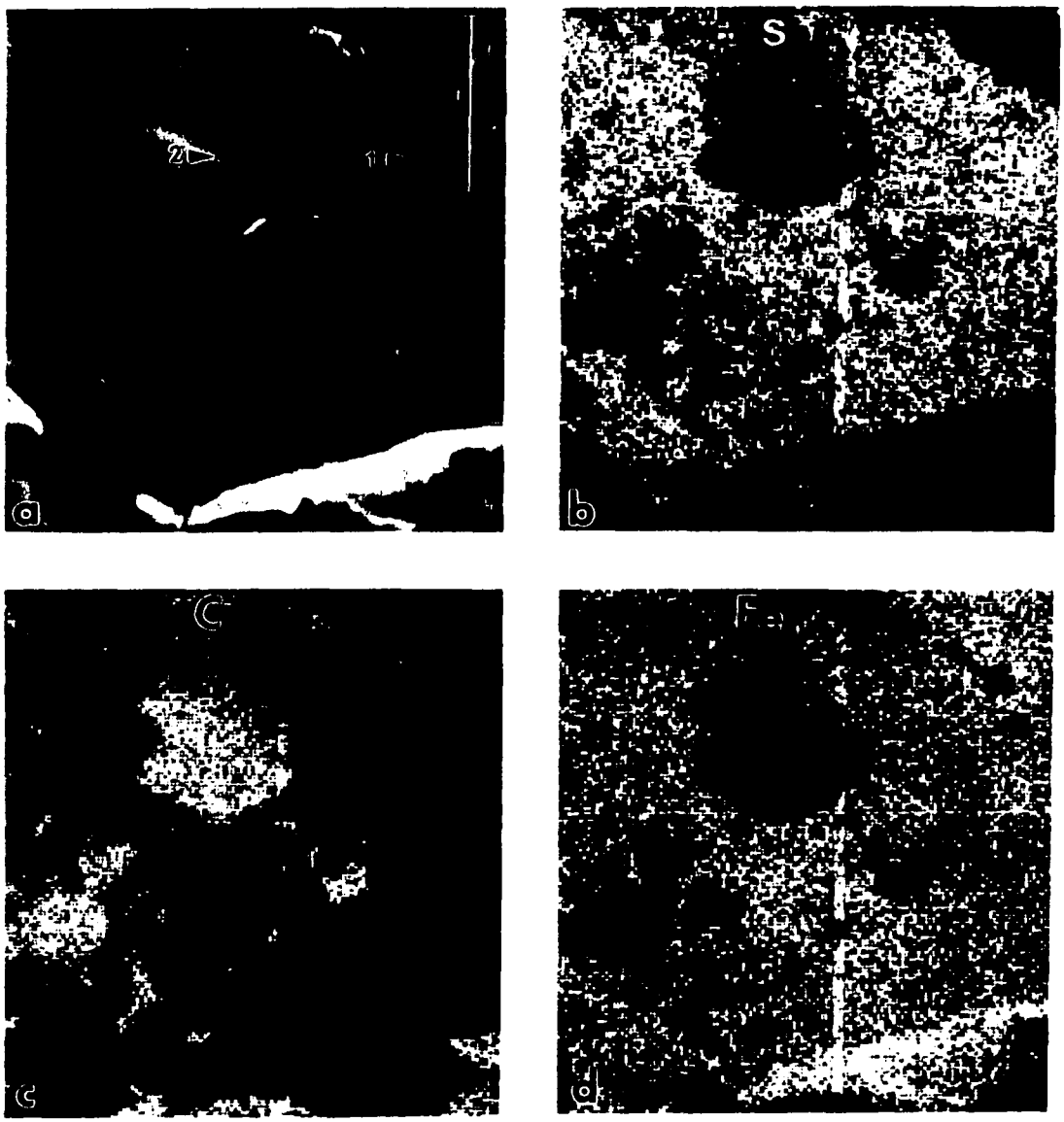

Figure 5. Auger analysis of type A gray iron fracture surface of Experiment S02-14, rate=10 um/s. (a) SEI image, (b), (c), (d) Auger elemental maps for S(152 eV), C(267 eV), and Fe(650 eV), respectively

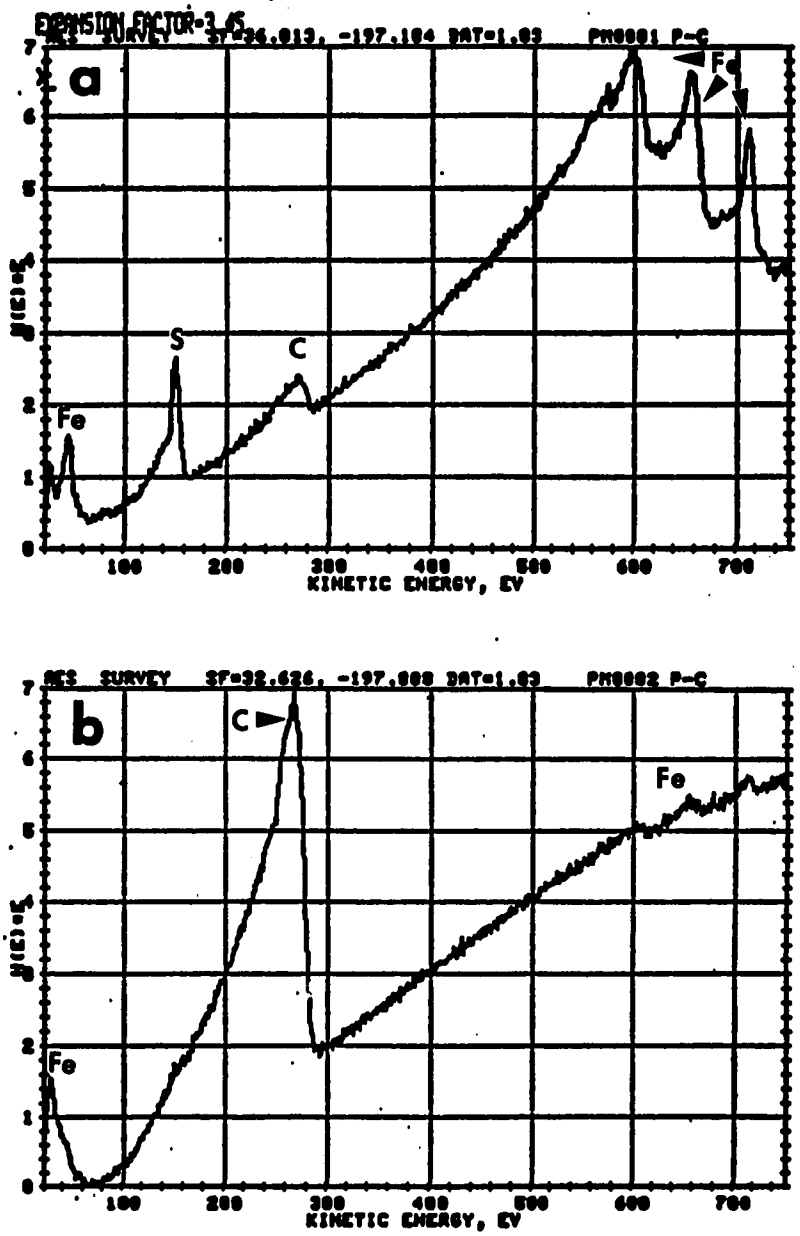

Figure 6. Auger spot analysis. (a), (b) Auger spectrum of point 1 and 2 in Fig. 5a, respectively

therefore the S coverage of this sample is estimated to be approximately one monolayer. Figure 6b shows that the graphite flake is thick enough to suppress the high energy Fe signals almost completely.

Other Auger analyses were carried out on type A samples solidified from high purity alloys with no deliberate S addition and a typical result is given in Figs. 7. The sample was solidified at 1 um/s in Experiment S00-5 of Part I. Figure 7a shows the fracture surface as seen in a SEI image and the Auger maps of the same area for O (510 eV), S (152 eV) and C (267 eV) are presented in Figs. 7b, c and d, respectively. The O map, Fig. 7b, shows that the O covered area is greatly extended in this high purity sample compared to the S-added 2.5 um/s sample. The Auger spectra taken at point A in a S-rich area and at point B in an O-rich area looked similar to Figs. 2b and c, respectively, which were taken from the corresponding area of S-added 2.5 um/s sample. The O was present in the form of iron oxide and the thickness of either O or S coverage was thereby estimated to be about the same as that previously determined. The overall summary of Auger analyses performed on type A samples are presented in Table 2.

Samples having type D graphite structure were investigated in the Auger analysis. Type D graphite is more than an order of magnitude smaller than type A graphite in size and in thickness as shown in Figs. 1a and b of Part III, and grows only in S-added alloys, not in high purity alloys, and only at higher solidification velocities. The typical result obtained with a type D sample is given in Figs. 8. The sample was solidified at 50 um/s in Experiment S02-3 of Part I. Figure 8a shows the topography of the type D fracture surface as seen in a SEI image and Figs. 8b,c and d present the respective Auger maps for S (152 eV), Fe (650 eV) and C (267 eV). It is seen from examining the Auger maps that the areas high in S are almost always high in Fe, and these regions are low in C. The C Auger map, Fig. 8d, indicates that the areas low in S are mostly high in C. The Auger spectrum taken

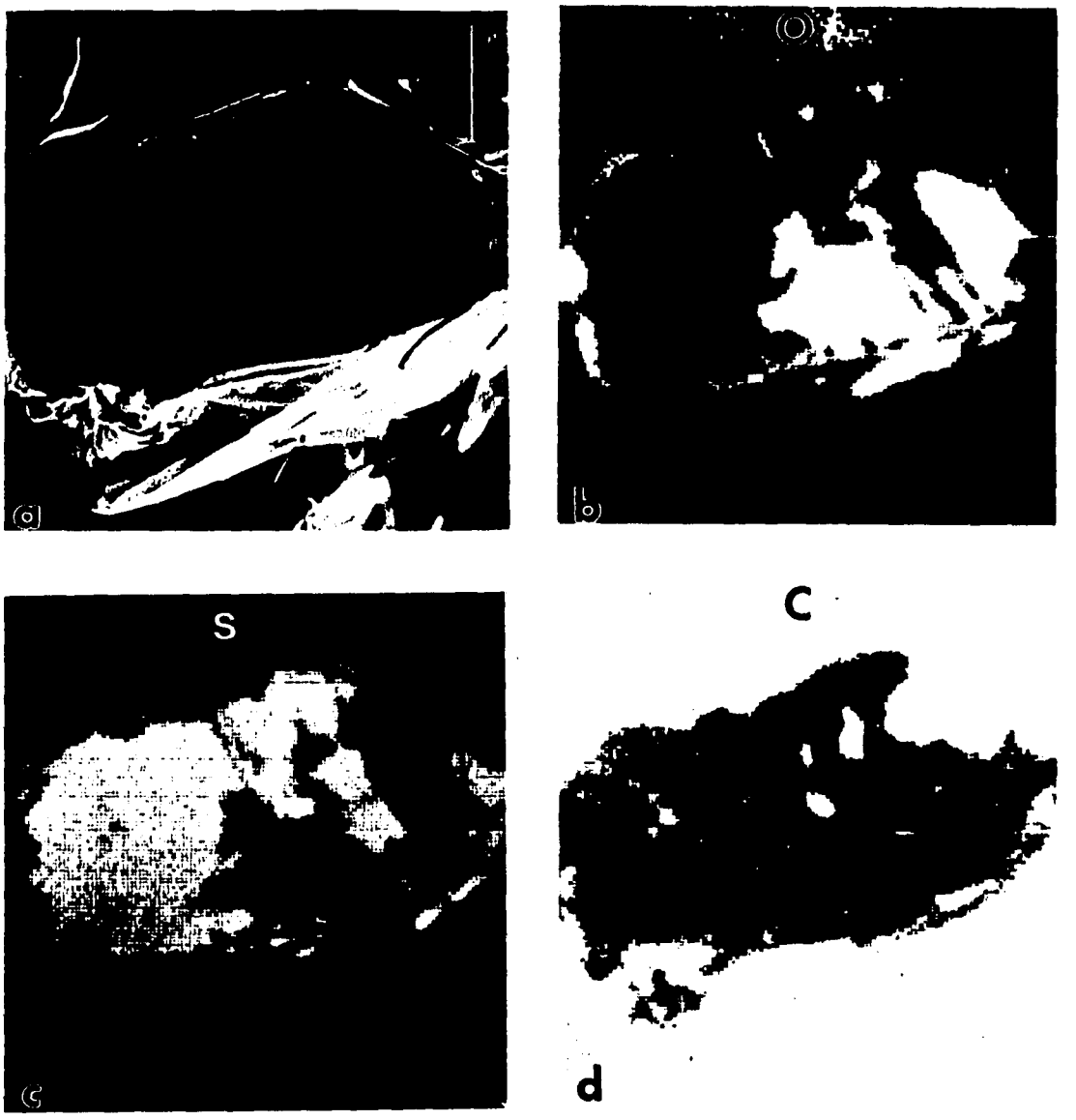

Figure 7. Auger analysis of type A gray iron fracture surface of Experiment S00-5, rate=1 um/s. (a) SEI image, (b), (c), (d) Auger elemental maps for O(510 eV), S(152 eV), and C(267 eV), respectively

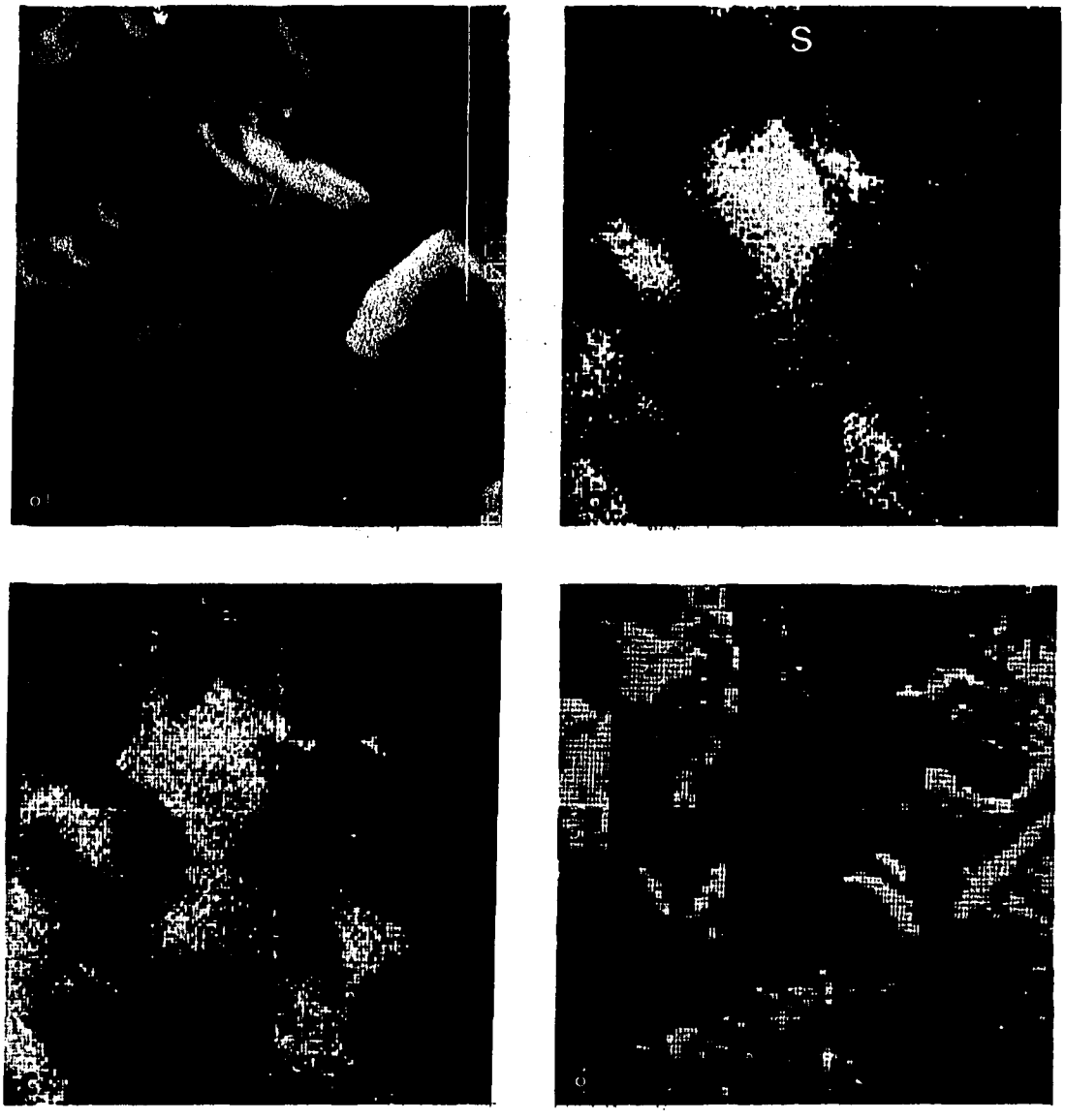

Figure 8. Auger analysis of type D gray iron fracture surface of Experiment S02-3, rate=50 um/s. (a) SEI image, (b), (c), (d) Auger elemental maps for S(152 eV), Fe(650 eV) and C(267 eV), respectively

Table 2. Summary of Auger analyses on cast iron fracture samples of type A graphite

Auger Expt. #	Dir. Sol. Expt. #	Rate [um/s]	Dist. from growth front [cm]	Type of quenching	Matrix Str.	Result
PFEB	S02-2	2.5	6.6	water	Pearlite	S & O competing
PFEC	S02-4	2.5	6.4	water	P	S & O competing
PFED	S00-2	2.5	0.5	water	Martensite	Mostly O
PFEE	S00-5	1	9.5	water	P	S & O competing
PFEF	John Deere	Casting	-	-	P	S & O competing
PFEG	John Deere	Casting	-	-	P	S & O competing
PFEH	S02-6	2.5	2.9	water	P	S & O competing
PL	S00-11	5	0.2	air	P	S & O competing
PM	S02-14	10	0.2	air	P	S with no O
PY	S00-4	2.5	7.4	water	P	S & O competing
PZ	S02-14	5	5.5	air	P	S & O competing

at point A in a high S area is given in Fig. 9 and it shows no hint of O present. In addition, the relative intensity of the S signal compared to that of either Fe1 or Fe2 signal is about the same as in Fig. 2b, the spectrum taken from a S-rich region of S-added 2.5 um/s sample. The S coverage on the underlying iron matrix is, therefore, estimated to be approximately one monolayer. Table 3 summarizes the Auger analyses on cast iron fracture samples of type D graphite having pearlite matrix structure.

Auger analysis was also carried out on samples of coral graphite structures. Figures 10 present the result obtained from a sample solidified at 50 um/s in Experiment S00-12 of Part I. It was verified in Part I that the coral graphite grows only in high purity

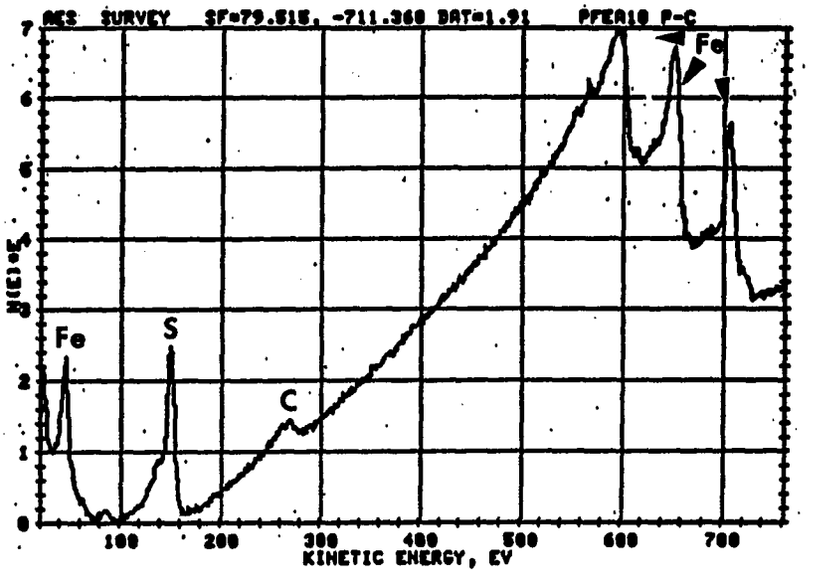

Figure 9. Auger spectrum of point A in Fig. 8a

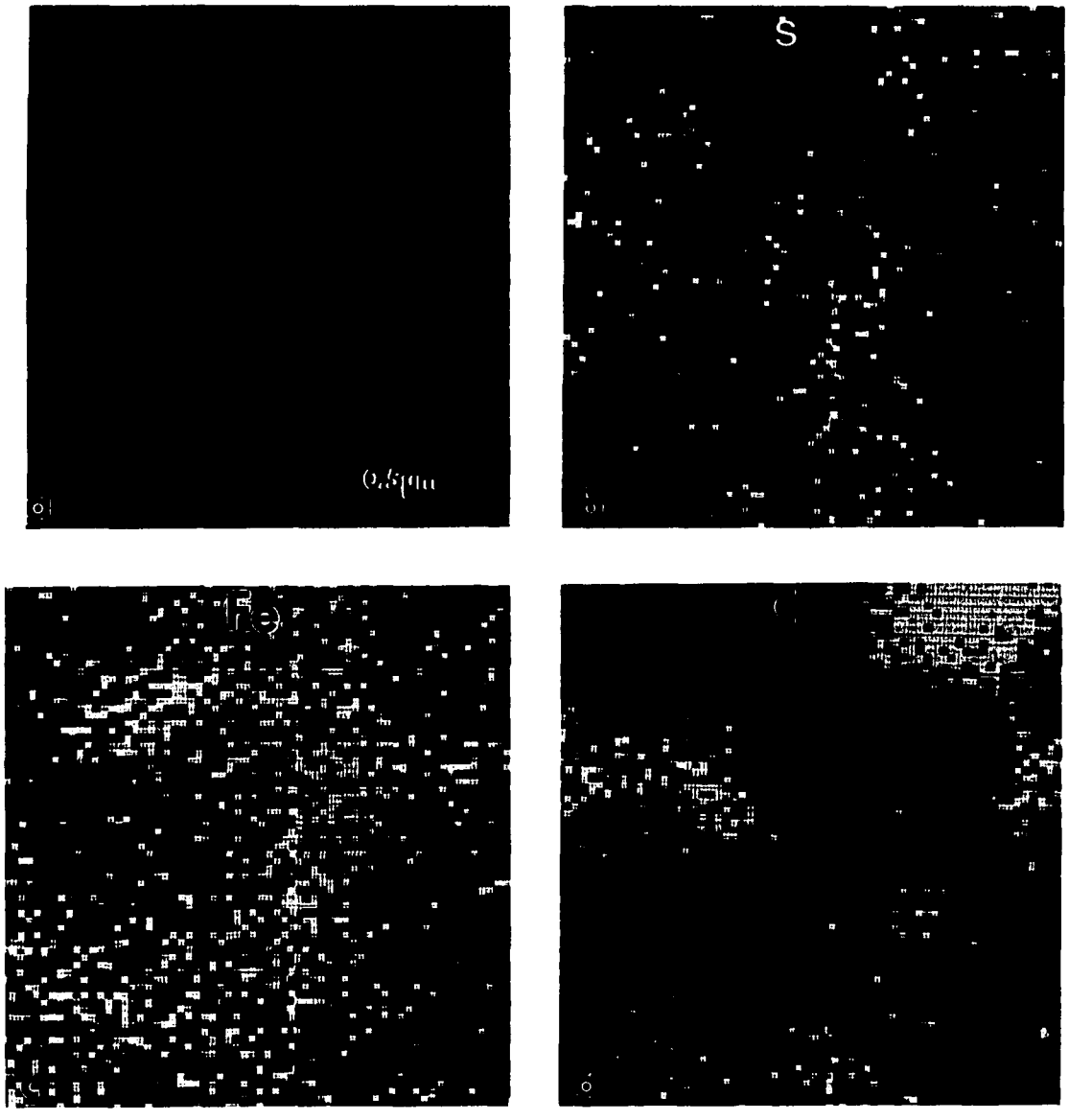

Figure 10. Auger analysis of coral gray iron fracture surface of Experiment PN, rate=50 um/s, distance from growth front=0.3 cm, pearlite matrix. (a) SEI image, (b), (c), (d) Auger elemental maps for S(152 eV), Fe(650 eV) and C(267 eV), respectively

Table 3. Summary of Auger analyses on cast iron fracture samples of type D graphite having pearlite matrix structure

Auger Expt. #	Dir. Sol. Expt. #	Rate [um/s]	Dist. from growth front [cm]	Type of quenching	Result
PFEA	S02-3	50	7	water	S only
PFEG	John Deere	Casting	-	-	S only
PI	S02-2	50	2	water	S only
PJ	S02-12	50	0.3	air	S only
PK	S02-12	50	3.3	air	S only

alloys. Because of the fine nature of the coral structure, analysis had to be restricted to an extremely small area of the fracture surface. Figure 10a shows the SEI image of the area. The high magnification 50 kX must be beyond the image resolving power of the SAM and the image is not very clear. After the sample was examined in the SAM, another SEI image was taken of the same area using a standard SEM of better resolution, which is given in Fig. 11 as a stereopair. The rectangle on Fig. 11 traces the boundary of the area shown in Fig. 10a. The matching Auger maps for S (152 eV), Fe (650 eV) and C (267 eV) are shown in Figs. 10b, c and d, respectively. Apart from the result of type D samples where both S and Fe occur at the same regions with little C, the Auger maps for S (152 eV), Fig. 10b, and for Fe (650 eV), Fig. 10c, indicate that the S-rich region is greatly restricted and included within the region high in Fe. The Fe-rich regions are outlined by black dots on Fig. 11, a stereopair showing the region of Fig. 10a. The points 1, 2 and 3 of Fig. 10a are also located on the stereopair at points with the same labels. The Auger spectrum taken at point 1 is given in Fig. 12a and it shows that the area around this point is the light area of the S Auger map, Fig. 10b. The spectrum taken at point 2 showed big peaks for Fe and C but no hint of S signal. Stereographic viewing of Fig. 11 verifies the presence of small

Figure 11. Stereopair of the same region as Fig. 10a taken with improved resolution in a SEM. Magnification 15,300X

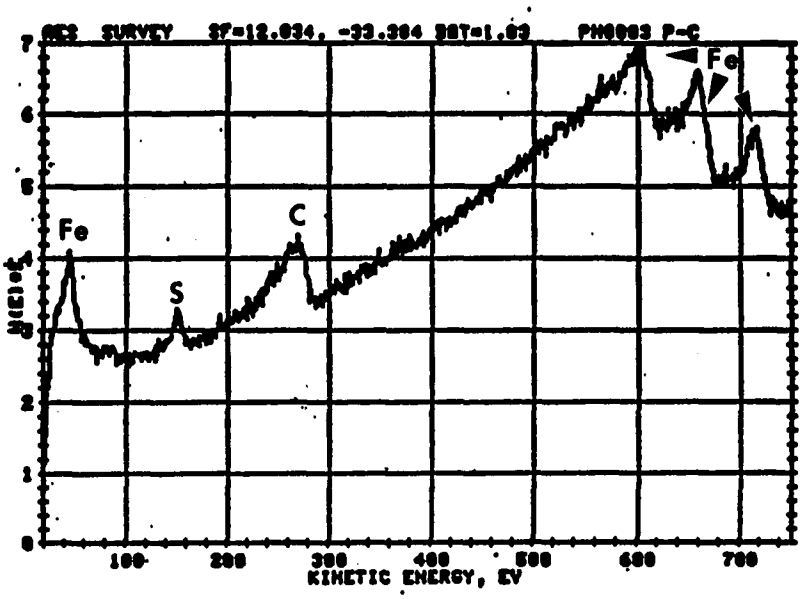

Figure 12. Auger spectrum of point 1 in Fig. 11

graphite filaments at locations shown bright in the C map, Fig. 10d. The fracture surface of coral graphite cast iron looks quite different from that of the flake type graphite cast iron since fracture often occurs transgranularly through the iron matrix. And therefore, it is quite difficult to locate the regions exposed on the surface by the fracture occurring along the iron/graphite interface. As a result, the true appreciation of the impurity adsorption on the interface is extremely difficult to obtain in cast iron samples of coral graphite with the method utilized in this study. Table 4 presents the summary of Auger analyses on cast iron samples of coral graphite.

Table 4. Summary of Auger analyses on cast iron fracture samples of coral graphite

Auger Expt. #	Dir. Sol. Expt. #	Rate [um/s]	Dist. from growth front [cm]	Type of quenching	Matrix Str.	Result
PN	S00-12	50	0.3	air	Pearlite	small S
PP	JP1-17	2.5	4.3	water	P	small S
PW	S00-12	50	2	air	Heat-treated Martensite	O & S mixed

The Auger analysis of the same kind was carried out on commercial type A and D samples prepared in conventional castings and supplied to us by John Deere Foundry, Waterloo, IA. Inoculation was applied before casting to obtain type A samples while the samples cast with no inoculation contained both type A and D structures. The result obtained from a type A sample is shown in Fig.13. Figure 13a shows the SEI image of the fracture surface and Figs.13b, c and d are the corresponding Auger maps for O (510 eV), S (152 eV) and Fe (650 eV), respectively. The results are qualitatively the same as those of the directionally solidified type A sample with 0.02 wt.% S addition. The interface is divided between regions rich in either O or S. And the O in O-rich areas was present in the form of iron oxide. It is, however, seen that the interface is mostly covered with an oxide

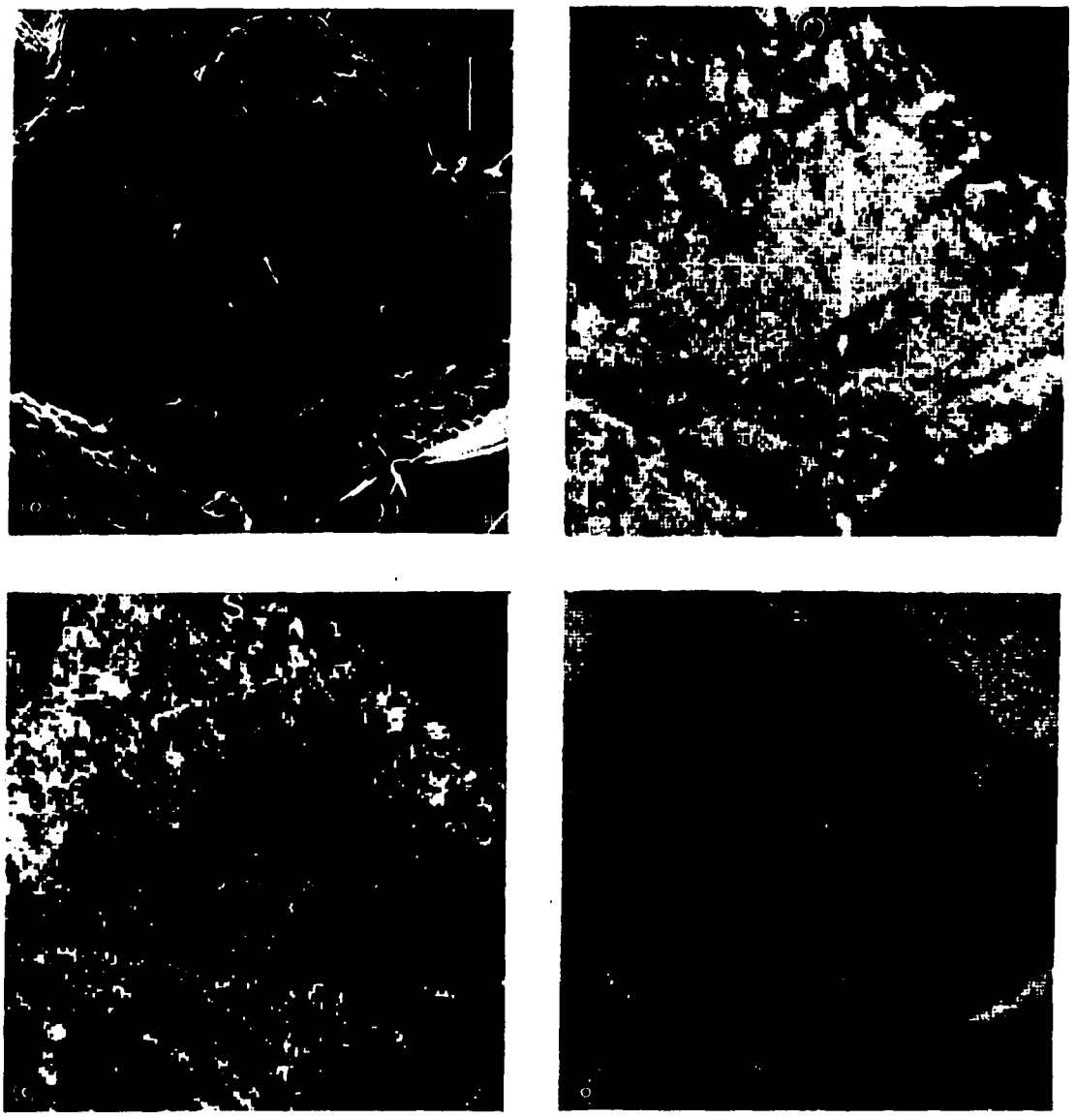

Figure 13. Auger analysis of commercial type A gray iron fracture surface. (a) SEI image, (b), (c), (d) Auger elemental maps for O(510 eV), S(152 eV), and Fe(650 eV), respectively

layer in spite of the high S content (0.07 wt.%). This may be because of the other minor elements included which tie up the S in the form of sulfide. As shown in Table 1, the commercial alloy contains 0.58 % Mn which is more than enough to tie up the S as MnS. Figure 14a presents another interface region of the commercial type A fracture surface containing several sulfide particles. The energy dispersive x-ray spectra taken at points 1, 2 and 3 of Fig. 14a were quite similar, and the spectrum at point 1 is shown in Fig. 14b. As shown in Fig. 14b, the iron/graphite interface of the commercial alloys contains many sulfide particles which consist of Fe, Mn, Ti, Cr, Si and Al. Similar sulfide particles were also observed in the laboratory prepared samples, but with much less frequency and the major participating elements were Fe, Mn and Si.

The sample prepared from the uninoculated commercial gray cast iron was observed to have both A and D graphite structures on its fracture surface. Results on A structures did not show any noticeable difference from the other type A samples previously investigated. The fine D structure produced qualitatively the same result as the directionally solidified type D sample. And Figs. 15 present the SEI image and the corresponding S (152 eV), C (267 eV) and low energy Fe (46 eV) Auger maps, respectively. The fracture surface consists of regions rich in either S or C. Figures 15b and d indicate that the regions rich in S are also rich in Fe. The Auger spectrum, Fig. 16, taken from the S-rich area looked about the same as that of Fig. 2b, and accordingly the S coverage is estimated to be approximately one monolayer.

Another set of experiments was carried out on type D samples solidified at 50 um/s in order to test the possibility of O or S segregation in the solid state during cooling. And they are summarized in Table 5. The directional solidification experiments of Part I were terminated by dropping the sample containment tube into a quench bath containing water which produced a rapid quench. The remaining melt, then, solidified rapidly to give a fine

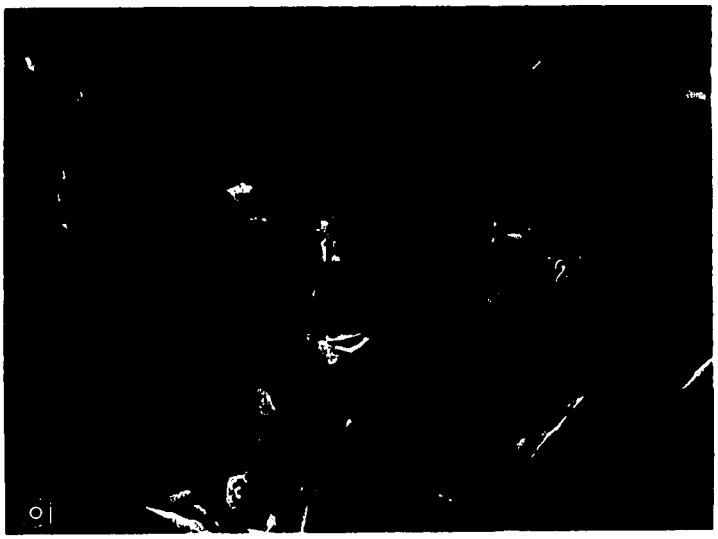

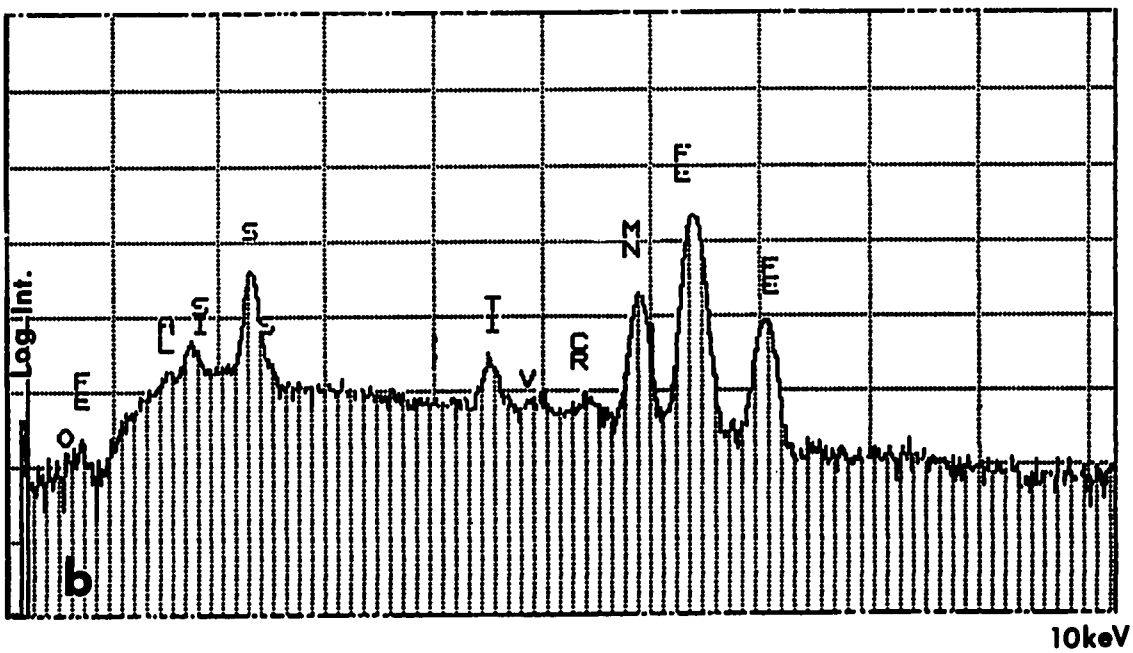

Figure 14. Energy dispersive x-ray analysis. (a) SEI image, (b) x-ray spectrum of point 1 in Fig. 14a

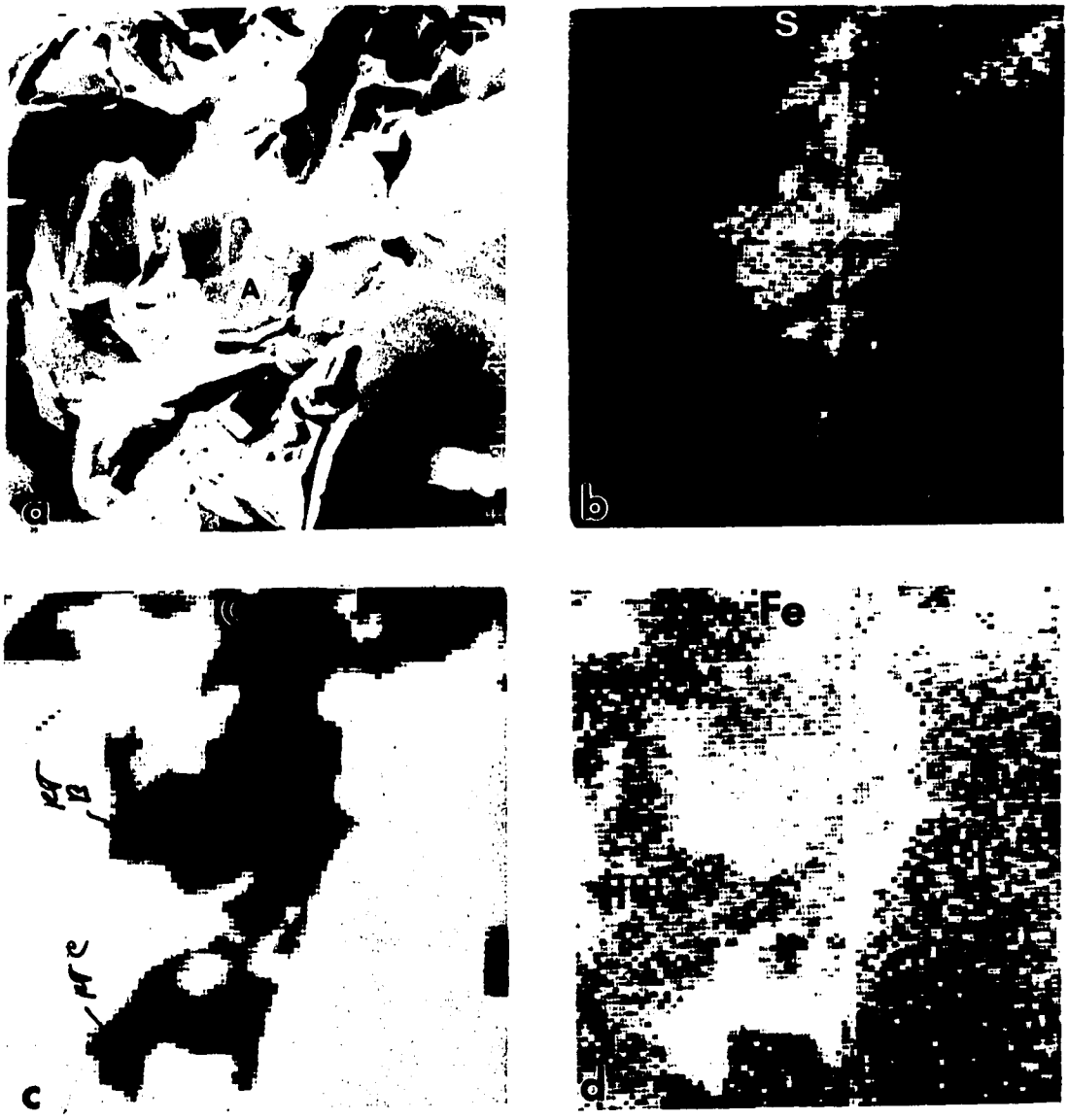

Figure 15. Auger analysis of commercial type D gray iron fracture surface. (a) SEI image, (b), (c), (d) Auger elemental maps for S(152 eV), C(267 eV), and Fe(46 eV), respectively

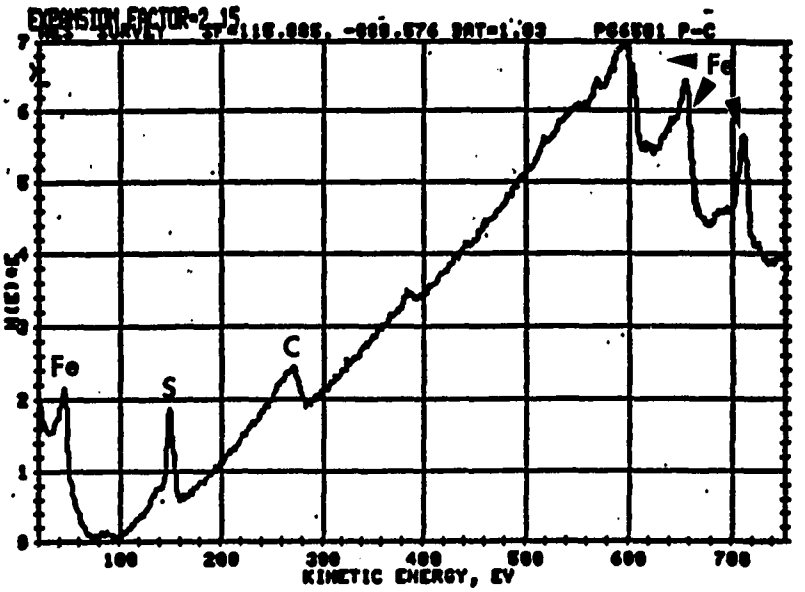

Figure 16. Auger spectrum of point A in Fig. 15a

Table 5. Summary of Auger analyses on cast iron fracture samples of type D graphite having pearlitic or martensitic matrix structure. (Samples solidified at 50 um/s)

Auger Expt.#	Dir. Sol. Expt.#	Matrix Structure	Dist. from growth front [cm]	Result
PH[a]	S02-2	Water quenched Martensite	0.5	O and S mixed
PI	S02-2	Slow cooled Pearlite	2.0	S only
PJ	S02-12	Air quenched Pearlite	0.3	S only
PQ	S02-12	Heat-treated and water quenched Martensite	1.4	O and S mixed
PK	S02-12	Slow cooled Pearlite	3.3	S only
PT	S02-12	Heat-treated and water quenched martensite	4.8	O and S mixed
PR	S02-13	Water quenched Martensite	0.3	O and S mixed
PS	S02-15	Ga-In quenched Martensite	0.3	O and S mixed
PU	S02-11	Tempered Martensite	3.0	O and S mixed
PV	S02-11	Heat-treated and water quenched Martensite	3.6	O and S mixed

[a]This sample solidified at 100 um/s.

white structure and the iron near the growth front which was in the form of austenite underwent the martensitic phase transformation. As a result, there were two interfaces formed on the sample rods, the solid/quenched melt interface and the interface between pearlitic and martensitic matrix structures. For the present experimental conditions, the latter was located 17 mm away from the former. Each part of a sample has a different thermal history depending on the relative location from the quench interface and the solidification velocity. In this experiment, it was desired to locate the fracture surface as close to the quench interface as possible in order to examine the segregation pattern which is least affected by later diffusion in the solid-state. Fracture samples in Experiment PH, PR and PS of Table 5 were, therefore, prepared by filing a V-notch in such a way that the segregation pattern at the iron/graphite boundary region present at a distance of 3 mm below the quenched solidification front. This corresponds to a cooling time in the solid of one minute and a temperature of around 1120°C. And the matrix had a martensitic structure. An unexpected result was found on analyzing the fracture surface of samples thus prepared. The results of Experiment PH, PR and PS were qualitatively the same and those obtained in Experiment PR are presented in Figs. 17. Figure 17a shows the surface topography as seen in a SEI image and Figs. 17b, c and d present the respective Auger maps for S (152 eV), O (510 eV) and Fe (650 eV). As can be verified in Fig. 17c, a significant amount of O presence was observed on the majority of the fracture surfaces of the samples having martensitic matrix structure. The Auger spectra taken from an O-rich area, point 1 of Fig. 17a, and from a S-rich area, point 2 of Fig.17a, are given in Figs. 18a and b, respectively. The spectra taken from the O-rich area show that the area is high in Fe but low in C and that the iron is present in the form of iron oxide. In most cases, S and O occurred at the same locations even at the area high in S as seen in Fig. 18b and the S covered area was greatly reduced. According to the results previously obtained with D

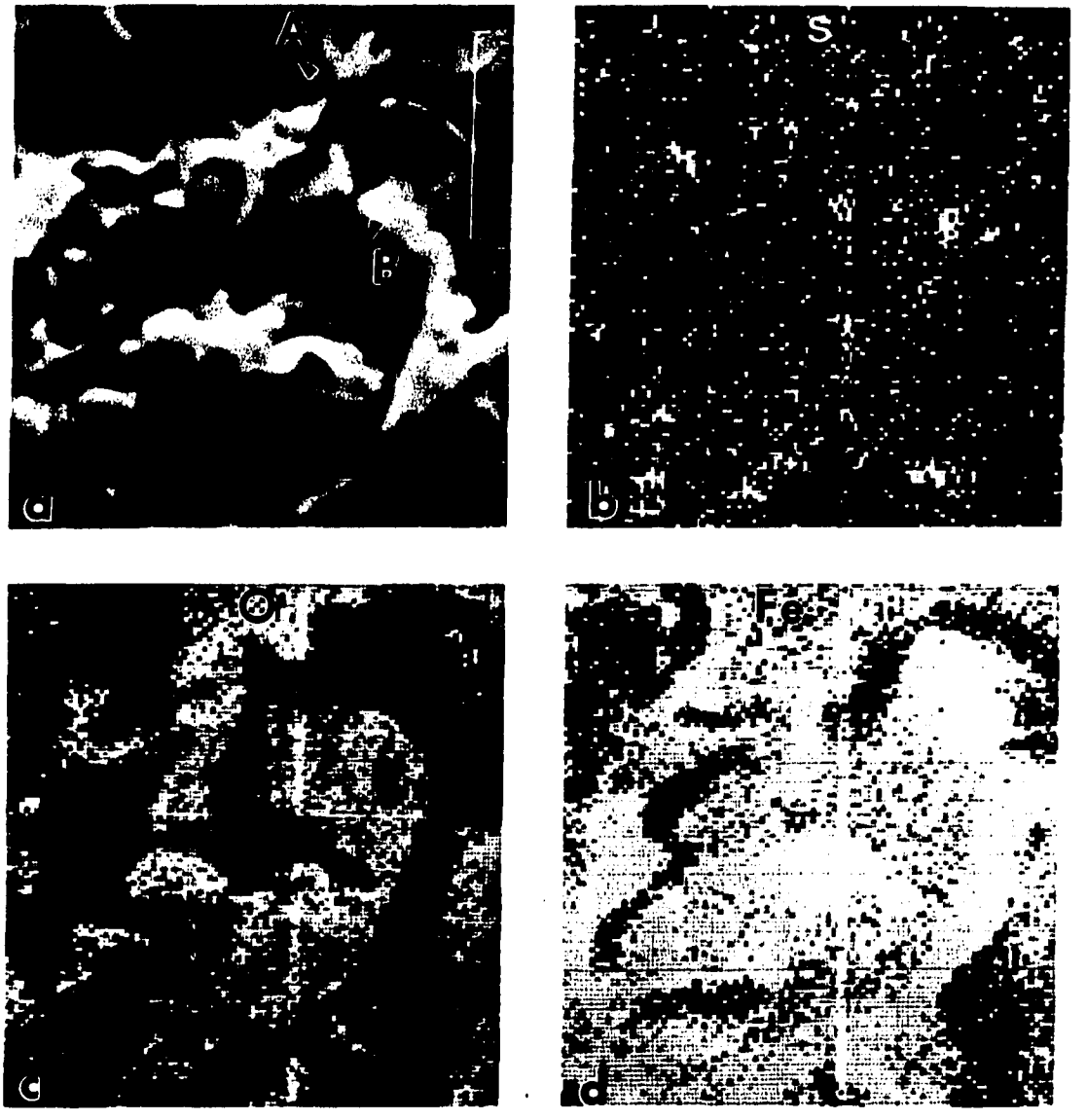

Figure 17. Auger analysis of type D martensitic gray iron fracture surface of Experiment S02-13, rate=50 um/s. (a) SEI image, (b), (c), (d) Auger elemental maps for O(510 eV), S(152 eV), and Fe(650 eV), respectively

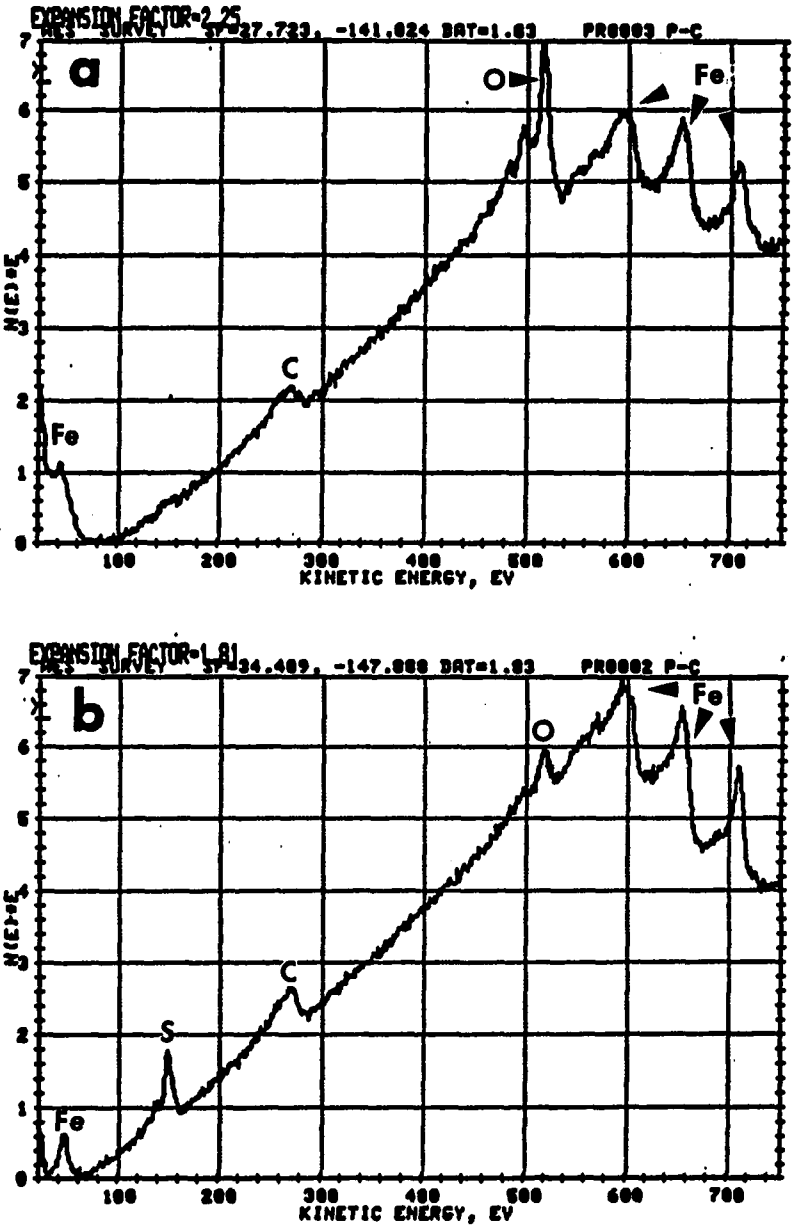

Figure 18. Auger spot analysis. (a) (b) Auger spectrum taken from point A and B of Fig. 17a, respectively

samples, no hint of O presence was detected. Concerning the discrepancies, it was suspected that the drastic martensite transformation on water quenching might have affected the segregation pattern. And another sample rod was directionally solidified in Experiment S02-12 at the same conditions but at this time quenched into air instead of water to terminate the solidification. The rod did not undergo the martensite transformation but the part near the quench interface showed fine pearlitic matrix structure. Two fracture samples were prepared; one, Experiment PJ, by placing a V-notch at a distance of 3 mm below the solidification front as in water quenched samples and the other, Experiment PK, taken away from the interface. The Auger analyses on both samples gave qualitatively the same results as those shown in Figs. 8, i.e., both S and Fe occurred in the same regions and those regions were low in C. No O was detected on the entire fracture surface.

In order to further study the effect of martensite transformation on changing the segregation pattern, a fracture sample in Experiment PQ was taken from between the two parts with which the above two samples in Experiments PJ and PK were prepared. Then, the sample was heat-treated at 950 ^{o}C inside a quartz tube filled with Ar, followed by quenching into the water to induce the martensite transformation. The Auger analysis gave the same result as obtained with the other water quenched samples. Additional experiments, PU and PV, were designed to test if the brittle nature of martensite had any effect on the fracturing process which might expose interfaces of another kind having a different segregation pattern. Two fracture samples were prepared from a rod originally pearlitic in matrix structure and heat-treated into martensite. One was annealed before fracturing, Experiment PU, and the other, Experiment PV, was fractured with no liquid nitrogen cooling in an attempt to reduce, in both cases, the brittle nature of martensite. The result was the same and O was still found in a significant amount. The above experiments

have shown that the high O is found in type D samples with a martensite matrix, and this is true:

1] if martensite is formed by direct quenching,

2] if martensite is formed by reheating the slowly cooled sample of pearlite matrix and then quenching, even though there was originally no O on the fracture surface of pearlite matrix before the heat-treatment,

3] if martensite is formed by very rapid quenching into the liquid Ga-In eutectic,

4] if martensite is tempered prior to fracture, and

5] if the fracture is done at room temperature without the liquid N_2 cooling.

DISCUSSION

The Auger analyses show that regions high in either S or O occur on the fracture surfaces of pearlite gray iron structures and that these regions are always associated with a high Fe signal and a low C signal. Analysis of the depth profiling experiments presents strong evidence that these are regions where the graphite flakes of the gray iron have pulled away from the iron matrix and that S or O is preferentially located on the Fe side of these iron/graphite interfaces. This is also supported by the fine markings found on those regions of A graphite gray iron, which may be associated with the growth steps of flake graphite such as those shown in Fig. 3 of Part III. In addition, the Auger spectra taken from those regions always show high energy Fe peaks of substantial intensity but a very weak C signal. The growth steps which were stopped growing by the iron phase may leave their trace as a relief on the mating iron surfaces. The S in elemental form provides roughly monolayer films on the interface regions and is observed in gray irons of the A and D flake graphite structures, which were studied here. However, the O is found only in gray irons of coarse type A graphite structures and exists in the form of iron oxide to provide 6~8 monolayer oxide films on the iron/graphite interface. The O adsorption, leading to the formation of iron oxide layers, occurs in many samples along the regions where the graphite growth steps used to be located while the S adsorption in those samples takes place out on the broad faces outlined by the O-rich regions. The two regions adsorbed by either O or S are strictly separated. This indicates that S and O compete for adsorption on the iron/graphite interface. It is interesting to note that the site competition on phase boundaries between the segregation of S and O occurs only in gray iron samples of coarse A graphite structures grown at a low rate from both high purity and S-added alloys. In high purity alloys, the increase in solidification velocity causes the transition in graphite morphology from type A to coral. On S addition to the high purity alloys, graphite changes

its structure from coarse type A to fine type A and then to type D flake morphologies as the rate is increased. The Auger data on pearlitic structures show that no O segregation occurs in fine type A and type D structures, and the iron/graphite interfaces are exclusively adsorbed by monolayer films of elemental S. Similar trends are also found on gray irons prepared in a commercial foundry by conventional casting. In commercial type A samples, the O adsorption on the interface is greatly extended because of the reduced S activity caused by elements forming sulfide particles. The commercial type D samples show no hint of O adsorption and the interfaces are exclusively covered by a thin S layer.

The experiments to test the possibility of solute segregation in solid state show that the segregation pattern initially set up at interfaces is not modified during the later cooling period, unless the iron matrix undergoes the martensitic phase transformation. The samples martensitic in matrix structure have wide regions of high O on the fracture surfaces regardless of graphite structures. In samples of a pearlite matrix, however, the high O regions in fracture surfaces are found only in gray irons having coarse type A graphite, and the iron/fine graphite interface regions are mostly covered with a S monolayer. The effect of martensite transformation on changing the segregation pattern observed in the fracture surface may be explained by considering two possible mechanisms by which the high O regions are exposed to be detected. First, plate martensite which forms at the high carbon levels which are present here contains many fine microcracks that are not difficult to observe under the optical microscope as shown in Fig. 19. Once the cracks are formed and create fresh surfaces during the transformation they may be contaminated by the O either present as an impurity in the quench operation, or when the samples were held in air before transfer to the Auger instrument, or when the samples were polished and etched to identify the interface position and evaluate the microstructures. Fracture may preferentially occur along those cracks and expose the O contaminated crack surfaces to be examined by Auger

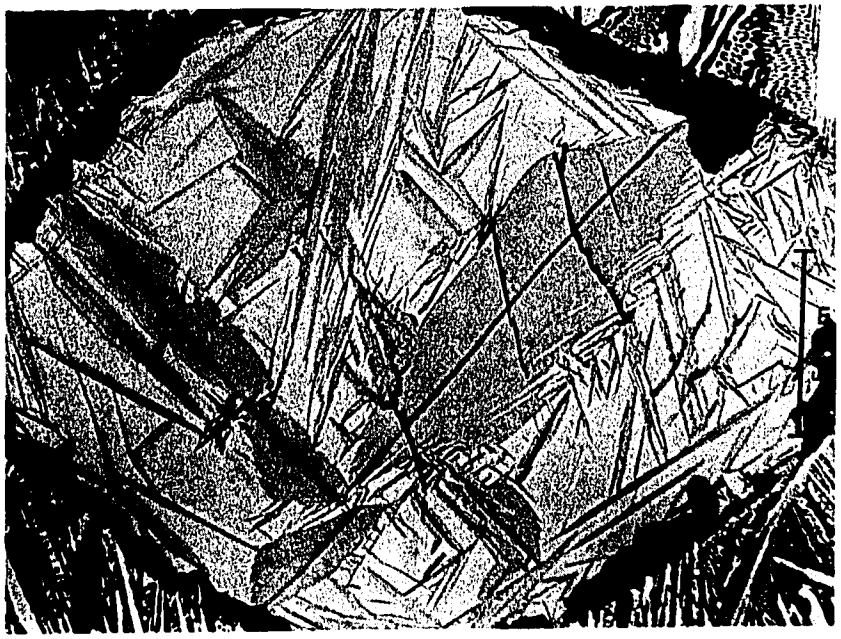

Figure 19. Optical micrograph showing quench cracks in a plate martensite of high C content (≈ 2 wt. %)

analysis. The results presented with reference to Fig. 17a show that the regions high in O are always a subset of regions high in Fe. This can be explained by referring to Fig. 19 which shows the cracked plate martensite surrounded by retained austenite. The fracture occurring along the cracks on the plate must propagate through the surrounding retained austenite. The fractured retained austenite would therefore be detected as a region high in Fe with no O contamination on a fracture surface, similar to the results of Fig. 17.

The second possibility includes the fact that it is well known that fresh martensite is extremely brittle, whether or not it displays cracked plates. Hence, once the martensite forms the presence of the sharp tips of the flake graphite will produce stress concentrations and it is likely that cracks will form at the iron/graphite interfaces, because of the brittle martensite/retained austenite matrix. Similar to the above argument, these cracked surfaces may be O contaminated before fracture in the SAM. Again, one would expect only part of the Fe fracture surface to be oxidized, as is the case in Fig. 17.

In either case, the segregation observed in the fracture surface has nothing to do with the one occurring at the solidification front in which this study is interested. Based on the results suggesting that martensitic phase transformation can lead to an erroneous conclusion in Auger fracture analysis by crack formation, special care must be taken in interpreting the Auger data. And the water quenching can not be used in an attempt to freeze the original segregation pattern at the interface. For the present study, air quenching seems to provide a proper means to avoid additional solute segregation in solid state during cooling since the sample cools fast down to the temperature regime where the diffusion rate is negligible. Since a V-notch was filed on the air quenched samples in such a way as to get a fracture surface at a distance of 3 mm from the solidification front, it can be concluded that the segregation pattern at the iron/graphite interface is determined either at the point of solidification or in solid state during the time 1 minute spent before quenching. Based on

the anticipated S enrichment at the solid/liquid interface along with the surface active nature of the element and the dramatic effect on microstructure which the S causes, it may be assumed that the S segregates to the iron/graphite interface at the solidification front between the molten iron and the graphite phase.

CONCLUSIONS

1. Auger fracture studies on the Fe-3.4C-2Si alloys with and without the addition of 0.02 % S show that the iron/graphite interface of coarse type A structures are preferentially adsorbed by S and O. The O adsorption occurs in many samples along the regions where the graphite growth steps used to locate, while the S adsorption in those samples takes place out on the broad faces outlined by the O-rich regions. The two regions adsorbed by either S or O are mutually exclusive, indicating that the S and O compete for adsorption sites on the iron/graphite interface. The adsorbed O is present in the form of iron oxide but the S in elemental form.

2. When the type A flake structure gets finer on increasing the solidification velocity or the graphite changes its morphology to type D, the iron/graphite interface is exclusively covered with a thin S layer with no hint of O adsorption.

3. Analysis of depth profiling experiments shows that the regions high in O are covered by 6~8 monolayers of iron oxide and those high in S by roughly one monolayer of S films.

4. Evidence is found that the quenching technique cannot be used to freeze the segregation pattern for the Auger study of cast iron because the martensitic phase transformation produced on quenching can lead to an oxygen contaminated fracture surface. Additional experiments are needed to verify this conclusion before the quenching experiments can be disregarded.

REFERENCES

1. Johnson, W. C.; Smartt, H. B. Met. Trans. A, 1977, 8, 553.

2. Francis, B. Met. Trans. A, 1979, 10, 21.

3. Franklin, S. E.; Stark, R. A. Mat. Res. Soc. Symp. Proc. 1985, 34, 25.

4. Seah, M. P.; Dench, W. A. Surface and Interface Analysis, 1979, 1, 2.

PART III. GROWTH STRUCTURE OF FLAKE GRAPHITE (TYPE A AND D) IN Fe-C-Si ALLOYS

INTRODUCTION

The most common type of graphite crystallized in the solidification of commercial purity Fe-C-Si alloys takes on a flake morphology, coarse type A and fine type D flake at the lower and higher range of growth rate, respectively. In an alloy of a given composition, the A⇒D transition is mainly governed by the cooling rate. And the critical rate required for the transition shows variation according to the addition of impurities such as S, Te and O. In high purity alloys, however, the transition upon increasing the rate is between type A and coral. The coral graphite has the same fine size as type D, but appears more of a highly branched rod structure as opposed to a branched plate structure of type D. The structure control in cast iron is, therefore, achieved during the solidification by causing a specific graphite morphology to dominate in growth. The selection of a certain type of graphite depends strongly on the impurities added and the cooling rate.

In many respects the morphological selection appears to be determined by the growth behavior of graphite itself although the presence of the metal phase, austenite, is not to be neglected. As an initial step to understand the growth behavior of graphite under the influence of impurities, S or Te, the graphite crystals themselves, grown at various solidification velocities, were carefully examined by optical microscopy, transmission and scanning electron microscopy. Several studies have demonstrated in type A flake graphite the occurrence of structural defects such as rotation stacking faults around the "c" axis of graphite and twin boundaries (1,2,3), which were understood to play an important role in the graphite growth. The structural defects observed in the studies, however, can not be used to explain the change of graphite morphology in terms of varying solidification velocities nor of impurities. They either used conventional casting (1) or did not pursue the effect of changing velocities (2), and did not have a close control over impurities to

investigate the effect of a specific element on graphite morphology. Furthermore the previous studies did not pay attention to type D flake graphite at all.

This study is mainly concerned with the growth structure of type A and D flake graphite in Fe-3.4C-2Si alloys. Trace amounts of S (0.02 wt. %) or Te (0.1 or 0.05 wt. %) were added in order to control the graphite growth behavior. A preliminary investigation of the coral growth structure occurring in high purity alloys was carried out only for the sake of comparison with the flake morphologies. A directional solidification technique was employed to solidify cast irons of the required graphite type since it provides particular advantages to control the solidification velocity and examine microstructures of crystallized graphite versus velocity. This study presents an evaluation of growth modes involved in the formation of flake graphite, both type A and D. And the effect of the impurity elements, S or Te, on the occurrence of the rotation stacking faults will be examined under various solidification velocities.

EXPERIMENTAL TECHNIQUE

Cast irons of type A and coral graphite were directionally solidified from the parent alloys made to a target composition of Fe-3.4 wt. % C-2 wt. % Si. The addition of S (0.02 wt. %) or Te (0.1 or 0.05 wt. %) was applied to the parent alloy in order to obtain type D graphite. Details of the alloy preparation and the solidification experiments and their results are included in Part I.

Graphite specimens were extracted from the directionally solidified sample by the dissolution of the iron matrix using 50 % hydrochloric acid. The type A graphite specimens were prepared from the samples solidified at 1 and 20 um/s. The S-induced type D specimens were prepared at two different rates, 50 and 100 um/s. The Te-induced type D specimens were prepared at 20 um/s. And the coral graphite was prepared from the sample solidified at 50 um/s. Part of the extracted graphite was examined in the as-extracted condition using a scanning electron microscope (SEM). The remaining part was ultrasonically cleaned in methane and collected on a C-coated Cu-grid for the transmission electron microscopy (TEM). Optical examination was carried out only on type A graphite.

Specimens for the graphite fracture analysis were prepared from samples containing type A, D and coral morphologies. A V-notch was filed into the cast iron sample at right angles to the solidification direction and samples were broken in air and then loaded into the chamber of an SEM. Stereopairs were taken from the fracture surface in two directions 6° apart to perform a three dimensional evaluation of the fracture characteristics of graphite.

RESULTS

The unique appearances of type A, D and coral graphite solidified from a cast iron eutectic are best illustrated by the stereopairs shown in Figs. 1a, b and c, respectively. The stereopairs in Fig. 1 are the secondary electron images taken from deep etched polished surfaces having a growth direction normal to the page. The type A and the coral graphite, in Fig. 1a and c, were solidified from the high purity alloys at 1 and 50 um/s, respectively. The type D in Fig. 1b was solidified at 20 um/s from the Te-doped alloys. The S-induced D graphite showed similar appearances to the Te-induced D graphite. The empty spaces seen in the stereographic view of the figures were originally filled with the metallic phase which was removed during etching. The metallic phase is therefore more isolated in flake A and D graphite than in coral graphite, by thick stiff-looking plates in type A and by thin curved plates in type D. It is important to notice in Figs. 1a and b the huge difference in size and thickness between type A and D graphite flakes. Figure 2 is included to show the size differences between type A and D flakes at the same magnification. Type D flakes are almost two orders of magnitude smaller than type A flakes. In coral graphite, however, the graphite itself looks more isolated, and the connection between parts of the graphite is not so complete as in flake.

The growth mechanism of each individual plate of A graphite was investigated. Figure 3 is an optical micrograph of a graphite flake exposed by deep etching on the surface of a sample rod directionally solidified at 1 um/s. The flake as a whole is made up of many parts each of which consists of many thin sheets stacked together on their broad face. The major growth direction of the sheets is in general parallel to the solidification direction indicated by the arrow. A bright field image, Fig. 4a, taken from extracted A graphite also shows the presence of a few stacks of thin sheets which look similar to those in the optical micrograph, Fig. 3. An electron diffraction pattern, Fig. 4b, taken from the selected area

Figure 1. Stereopairs of SEI images taken from extracted graphite of (a) type A flake morphology grown at 1 um/s. Solidification direction normal to the page

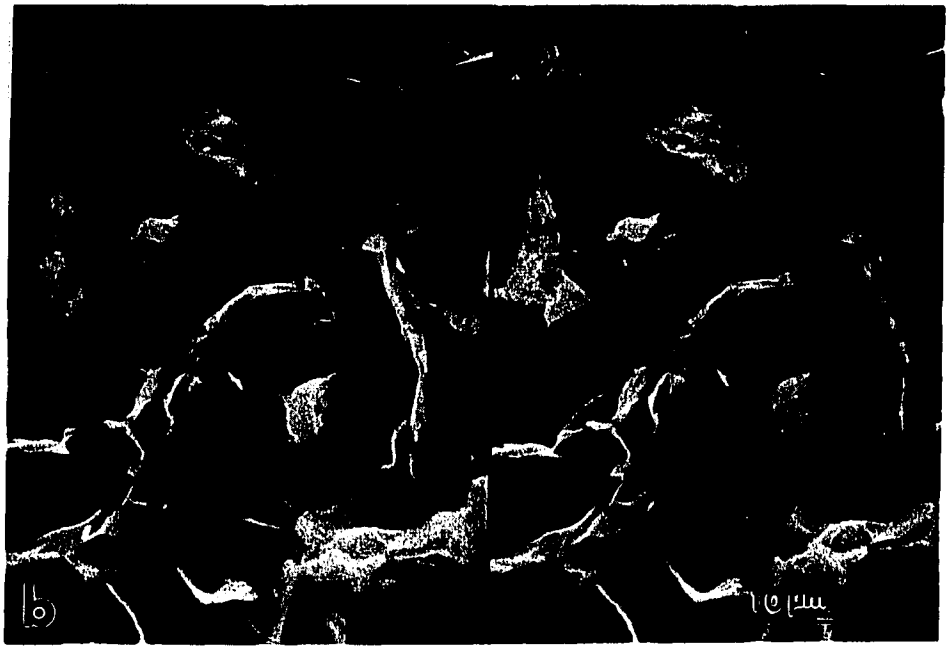

Figure 1. (continued) (b) Type D flake morphology grown at 100 um/s. Solidification direction normal to the page

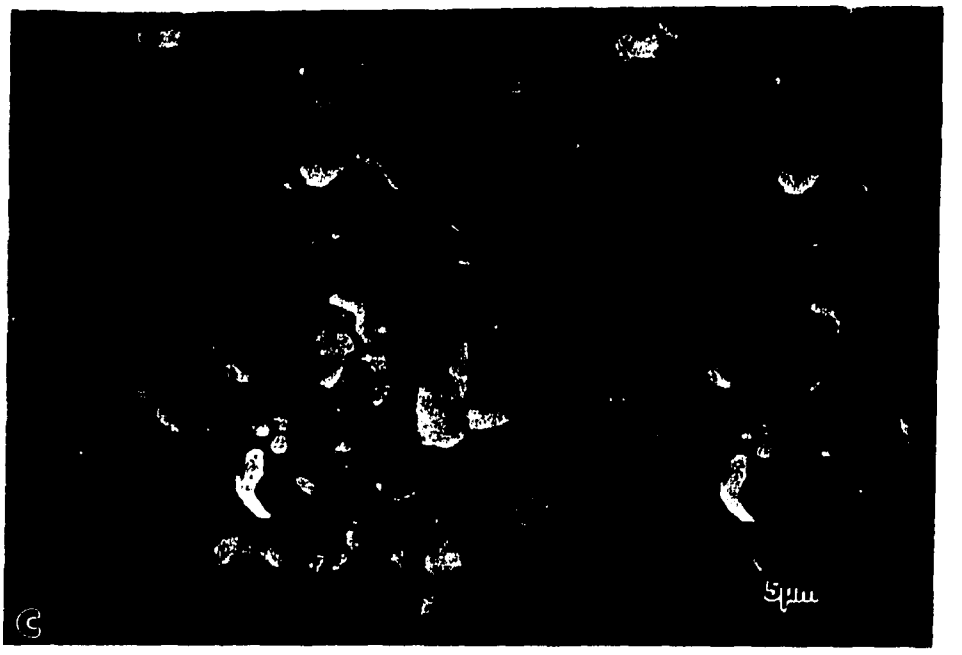

Figure 1. (continued) (c) Coral morphology grown at 50 um/s. Solidification direction normal to the page

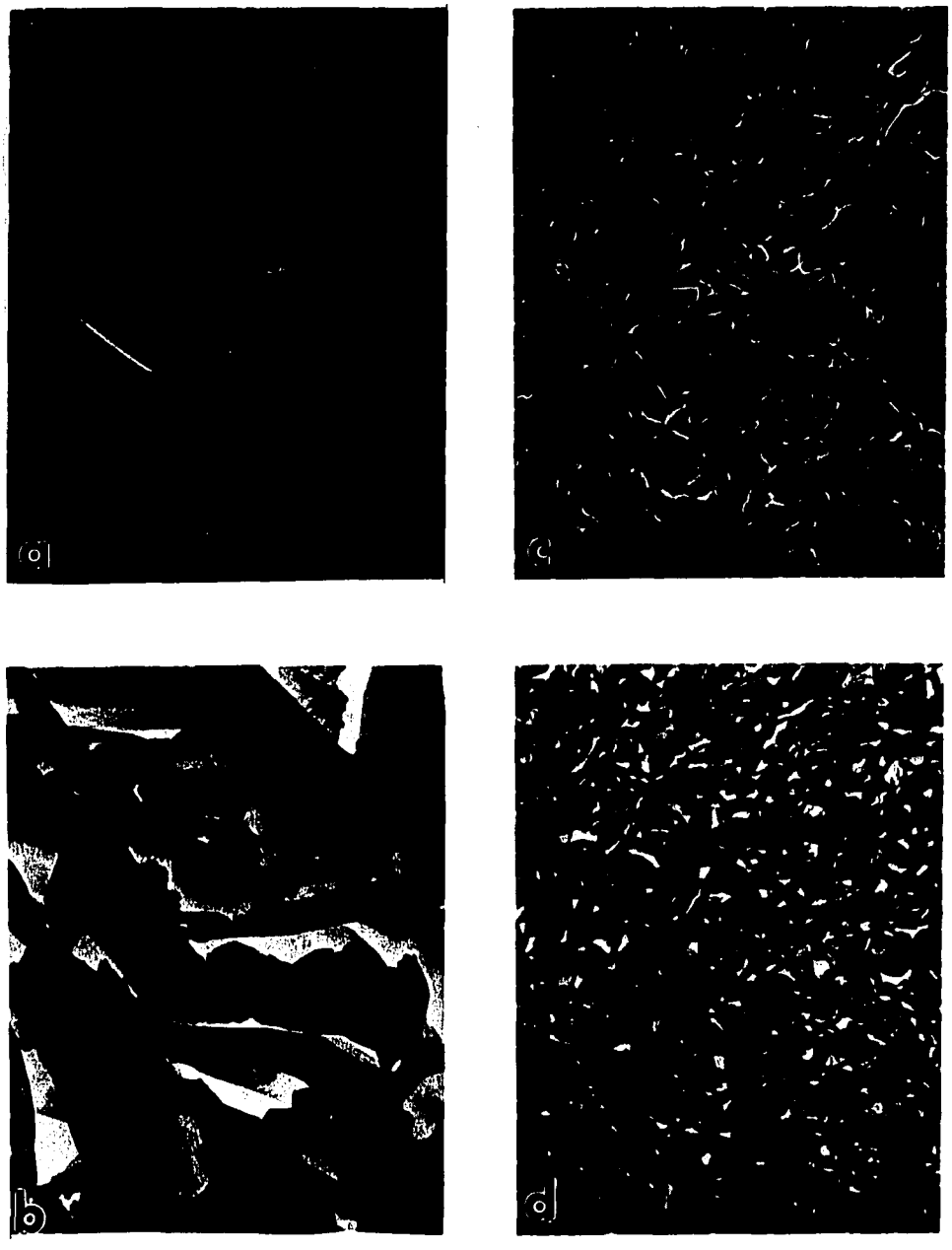

Figure 2. Secondary electron images taken from extracted graphite. Solidification direction normal to the page, 20 um/s, 400X (a) type A flake grown from a S-added alloy, (b) inverted image of (a), (c) type D grown from a Te-added alloy, (d) inverted image of (c)

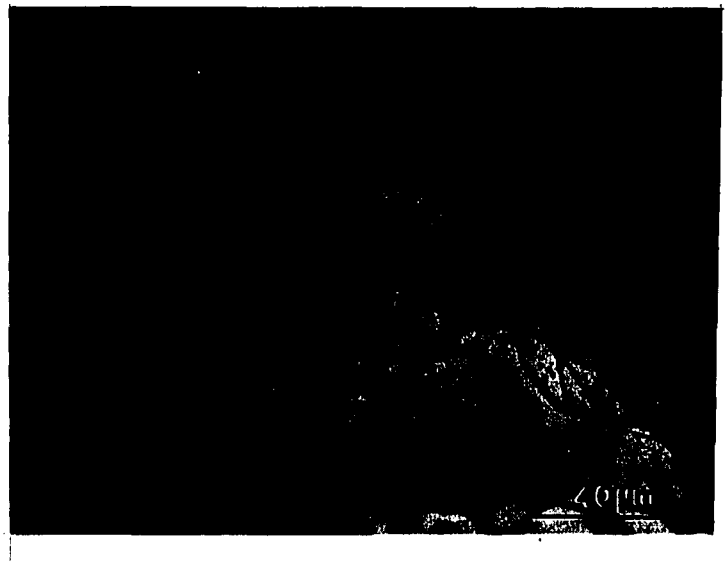

Figure 3. Optical micrograph of type A graphite exposed by deep etching on the surface of a sample rod directionally solidified at 1 um/s. Solidification direction to the right, 500X

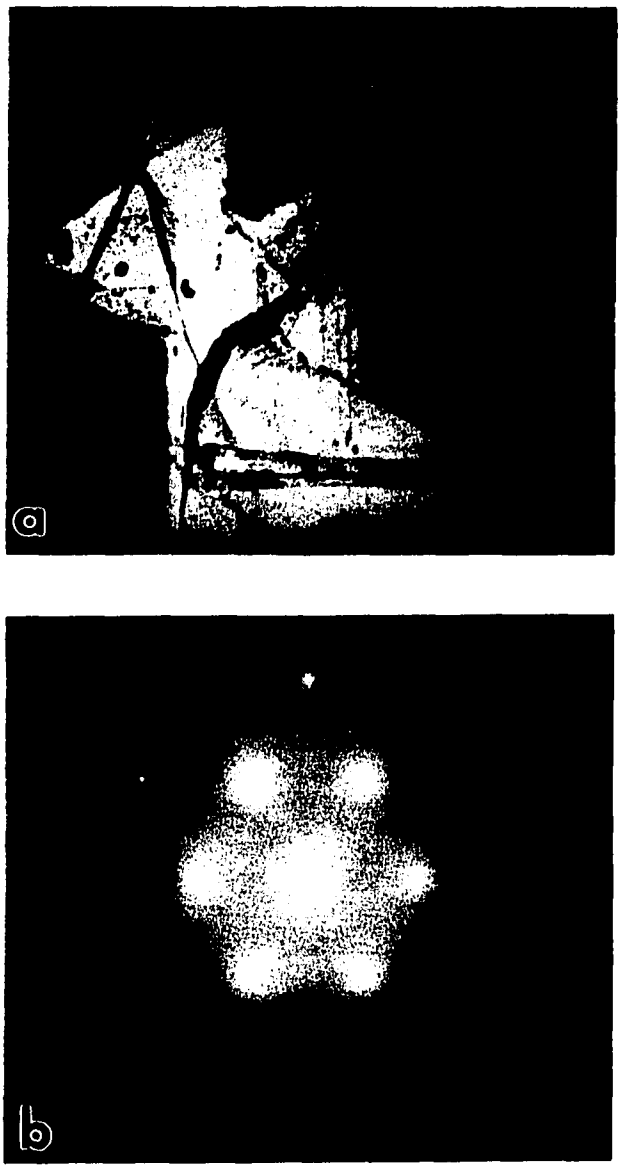

Figure 4. Bright field image and electron diffraction pattern taken from a type A graphite flake solidified at 1 um/s. (a) Bright field image, 4500X, (b) electron diffraction pattern of <0001> zone axis reflections from the dotted area of Fig. 4a

shown as a dotted circle in Fig. 4a provides direct evidence that the sheets have been formed parallel to the basal plane of graphite. The diffraction spots in Fig. 4b are the ones from <0001> zone axis reflections. The basic growth unit is, therefore, safely considered to be a thin graphite sheet whose broad face is parallel to the basal plane of graphite. The term basal sheet is used to denote the basic growth unit in this study.

The optical microscopy on extracted type D graphite was not very fruitful except for producing direct evidence that D graphite observed from a polished surface as shown in Fig. 5a consists of many fine graphite flakes connected together. Figure 5a was taken from the polished surface of the piece of bulk graphite shown in Fig. 5b, which was extracted from a cast iron sample of D graphite. The furrows in the bulk piece used to be filled with the proeutectic austenite dendrite arms and were exposed during extraction. The nature of the individual fine flakes, connected together to form D graphite, was then investigated utilizing TEM. Most type D flakes were thin enough to be transparent to electrons of 120 keV in contrast to type A flakes which were generally opaque with an occasional thin area observed at their edges. The stereopair shown in Fig. 6a consists of two bright field images taken from a D flake in two directions 8° apart. Stereographic viewing of the figure reveals that the flake is significantly curved as if it tries to wrap up the incident electron beam. And the middle flat part of the flake is seen to lie deep in the bottom at almost right angles to the incident beam. The selected area diffraction pattern, Fig. 6b, taken in the middle flat portion of the flake includes two sets of <0001> zone axis reflections rotated 30° about the zone axis. It seems reasonable to conclude from investigating the micrographs in Fig. 6 that the central part of the graphite flake consists of two basal sheets rotated 30° relative to each other. The diffraction patterns observed most frequently in type D graphite resemble the one in Fig. 6b with variations in the degree of rotation. The D flakes are therefore considered to be mostly made of a few basal sheets stacked together

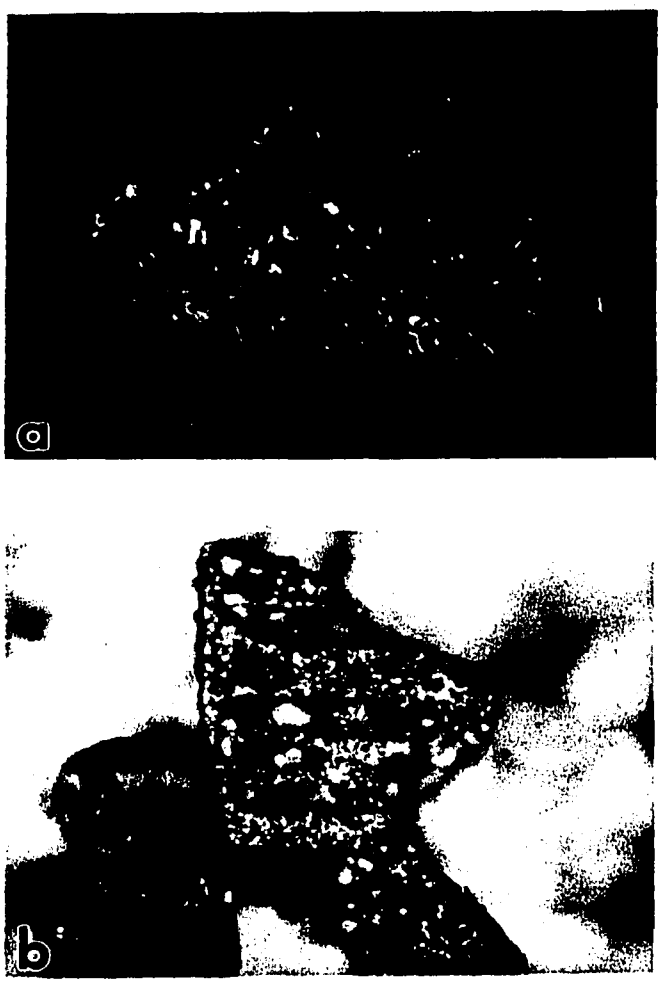

Figure 5. Optical micrograph of extracted type D graphite flakes. (a) Taken from the polished surface of a piece of bulk graphite such as shown in Fig. 4b, 1000X, (b) bulk type D graphite samples, 200X

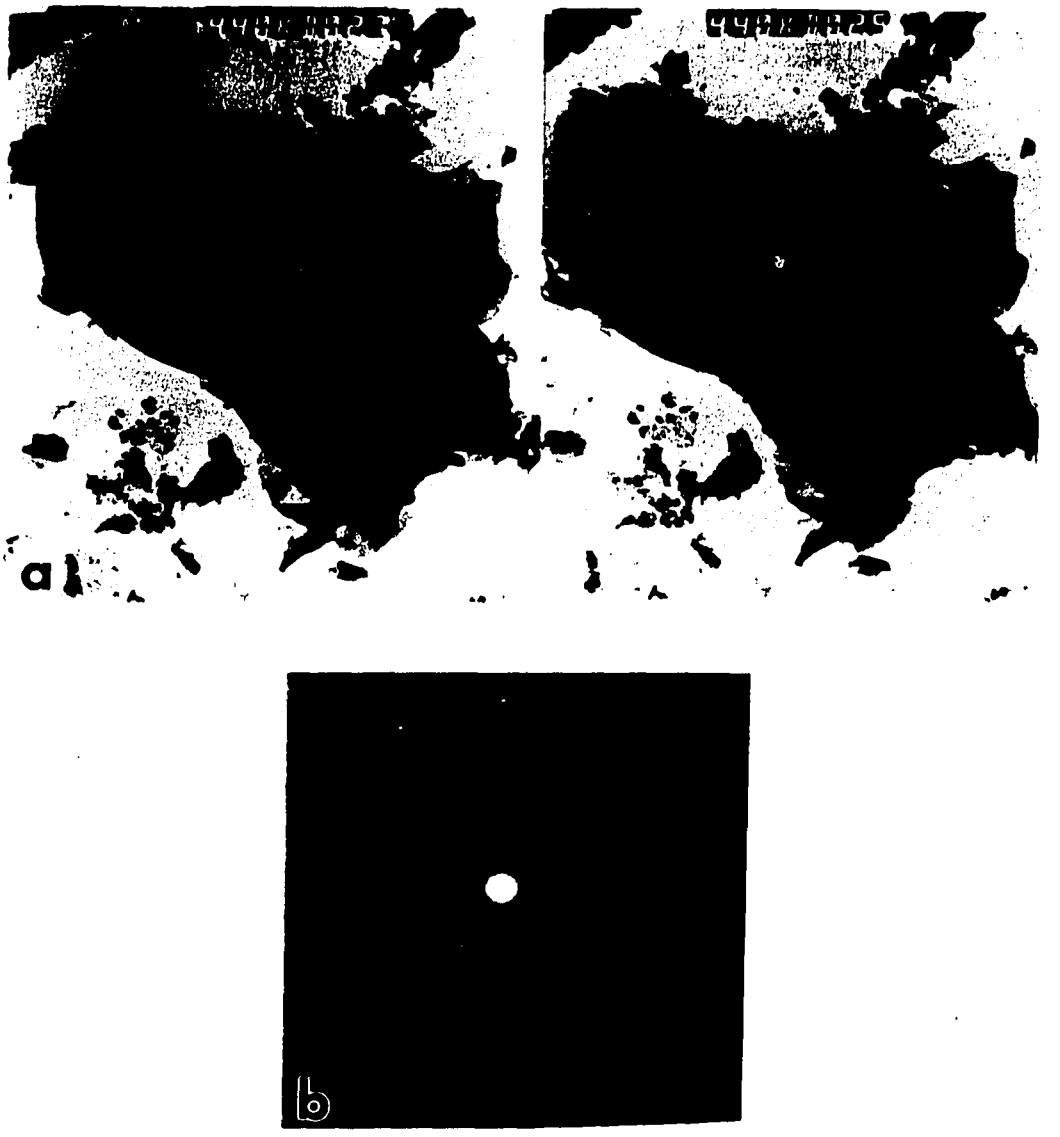

Figure 6. Stereopair of TEM bright field images and electron diffraction pattern taken from a type D graphite flake. (a) Bright field image, 4400X, (b) electron diffraction pattern of <0001> zone axis reflections taken from the dotted area of Fig. 6a

with some rotation stacking faults present between them. Each individual basal sheet is estimated to be less than a thousand Å in thickness, the penetration depth of electrons at 120 keV being less than a few thousand Å.

The nice development of basal sheets such as observed in the A and D flake graphite is absent in coral graphite. Figure 7 presents a TEM stereopair of coral graphite. Stereographic viewing of Fig. 7 gives the impression that the growth occurs in a more isolated manner and the connection between branches of graphite is more localized. The diffraction patterns most typical in coral graphite are presented in Figs. 8a and b. The spots in Fig. 8a result from $<01\bar{1}0>$ zone axis reflections, which means that the crystal within the area selected by the aperture is oriented with the "c" axis at right angles to the incident beam, if not tilted. In the flake type graphite observed in this study, it was a rare event to have the "c" axis aligned at right angles to the incident beam. The nice development of the basal sheets in type A and D graphite almost always causes the flakes to sit on the Cu-grid with the "c" axis parallel to the incident beam. The diffraction pattern in Fig. 8b shows that there are several crystals in the selected area, the innermost ring constructed by the reflections from [0002] plane sets. The area selected by the aperture used in the present study is approximately 1 um in diameter. In flake graphites, the diffraction pattern does not change over different locations in an area of a few 10's um in diameter in type A and several um in type D. In coral graphite, however, the diffraction pattern changes as soon as the selected area is moved. In addition, the selected area sometimes contains several crystals of different orientation.

Fracture surface analyses were also carried out on cast irons of type A, D and coral graphite by taking stereopairs using an SEM. Figure 9 presents two sets of stereopairs taken from the fracture surface of A graphite cast iron, the fracture occurring nearly perpendicular to the solidification direction. Figure 9a allows three dimensional

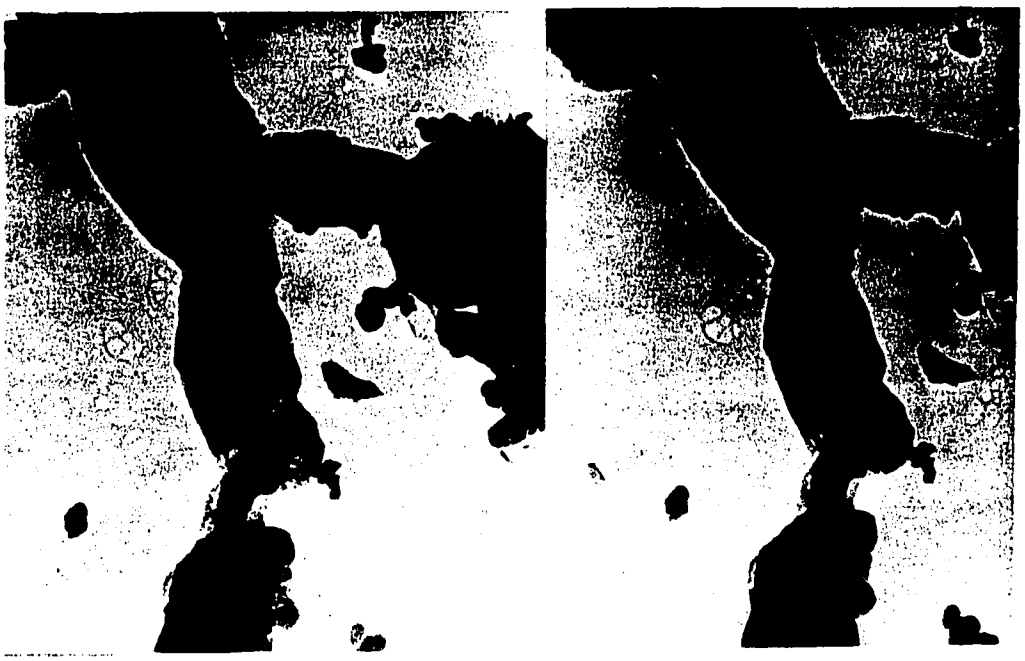

Figure 7. Stereopair of TEM bright field images taken from coral graphite, 17000X

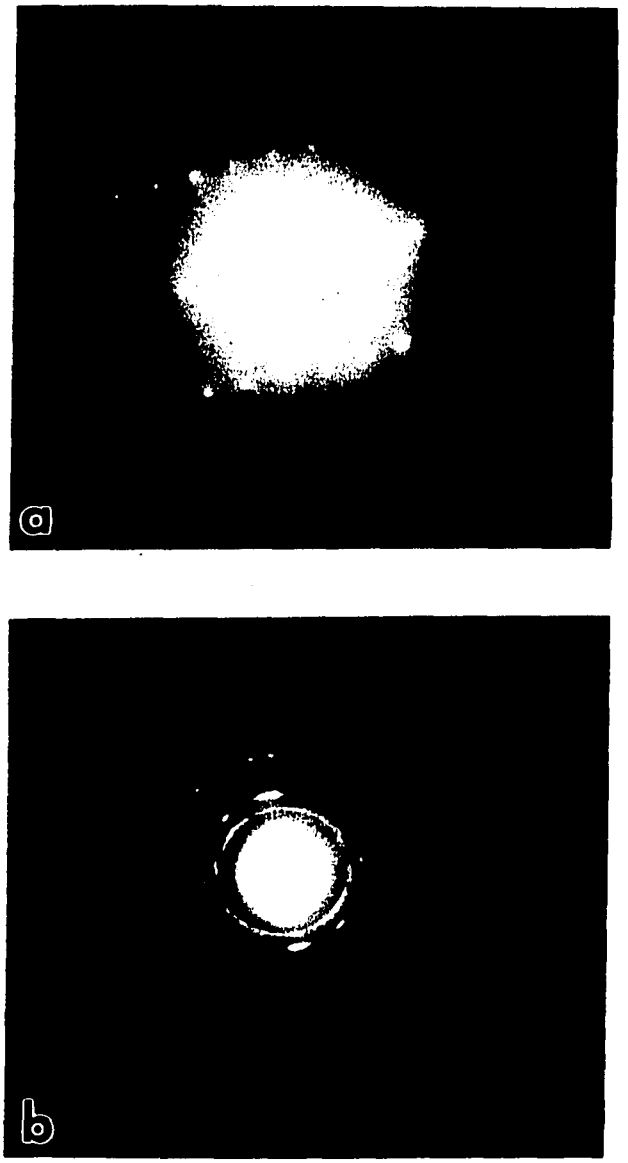

Figure 8. Electron diffraction patterns taken from coral graphite. (a) <0$\bar{1}$10> zone axis reflections, (b) the innermost ring constructed by reflections from [0002] plane sets in several crystals

Figure 9. Stereopairs of SEI images taken from fracture surface of type A graphite cast iron solidified at 1 um/s. (a) 282X, solidification direction normal to the page

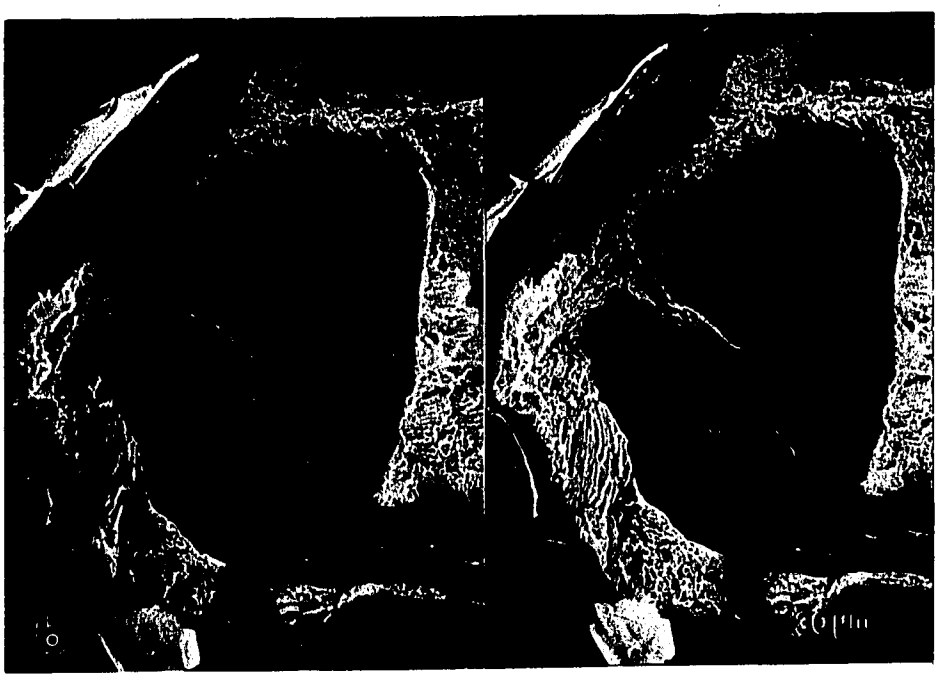

Figure 9. (continued) (b) 746X, solidification direction normal to the page

examination of graphite flakes broken along the broad faces and exposed on fracturing. Figure 9b, another stereopair, clearly shows the stacking of many growth steps to make a big flat flake. Important features to be noted in Fig. 9 include; (1) The thick graphite flakes show a substantial ability to bend around the neighboring iron phase although they consist of many layers each of which shows significant flatness, and (2) Transgranular fracture through the iron phase, showing typical ductile microvoid coalescence structures, occurs along with the fracture through the graphite. The fracture surface of D graphite cast iron is presented in Fig. 10. Stereographic viewing of Fig. 10 indicates that the fracture surface consists of many irregularly shaped grains a few um in size with some delaminated graphite sheets protruding over the surface. The previous work with Auger spectroscopy established that the irregular grains are the iron matrix covered with thin graphite layers, and the D graphite does not allow fracture to occur transgranularly through the iron matrix but only through the graphite or along the iron/graphite interface. The stereopair from the fracture surface of coral graphite cast iron, Fig. 11, shows many broken graphite debris, much finer than those observed on the fracture surface of D graphite cast iron.

Results on the occurrence of rotation stacking faults in A and D graphite are summarized in Table 1 as a function of impurity elements added and also of the solidification velocities. The stacking faults were observed by taking diffraction patterns from a small area selected by the aperture. The selected area in this study were approximately 1 um in diameter. In some cases, use was made of a convergent beam 100 Å spot size and still stacking faults of the same kind were observed. Typical diffraction patterns showing the presence of stacking faults with various rotation angles are presented in Fig. 12. The patterns include two or more sets of <0001> zone axis reflections rotated a certain degree about the "c" axis of the hexagonal crystal structure of graphite. Bollmann (4,5) and Minkoff and Myron (6) calculated possible rotation angles from pure

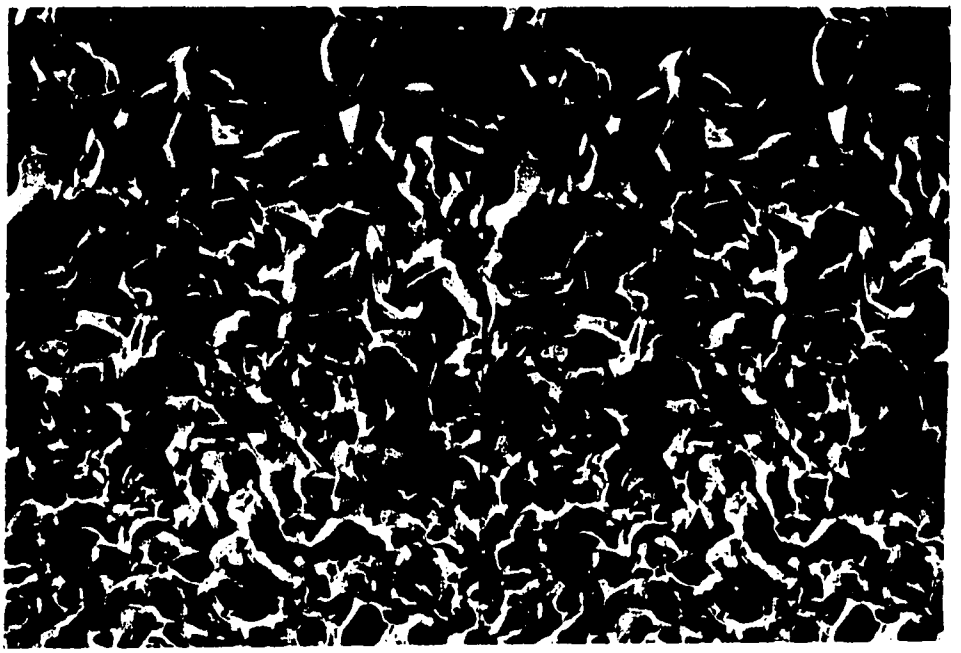

Figure 10. Stereopair of SEI images taken from the fracture surface of type D graphite cast iron solidified at 50 um/s. Solidification direction normal to the page, 1250X

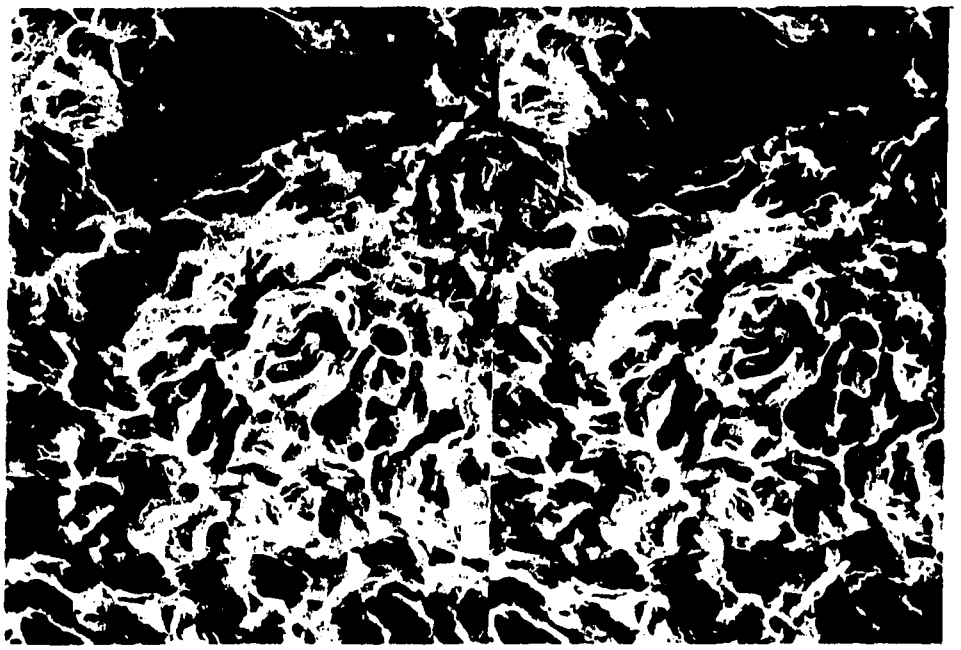

Figure 11. Stereopair of SEI images taken from the fracture surface of coral graphite cast iron solidified at 50 um/s. Solidification direction normal to the page, 1960X

Table 1. Occurrence of rotation stacking faults in graphites grown from Fe-3.4C-2Si alloys

Graphite morphology	Purity	Solidification rate [um/s]	Probability of fault occurrence # fault cases/ # total cases
Type A	High purity	1	5/52 (10 %)
	S-added	1	14/104 (13%)
		20	32/100 (32 %)
Type D	S-added	50	103/115 (90 %)
		100	116/122 (95 %)
	Te-added	20	155/167 (93 %)

Table 2. Rotation angles predicted for hexagonal lattices by the modified coincidence boundary theory (3)

Rotation angle (°)	Area of the coincidence lattice/ Area of the atomic lattice
21.8	7
27.7	13
13.2	19
17.86	31
9.44	37
15.16	43
16.48	49
7.34	61
24.4	67
11.64	73
27.84	79
6.0	91
5.04	127

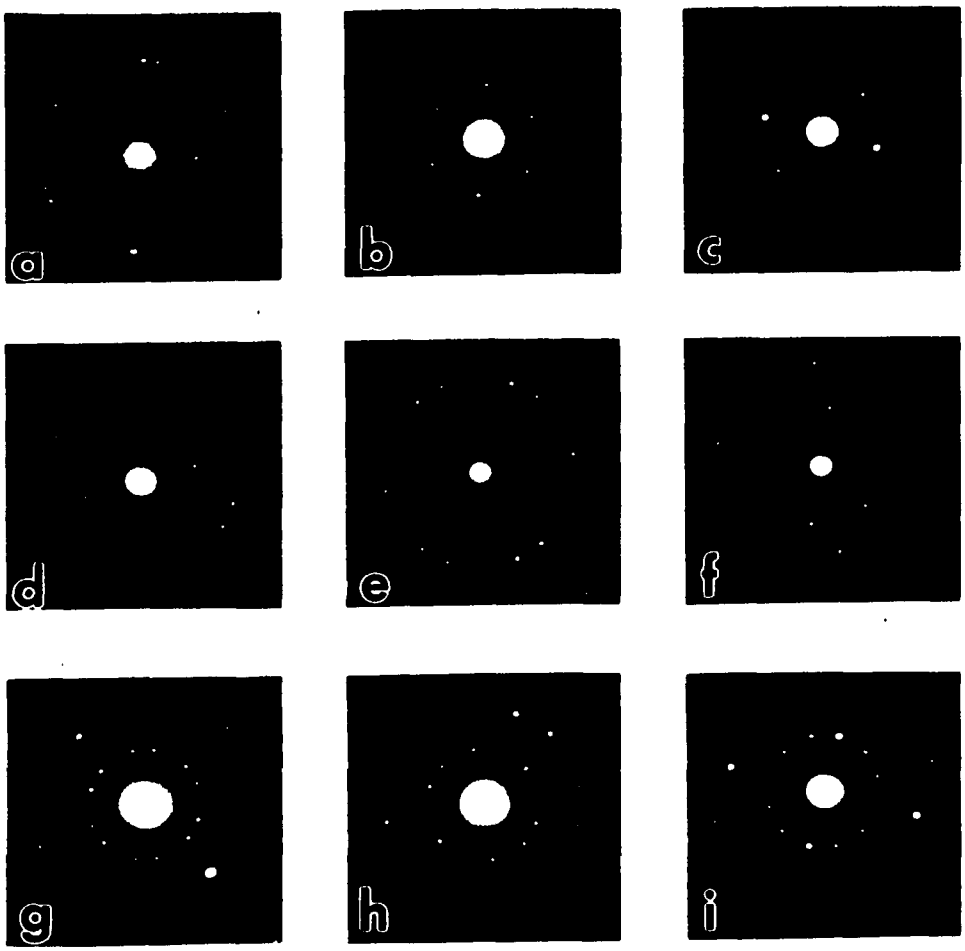

Figure 12. Electron diffraction patterns taken from type D graphite flakes having stacking faults of various rotation angles. (a) 9.5, (b) 11.5, (c) 13.5, (d) 15, (e) 16.5, (f) 18, (g) 22, (h) 24, (i) 28°

geometrical considerations based on the partial coincidence boundary concept. Table 2 lists the predicted rotation angles in the order of decreasing coherent site density. The diffraction patterns presented in Fig. 12 verify the presence of some of the rotation angles predicted by the theory.

According to Table 1, the occurrence of rotation stacking faults amounts only to 10 % of the cases investigated in A graphite, grown at 1 um/s in both high purity and S-added alloys. Most 1 um/s samples investigated were free from any kind of defects. Diffraction patterns such as shown in Fig. 4b could be obtained from flakes a few 10's um in size. Stacking faults occur more frequently as the rate is increased, about 30 % frequency at 20 um/s in S-added alloys. It was shown in Part I that it is not possible to grow A graphite at rates above 2.5 um/s in alloys with no S-addition. The rotation angles of 22°, 13.5° and 16.5° were most frequently observed in A graphite as presented in Fig. 13. The A⇒D transition in graphite morphology is reported in Part I to occur at around 50 um/s in S-added alloys. The S-induced D graphite samples were therefore prepared from cast iron solidified at 50 um/s. The frequency of occurrence of rotation stacking faults in type D shows a sharp increase up to 90 % of the total cases investigated. Further increase in the solidification velocity to 100 um/s after the A⇒D transition causes a small increase in the frequency of stacking faults to 95 %. The major effect of the increase in velocity from 50 to 100 um/s is on the distribution of the rotation angles. Figure 14 shows that in 50 um/s samples, the rotation angles are distributed among the top five angles listed in Table 2. In 100 um/s samples, however, 5 additional angles were observed over the ones which were operative in 50 um/s samples. It has been established that when Te is added to the parent alloy, D graphite is induced at much slower rates than with the S addition (7). In the absence of the 10% H_2 + Ar atmosphere, Te causes the formation of D graphite to start as low as 5 um/s. The Te-induced D samples were prepared from cast iron solidified at 20

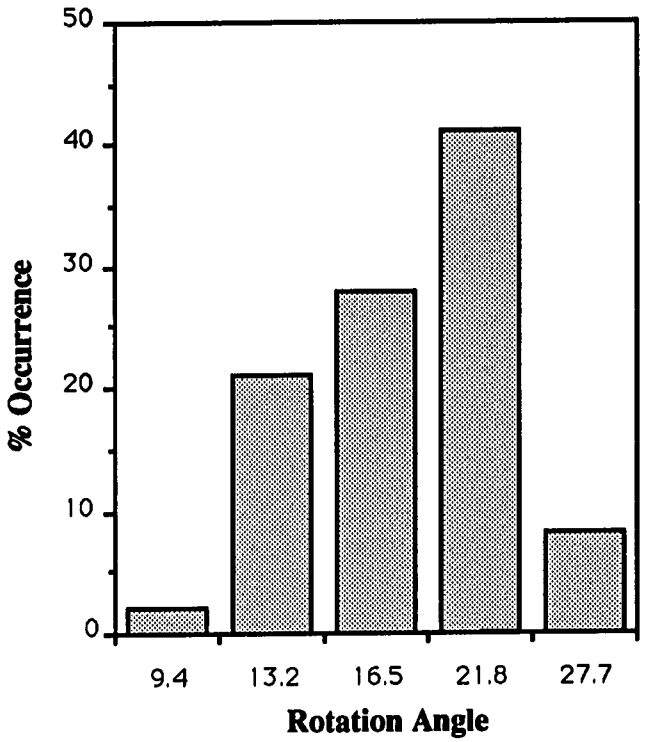

Figure 13. Occurrence of stacking faults in type A graphite versus rotation angle

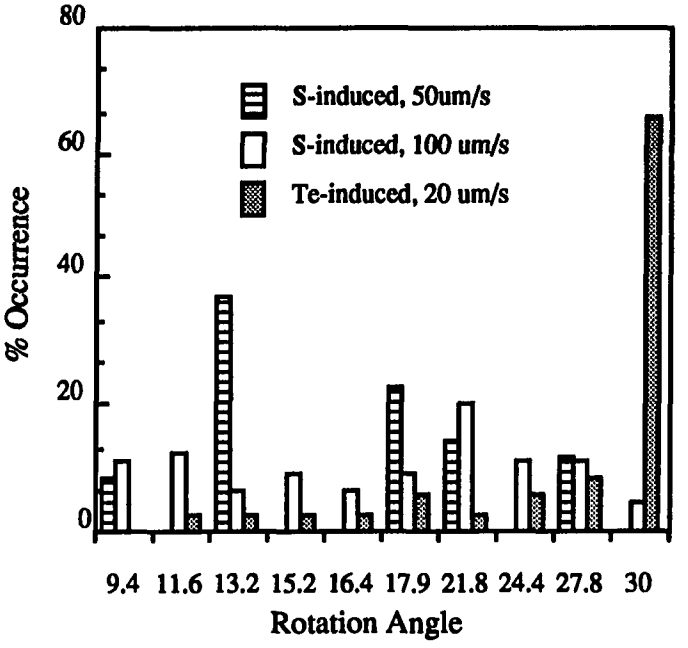

Figure 14. Occurrence of stacking faults in type D graphite versus rotation angle

um/s since at higher rates it is possible for the gray-white transition to occur. Rotation stacking faults were observed in 93 % of the total samples investigated. Although the frequency of fault occurrence does not show a significant difference between the S-induced and the Te-induced D graphite, a noticeable trend in the distribution of rotation angles was observed in Te-induced D samples; More than 60 % of the cases showing the presence of stacking faults had the rotation angles between 28° and 30° as shown in Fig. 12. The diffraction pattern shown in Fig. 6b is the very one most frequently encountered in Te-induced D graphite samples. The rotation angle measured in Fig. 6b is close to 30°.

DISCUSSION

The experimental results show that the flake graphite grown from cast iron eutectic consists of stacks of thin growth layers in both A and D graphite. The broad face of each layer was verified in Figs. 4b and 6b to be parallel to the basal plane of graphite, causing the layer to be named basal sheet. The roughly hexagon-like growth steps found in Figs. 3, 4a and 9b support the general belief that each basal sheet is developed by a ledge growth along the "a" axis of a graphite crystal. The basal sheets are stacked along the broad face in a unique way to produce either A or D graphite. It was also verified in Fig. 4b and 6b that the stacking can be achieved either with or without a crystal mismatch present between the constituent basal sheets. The most common crystal mismatch observed was a rotation stacking fault resulting from two adjacent basal sheets rotated in stacking by a certain degree relative to each other. The preferential selection of specific rotation angles was predicted on the basis of geometric considerations. The basis of this theory is that low energy configurations between crystals are probable for orientations which place atoms in similar coordinate states, the energy being lowest when the density of coordination sites is highest.

The results obtained from the fracture surface analysis again confirm the layered structure of flake graphite both in type A and D. It has been established that the broad face of each growth layer is parallel to the basal plane of graphite and that there may or may not be crystal mismatch such as rotation stacking faults existing between the layers. It is known that graphite fractures preferentially on basal planes, and hence it is reasonable to expect the iron/graphite interfaces to be the preferred fracture sites, as seems to be the case in Figs. 9a and b. The major difference between A and D graphite discovered in fracture analyses is that fracture occurs both at iron/graphite interfaces and through the iron matrix in type A, but it only occurs at iron/graphite interfaces in type D (except, of course, through

primary dendrites). This may be due to the close spacing and highly connected and curved morphology of the type D graphite, compared to larger, planar and less well connected type A graphite. The freedom of type D graphite to change the growth direction with little difficulty seems to be related to the thin nature of type D graphite plus the frequent fault formation.

Table 1 shows conclusively that the occurrence of rotation stacking faults is governed by the type of graphite flake, solidification velocity and impurity elements added. The A⇒D transition in graphite morphology is accompanied by a remarkable increase in the frequency of fault formation. In type A samples grown at the lower rate 1 um/s, the S addition seems to have little effect on the fault formation. The effect of increasing velocity on faults in A graphite can be investigated only in S-added alloys because in high purity alloys the A⇒coral transition occurs at low rates. The growth of A graphite at higher rates on S addition is discussed in Part I. The increase in velocity from 1 to 20 um/s in S-added alloys increases the probability of fault occurrence from 13 to 32 %. The rate increase in the S-induced D graphite from 50 to 100 um/s also causes an increase, although small, in the frequency of fault formation. The velocity increase to 100 um/s in D graphite has a remarkable effect on the distribution of rotation angles observed. Additional rotation angles were observed to be selected in fault formation over the ones operative in 50 um/s samples. The effect of Te on the faults in D graphite is clearly distinguished from that of S in that the stacking faults of a specific rotation angle close to 30° occur most frequently on Te addition.

CONCLUSIONS

1. Strong evidence has been produced in Figs. 3, 4, 6 and 9 that in the directional solidification of Fe-3.4C-2Si alloys, the flake graphite, both type A and D, grows by stacking of the basic growth units. The freedom for the D graphite to change growth direction with little difficulty compared to type A may be related to its extremely small thickness, which is approximately two orders of magnitude smaller than type A, plus the frequent fault formation.

2. Electron diffraction patterns taken from the extracted A and D graphites confirmed that the broad face of the basic growth layers is parallel to the basal plane of graphite and that there may or may not be crystal defects such as rotation stacking faults existing between the layers stacked.

3. It has been verified that the most common crystal defects observed in flake graphite is the rotation stacking faults. The fault formation is encouraged with the increasing solidification velocity and shows a sharp increase in frequency upon the A⇒D transition. In S-added alloys, the rate increase from 1 to 20 um/s causes the probability of fault occurrence in A graphite to increase from 13 to 32 %, and in D graphite the rate increase from 50 to 100 um/s raises the probability from 90 to 95 %.

4. It has also been observed in S-induced type D samples that the increase in solidification velocity from 50 to 100 um/s causes additional rotation angles to be operative in the fault formation. Over the angles, 9.4, 13.2, 17.9, 21.8 and 27.8°, which were observed in 50 um/s samples, the angles, 16.4, 24.4 and 30°, were additionally observed in 100 um/s samples.

5. When Te, instead of S, was added to induce type D graphite, the rotation angle close to 30° was most frequently selected, about 60 % of the cases investigated, in the fault formation.

REFERENCES

1. Purdy, G. R.; Audier, M. "The Physical Metallurgy of Cast Iron", 3rd Intl. Symp., Stockholm, Sweden, 1984, 13.

2. Double, D. D.; Hellawell, A. "The Metallurgy of Cast Iron", 2nd Intl. Symp., Geneva, Switzerland, 1974, 509.

3. Oron, M.; Minkoff, I. "Recent Research on Cast Iron", ASM Seminar, Gordon and Breach, New York, N. Y., 1968, 173.

4. Bollmann, W. Phil. Mag., 1962, 7, 1513.

5. Bollmann, W. Phil. Mag., 1967, 16, 363.

6. Minkoff, I.; Myron, S. Phil. Mag., 1969, 19, 379.

7. Verhoeven, J. D.; Park, J. S.; Jones, L. L. Met. Trans., 1989, 20A, 1867.

PART IV. EFFECT OF H AND O ON THE POTENCY OF Te TO PROMOTE WHITE IRON IN THE SOLIDIFICATION OF Te-DOPED Fe-C-Si ALLOYS

INTRODUCTION

It has already been established by Dawson's experiments (1,2,3) with a high purity gray iron that H improves the ability of Te to suppress the formation of gray structures. His work was initiated by observing that the amounts of Te additions required to produce white iron structures were much greater in the moisture free laboratory tests than in the tests with molds that contain moisture. In his experiments, the H content in Te-doped alloys was deliberately increased before pouring, either by bubbling H_2 gases through the melt or by using a slightly damp ladle. And the solidification was carried out in air in conventional casting experiments. Concerning the mechanism by which H promotes white iron in the presence of Te, Dawson did not give any clear explanation. He stated that the carbide-promoting effects must be due to the combined effects of Te and H when present simultaneously. In view of the tendency of Te to react with O, it seemed advisable to carry out experiments with controlled amounts of H. In experiments with no control over the solidification atmosphere as in Dawson's, it is extremely difficult to estimate the effects produced by the reactive gaseous elements, O and H, dissolved in the melt. Fortunately the present study could obtain a clearer picture about the H effect by taking advantage of the ability to control the solidification atmosphere.

In the previous study (4,5) on the effect of Te to promote white structure in the directional solidification of Fe-C-Si alloys, the Te effect was found to be reduced when the solidification atmosphere was enriched in O content by the inadvertent use of O-contaminated Ar. The present study was carried out to collect more convincing experimental results which might lead to a clearer understanding of the role played by O and H modifying the Te effect. The behavior of Te in cast iron solidification was investigated under various atmospheres differing in terms of H_2 and O_2 content.

EXPERIMENTAL TECHNIQUE

Cast irons of three different compositions were prepared; (1) Fe-3.4C-2Si, (2) Fe-3.93C-1Si, and (3) Fe-4.28C-0.25Si. The compositions were chosen to allow a constant carbon equivalent. This means that in each alloy the C composition is shifted the same amount below the C composition of the eutectic trough. The Te doping was applied to the parent alloys (1) by 0.1 wt.% and (2) by 0.05 wt.%, but not to the alloy (3). The alloy (3) was prepared to examine the H effect on structure control in the absence of Te. Details of the alloy preparation and the solidification experiments are included in Part I. The G⇒W or W⇒G transition rates were measured and used as a tool to represent the effectiveness of Te to promote white structures under five different solidification atmospheres. The solidification atmosphere was controlled in terms of H_2 and O_2 content.

The directional solidification experiments were carried out in a hard fired, high-purity Al_2O_3 tube with one end closed, containing a cast iron sample in it. The desired atmosphere could be provided by use of the proper gases to fill the tube during solidification. The O-rich atmosphere was obtained using 10 vol.% O_2 plus balance Ar and the H-rich atmosphere using 10 vol.% H_2 plus balance Ar. The O- and H-rich atmosphere will be hereon referred to as "10% O_2+Ar" and "10% H_2+Ar", respectively. Another way to control the H content in the solidification atmosphere was accidentally found, which, incidentally, led to this controlled study. The directional solidification experiments were previously carried out in Al_2O_3 tubes with both ends open. The lower end of the tube was closed using a vacuum seal epoxy, positioned inside of the cold finger as schematically shown in Fig. 1 of Part I. It turned out that when pure Ar was used to fill the containment tube, the epoxy appears to have acted as a H source and produced the same effect as the H-rich environment in both gray and white solidification, but with slightly less effectiveness. The position of the epoxy was such that it became quite warm and it is assumed here that a

gas, rich in H, was evolved. Therefore, it is assumed that an environment having a limited H_2 supply was set up using pure Ar to fill the Al_2O_3 tube which had one end closed with an epoxy. This will be hereon referred to as "epoxy end+Ar" atmosphere. In several experiments under epoxy end+Ar atmosphere, the O content was increased by using O-contaminated Ar containing O_2 up to 1 % instead of pure Ar to fill the tube. This gas was a welding grade Ar which was used in the initial experiments of this study (6). In all experiments O was considered to be provided either by the inherent O content in the alloys or by the possible reduction of the Al_2O_3 tube wall in contact with cast iron melt at high temperatures. Therefore, the use of pure Ar to fill the closed end Al_2O_3 tube came to provide a solidification atmosphere of another kind where the O activity might be relatively high even without the deliberate O_2 addition. This will be hereon called "pure Ar" atmosphere.

RESULTS

The potency of Te to promote white iron was measured in terms of the solidification velocity required to induce the gray-to-white (G⇒W) or white-to-gray (W⇒G) transition. Most experiments with the Fe-3.4C-2Si-0.1Te alloys were carried out previously and reported elsewhere (4). The experiments under pure Ar and 10% H_2+Ar atmospheres were additionally performed on the alloys and the results are presented in Table 1. Consider the experiment JP1-29 run under 10% H_2+Ar atmosphere to illustrate the rate sequence information. The controlled solidification was begun at 5 um/s for 5mm and then the rate was stepwise increased up to 100 um/s after a certain length, indicated in the parentheses, was solidified at a given rate. The acceleration in rates induced the G⇒W transition, where possible, and allowed the G⇒W transition rate to be determined, 5 um/s in this experiment. In addition, the white structures induced on acceleration served as a necessary prerequisite for the following W⇒G transition experiment carried out by decreasing the rate, in steps, down to 2.5 um/s. And the W⇒G transition occurred at 2.5 um/s. The sample in experiment JP1-30 was solidified under pure Ar atmosphere and the resulting structure was all gray, indicating that a rate above 100 um/s is required to cause the G⇒W transition. In experiment JP1-31, the sample was solidified under 10% H_2+Ar atmosphere and the structures were all white, placing the W⇒G transition rate at <2.5 um/s. Table 2 summarizes the G⇒W and W⇒G transition rates versus solidification atmospheres in experiments carried out on Fe-3.4C-2Si-0.1Te alloys, using the data from reference 4 and Table 1. It is apparent that the increasing O_2 influence in atmosphere, provided by the decrease in H_2 content, raises the rate required to solidify the white structures. Under the pure Ar atmosphere where no deliberate O_2 enrichment was applied, the Te effect was almost completely neutralized and could not induce white structures even above 100 um/s. Accordingly experiments under 10% O_2+Ar atmosphere were not tried. Another thing to

Table 1. Results of the G-W and W-G transition experiments with Fe-3.4C-2Si-0.1Te alloys

Expt.#	Rate Sequence Information Rate in um/s (Run Dist. in mm)	Atmosphere	G⇒W	W⇒G
JP1-29	5(5)-50(20)-100(20)-50(20)-10(15)-5(15)-2.5(10)	10% H_2+Ar	5	2.5
JP1-30	5(5)-50(20)-100(25)-50(20)-20(20)-10(15)	Pure Ar	> 100	All gray
JP1-31	5(5)-50(20)-100(25)-50(20)-10(15)-5(10)-2.5(3)	10% H_2+Ar	All White	< 2.5

Table 2. The transition, G-W and W-G, rates versus solidification atmospheres in Fe-3.4C-2Si-0.1Te alloys

Atmosphere	G⇒W (um/s)	W⇒G (um/s)
10% O_2+Ar	N.I.	N.I.[a]
Pure Ar	> 100	-
epoxy end+Ar with O-contaminated Ar	$50 < V_{g-w} < 120$	$5 < V_{w-g} < 50$
epoxy end with pure Ar	$5 < V_{g-w} < 90$	5
10% H_2+Ar	$< \approx 5$	< 2.5

[a]Not investigated.

be noted in Table 2 is that the range of transition rates is in general smaller in W⇒G experiments than in G⇒W experiments if carried out under the same condition. This result was most evident in the experiments with epoxy end and pure Ar atmosphere.

Based on the experimental results obtained with Fe-3.4C-2Si-0.1Te alloys, another set of experiments was performed on the Fe-3.93C-1Si-0.05Te alloys. The Te addition was cut in half (0.05 wt.%) since the alloy contained less Si (1 wt.%) and was expected to solidify white structures more easily. Experimental results under 4 different solidification atmospheres are presented in Table 3. Experiments under epoxy end+Ar atmosphere using O-contaminated Ar were not pursued and only the W⇒G transition was investigated this time. In experiments under a pure Ar atmosphere, it was found that the solidification microstructure was all gray in JP2-1 with no white iron induced up to 150 um/s and that when the white iron was initially established in JP2-2 and 3 the structure was not completely white but mottle which persisted down to 50 um/s. The W⇒G transition under epoxy end+Ar atmosphere occurred at 2.5-5, 4 and <5 um/s in experiments JP2-5, 6 and 7, respectively. The experiment JP2-5 placed the transition rate between 2.5 and 5 um/s. The next experiment JP2-6 was designed to obtain the exact transition rate which turned out to be 4 um/s. Another experiment JP2-7 confirmed that the W⇒G transition did not occur down to 5 um/s. Three experiments were also carried out under 10% H_2+Ar atmosphere. The first two experiments, JP2-8 and 9, produced all white structures, placing the W⇒G transition rate at <2.5 um/s. And the W⇒G transition under 10% H_2+Ar atmosphere was found to occur at 1 um/s in experiment JP2-10. The structure solidified under 10% O_2+Ar atmosphere, experiment JP2-11, was all gray and no hint of white iron was observed up to 150 um/s. Table 4 summarizes the W⇒G transition rates versus the solidification atmosphere using the data in Table 3. The H effect enhancing the potency of Te to promote white iron was demonstrated by the remarkable decrease in the W⇒G transition rates under

Table 3 Results of the W-G transition experiments with Fe-3.93C-1Si-.05Te alloys

Expt.#	Rate Sequence Information Rate in um/s (Run Dist. in mm)	Atmosphere	W⇒G Tran.(um/s)
JP2-1	5(5)-150(10)-100(10)-50(20)-10(20)-5(20)-2.5(20)-1(10)	Pure Ar	All Gray
JP2-2	250(15)-150(15)-100(15)-50(15)-10(15)-5(15)-2.5(15)-1(10)	Pure Ar	Mottle down to 50
JP2-3	200(20)-100(20)-50(20)-5(15)-2.5(15)-1(10)	Pure Ar	Mottle down to 50
JP2-5	100(25)-10(25)-5(25)-2.5(25)	epoxy end+Ar	2.5-5
JP2-6	100(25)-10(25)-5(25)-4(25)	epoxy end+Ar	4
JP2-7	100(25)-50(25)-10(25)-5(25)	epoxy end+Ar	< 5
JP2-8	100(15)-50(15)-10(25)-5(25)	10% H_2+Ar	< 5
JP2-9	100(25)-10(25)-5(25)-2.5(25)	10% H_2+Ar	< 2.5
JP2-10	100(13)-50(13)-10(13)-5(15)-2.5(15)-1(25)	10% H_2+Ar	1
JP2-11	150(20)-100(20)-50(15)-10(15)-5(15)-2.5(18)-1(8)	10% O_2+Ar	All Gray

Table 4. The W-G transition rates versus solidification atmospheres in Fe-3.93C-1Si-0.05Te alloys

Atmosphere	W⇒G transition rate (um/s)
10% O_2+Ar	> 150
Pure Ar	> 50 (mottle at > 50)
epoxy end + O-contaminated Ar	N.I.[a]
epoxy end + pure Ar	4
10% H_2+Ar	1

[a]Not investigated.

both epoxy end+Ar and 10% H_2+Ar atmosphere. The white structures initially induced in the experiments maintained its growth down to 4 um/s in epoxy end+Ar and 1 um/s in 10% H_2+Ar atmosphere.

The effect of H on the W⇒G transition was examined in the absence of Te with the Fe-4.28C-0.25Si alloys. The Si content was reduced to 0.25 wt.% in order to establish the white iron growth with no Te doping. Since the W⇒G transition can occur only at very low rates, 1 um/s or below, in pure Fe-C alloys regardless of the solidification atmosphere, the Si addition by 0.25 % was necessary to evaluate the H-effect on the transition. Table 5 presents the experimental results. The two experiments run under 10% H_2+Ar atmosphere, JP3'-1 and 3, produced completely gray cast iron with no hint of white structures up to 150 um/s whereas in experiment JP3'-2 under pure Ar atmosphere the W⇒G transition occurred at 10 um/s. Table 6 summarizes the G⇒W transition rate versus atmosphere using the data in Table 5. It can be seen in Table 6 that H by itself has a tendency to promote gray iron when present alone in the absence of Te.

Table 5 Results of the W-G transition experiments with Fe-4.28C-0.25Si alloys

Expt.#	Rate Sequence Information Rate in mu/s (Run Dist. in mm)	Atmosphere	G⇒W Tran.(um/s)	W⇒G Tran.(um/s)
JP3'-1	150(20)-100(20)-50(15)-10(15)-5(15)-2.5(10)-1(5)	10% H_2+Ar	> 150	All Gray
JP3'-2	100(25)-50(25)-10(15)-5(15)-2.5(15)-1(10)	Pure Ar	-	10
JP3'-3	5(5)-50(20)-100(20)-50(20)-20(15)-10(15)-5(10)	10% H_2+Ar	> 100	All Gray

Table 6. The W-G transition rates versus solidification atmospheres in Fe-4.28C-0.25Si alloys

Atmosphere	G⇒W transition rate (um/s)	W⇒G transition rate (um/s)
Pure Ar	-	10
10% H_2+Ar	> 150	All gray

DISCUSSION

The experimental results show that control of the solidification atmosphere with gases containing H_2 or O_2 has a remarkable influence on the resulting microstructure of Te-doped Fe-C-Si alloys. The increased H_2 or O_2 content in the atmosphere is expected to raise the H or O concentration dissolved in cast iron melt at the high temperatures (see appendix). Table 2 shows that the potency of Te to promote white irons is dramatically diminished in the Te-doped Fe-3.4C-2Si alloys with the restriction of the H supply or with the increase in O content. The alloys undergo a G⇒W transition at $V_{g\text{-}w} < 2.5$ um/s when the stable H supply is secured in the melt throughout the solidification by the 10% H_2+Ar atmosphere. When the location of the H source is biased at the bottom of the tube and the H supply becomes limited and less stable in the epoxy end+Ar atmosphere, the alloys undergo the transition at higher rates, $5 < V_{g\text{-}w} < 90$ um/s and $V_{w\text{-}g} = 5$ um/s. And the transitions occur at even higher rates when small amount of O_2 is deliberately introduced in the epoxy end+Ar atmosphere, $50 < V_{g\text{-}w} < 120$ um/s and $5 < V_{w\text{-}g} < 50$ um/s. Upon the complete removal of the H_2 source from the melt in pure Ar atmosphere, the white structures are not induced even above 100 um/s. In all the experiments the O presence could not be avoided on account of the inherent O content in alloys. Probably the Al_2O_3 containment tube may also contribute to increase the O level at high temperatures. The pure Ar atmosphere is therefore believed to provide a significant O activity although no O is supplied. It has been established that the G⇒W transition in undoped cast irons containing 2 % Si occurred at around 2000 um/s (7,8). Hence, it is apparent that small additions of Te to high purity hypoeutectic 2 % Si irons reduce both $V_{g\text{-}w}$ and $V_{w\text{-}g}$ by factors of 500 or more only when the O activity in the molten alloy is suppressed in one way or another. In addition, the increased O or the decreased H influence causes the transitions to occur quite randomly, particularly in G⇒W transitions. For instance, the G⇒W transition occurred in

a range of V_{g-w} =5 to 90 um/s in epoxy end+Ar atmosphere with pure Ar and V_{g-w} = 50 to 120 um/s in epoxy end+Ar atmosphere with O-contaminated Ar.

The experiments with the Te-doped Fe-3.93C-1Si alloys confirmed the influence of H and O on the effectiveness of Te modifying the solidification microstructures. The alloys undergo the W⇒G transition at lower rates than the 2 % Si alloys, at 1 and 4 um/s under 10% H_2+Ar and epoxy end+Ar atmosphere, respectively, apparently because of the reduced Si content. The reduced Si allowed the white formation, although not complete but mottle, in pure Ar atmosphere at > 50 um/s, which was not allowed with 2 % Si alloys above 100 um/s. In 10% O_2+Ar atmosphere, however, the Te effect is shown in Table 4 to be neutralized even in 1 % Si alloys and the white growth is not induced up to 150 um/s.

It can, therefore, be concluded that the Te is most effective at inhibiting the gray formation when under strong H influence but it is easily neutralized with the increasing O activity. The present results indicate that the enhanced effectiveness of Te in the H presence has a close relationship with the O activity in melt. The work of Verhoeven and coworkers (5) suggested that the critical action of the Te in retarding the gray iron growth results from Te atoms precipitating out of the cast iron melt onto either the melt/graphite interface or the melt/graphite/iron trijunction. Such action requires the Te to be dissolved in solution in the melt. The element Te is, however, very reactive so that it would oxidize at relatively low O activities in the cast iron melt. Once oxidized it seems unlikely that it would be effective at inhibiting the growth of the graphite phase. Hence, the action of the H must be mainly to reduce the O activity and thereby increasing the concentration of Te dissolved in the cast iron melt at the freezing interface. This view is further supported by the experiments with the undoped Fe-4.28C-0.25Si alloys, showing that H by itself has no power to promote white iron. The alloys undergo the G⇒W transition at 10 um/s when the pure Ar gas is used. But no white structures are induced up to 150 um/s under the 10%

H_2+Ar atmosphere. The H, therefore, has a tendency to promote gray instead of white structures when no Te is added.

Additional evidence of H-O interaction has already been presented in Part I in discussing the effect of O on structure control in gray solidification. The effect of H there was presumably to suppress the O activities at the solidification front, allowing the growth of type A flake graphite at higher rates than with high O levels. It appears that in cast iron solidification, in both gray and white, the effect of H on microstructures must be understood by considering its interaction with O.

Some analytical methods also support that the oxidation of Te could reduce its effectiveness (6). The O content determined by vacuum fusion analyses was higher at the finish than at the start of the solidified sample rods. Three rods of 2 % Si alloys were analyzed and the average value was 110 ($\sigma = \pm 53$) and 463 ppmw ($\sigma = \pm 301$) at the start and at the finish, respectively. The Te content, however, did not show any significant difference at the two ends in wet chemical analysis. The average value was 433 ($\sigma = \pm$ 8.5) at the start and 402 ppmw ($\sigma = \pm 40$) at the finish. Since the chemical analyses do not distinguish the Te either in elemental or in compound form, it may be concluded that the decreased potency of Te near the end of the experiments results from the interaction between O and Te, most likely by oxidation of Te.

CONCLUSIONS

1. Directional solidification experiments with the Te-doped Fe-3.4C-2Si alloys have established that the potency of Te to promote white structures is substantially reduced without the H supply. The alloys undergo the G⇒W transition at < 5 um/s and the W⇒G transition at < 2.5 um/s in an atmosphere of 10 vol.% H_2 + Ar. When a small amount of H is presumably added from the hot epoxy the transition rates rise to values as high as 50 to 100 um/s. With complete removal of H they rise to values > 100 um/s.

2. The influence of atmosphere control upon the Te effect was also examined in Fe-3.93C-1Si alloys in a study of only the W⇒G transition. Similar results were obtained to the 2% Si alloys. The 10% H_2 + Ar atmosphere allowed white growth down to 1 um/s; pure Ar produced only a mottled structure at high rates and the white component disappeared at rates of 50 um/s; an atmosphere of 10% O_2 + Ar did not allow white growth to the highest rates studied, 150 um/s. The results show that H promotes the stabilizing effect of Te upon white growth while O inhibits it, similar to the 2% Si alloys.

3. It is strongly suggested that the H-O interaction improves the effect of Te for the promotion of growth of white iron. If it is assumed that once oxidized the Te loses its power to suppress the gray growth, as seems likely, the H enhances the potency of Te in a way somewhat indirect, i.e., by inhibiting the oxidation of Te or by reducing Te compounds to increase the concentration of Te dissolved in the molten alloys. This conclusion is supported by the experiments with undoped Fe-4.28C-0.25Si, which showed that H by itself promotes gray iron. Hence, the enhancement of the Te promotion of white growth by H is most likely due to an interaction of the H with the Te, as opposed to independent action of H.

REFERENCES

1. Dawson, J. V. AFS Trans., 1969, 77, 113.

2. Dawson, J. V. AFS Cast Metals Res. J., 1969, 5, 138.

3. Dawson, J. V. Foundry Trade J., Feb. 1970, 287.

4. Verhoeven, J. D.; Park, J. S.; Jones, L. L. Met. Trans., 1989, 20A, 1867.

5. Verhoeven, J. D.; Bevolo, A. J.; Park, J. S. Met. Trans., 1989, 20A, 1875.

6. Jones, L. L. M. S. Thesis, Iowa St. Univ., Iowa, U.S.A., 1985.

7. Magnin, P.; Kurz, W. MRS Symp. Proc., H. Fredricksson and M. Hillert eds., Elsevier Science Publ. Inc., New York, NY, 1985, 34, 263.

8. Carlberg, T.; Fredricksson, H. Solidification and Casting of Metals, TMS, London, 1979,115.

GENERAL DISCUSSION

The main objective of this study was to examine the influence of four impurities S, Te, O and H on structure control in the directional solidification of Fe-C-Si alloys. Solidification experiments consisted of two major parts; (1) Evaluation of the Te effect on the transition between gray and white structures, and (2) evaluation of the S effect on graphite morphology control in the gray solidification. In the course of the solidification experiments, it was also observed that control of the solidification atmosphere by either H_2 or O_2 gas had a substantial influence on the microstructure. Experiments were done under three atmospheres: Ar, Ar + 10% O_2 and Ar + 10% H_2. The primary effect of adding the hydrogen appears to be a lowering of the O activity in the melt. Hence, it is considered that the three atmospheres are providing three levels of O activity,

Atmosphere	Oxygen Activity
Ar + 10% H_2	Very low
Ar	low
Ar + 10% O_2	High

It is, of course, possible that the H atom could be playing some direct role in the action of the solidification reactions taking place at the freezing interface, but this effect will be assumed to be a negligible one.

Most experiments with the Te-doped alloys were carried out in the previous study and the results have been reported (1). The additional experiments here in the present study produced evidence that the enhanced effectiveness of Te at suppressing gray formation under a strong H influence is closely related to the reduced O activity. The major emphasis of this study was put on the microstructural evolution in gray solidification. In the directional solidification experiments, gray cast iron can be made to exhibit three primary graphite morphologies that are produced during coupled growth of the graphite and austenite phases:

1] Type A flakes

2] Type D flakes

3] Coral

Figures 1 and 2 show the quenched interface regions of type A and D graphite, respectively. Two important facts are to be noticed in Figs. 1 and 2. First, Fig. 2 shows that type D can grow at 1 um/s, which was the slowest growth rate possible in this study, thereby producing evidence that the formation of type D graphite is directly from the liquid on solidification. Because type D graphite is so fine, it had not been possible in the higher rate experiments to rule out the possibility that the graphite of type D was actually forming by a solid state reaction, i.e., by precipitation from a thin austenite layer just behind the growth front. The quench interface of Fig. 2b shows, however, that this is not the case in the experiment at 1 um/s. The fine white iron structure which must form from the liquid is seen to lie directly on the graphite phase, thereby proving that the graphite phase in type D does form directly from the liquid, as is generally thought to be the case. Secondly, the dramatic difference in the shape of the interface regions between type A and D graphite suggests that each of those structures may form following a different kinetic equation. This means that the functional relation between velocity V and spacing λ, $V=\Phi(\lambda)$, and the functional relation between velocity and undercooling ΔT at the growth front, $V=\Phi(\Delta T)$, both change from one morphology to the next. Since the change in graphite morphology is greatly influenced by the impurity elements, the kinetic equations may also have to be modified according to the action the impurity causes. In gray solidification, both Te and S induce type D graphite when the type A growth is terminated upon increasing the growth velocity. The Te, however, suppresses the type A growth, thereby pushing the D$\Rightarrow$A

Figure 1. Quenched interface region of type A structure growing at 1 um/s, solidification direction ⇑, 50X, as polished

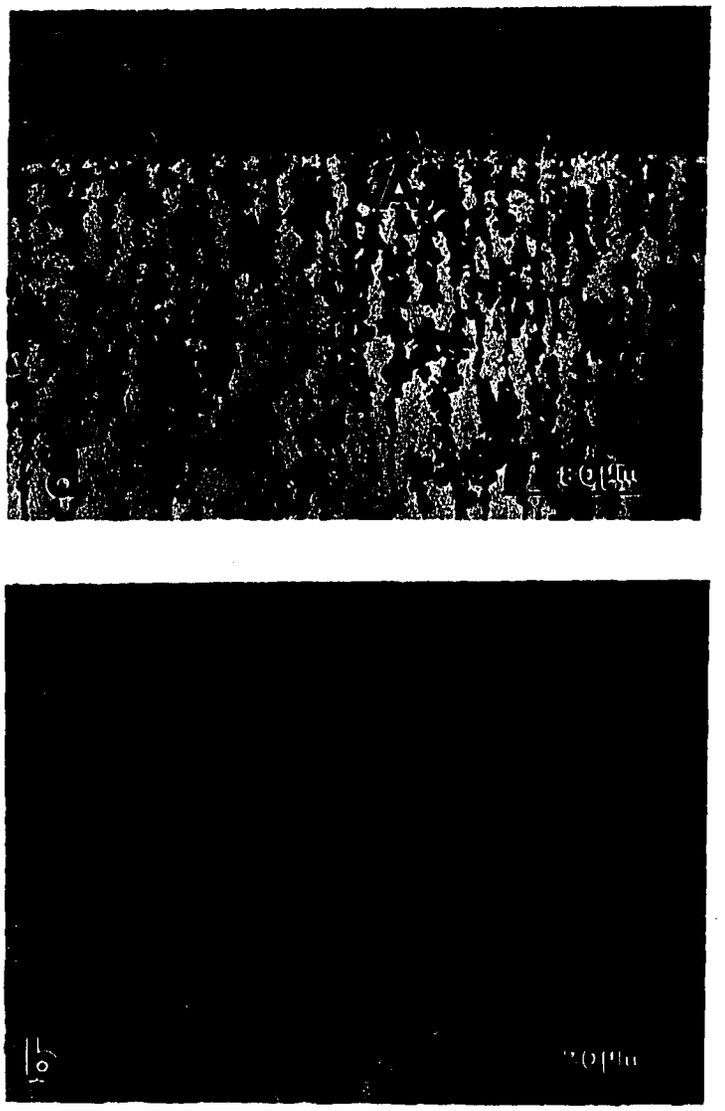

Figure 2. Quenched interface region of type D structure growing from Te-doped alloys at 1 um/s, solidification direction vertical, as polished, (a) 250X, (b) 1000X

transition down to an extremely low rate, while the S promotes the A formation at a higher rate. The H or O effect in gray solidification is most evident in high purity alloys with no S or Te doping. It is observed in high purity alloys that the transition in graphite morphology is from type A to coral, instead of type D, when the velocity is increased, regardless of the atmosphere control with either H_2 or O_2 gases. The H and O act in a manner opposing the effect caused by each other. The H encourages the A growth at a higher rate like the S but the O has an effect to suppress the type A formation like the Te, thereby reducing the transition velocity between A and coral graphite.

The most evident effect of the impurities observed in the gray solidification is, therefore, on the control of graphite morphologies and also on the transition velocities between them. At low growth velocities, around 1 um/s, the type A form appears, unless Te is added in a H_2 atmosphere. As the velocity is increased, transitions occur to other forms. In summary, the following transitions are observed:

1] A $\Rightarrow$ Coral

2] A $\Rightarrow$ D

3] A $\Rightarrow$ D $\Rightarrow$ White

The transition velocities have been measured under the same conditions of gradient and composition; gradient around 70°C/cm and composition of 3.4% C and 2% Si. In all cases the transition velocities have been found to be higher for the transition in the direction of arrow shown above (acceleration experiments) relative to the transition velocity in the opposite direction (starting with the phase on the right of the arrow and decelerating). This hysteresis in transition velocity (V_{tr}[acc] - V_{tr}[dec]) does not vary dramatically between the three transitions and, therefore, only the acceleration transition will be discussed.

Results with the high purity alloy

In the solidification of high purity alloys, only coral graphite is observed, i.e., only transition 1 with all three atmospheres. The atmosphere appears to control the transition velocity, V_{tr}, as illustrated in the following data.

Atmosphere	Oxygen Activity	V_{tr}
Ar + 10% H_2	Very low	20-50 um/s
Ar	low	2.5-5 um/s
Ar + 10% O_2	High	1-2.5 um/s

Two conclusions seem to be significant:

1] Increased O does not produce type D graphite (both S and Te do).

2] As the O activity drops the type A graphite can grow to higher rates.

This second conclusion is consistent with an effect on the kinetic equations as shown graphically in Fig. 3. The kinetic curves assume that structures which are able to grow at a higher solidification interface temperature for a given rate of solidification will protrude in front and crowd out the competing structures. There are, therefore, essentially two possibilities for the effect of the increased O upon these kinetic curves. The O is expected to make it more difficult for the growth to occur because of some type of adsorption effect so that increased O will cause the curves to move downward in order to provide more undercooling (and hence more free energy) for the growth processes at a given velocity. Hence, either the type A or the coral curve will move down more, depending on which one is most sensitive to the increased O level. If increased O moved the coral down more, V_{tr} would have to increase, just the opposite of what is found. Hence, it seems that the data require the increased O to lower the type A curve more than the coral curve. This means that the O increases the required undercooling at a given velocity more for the type A than for the coral.

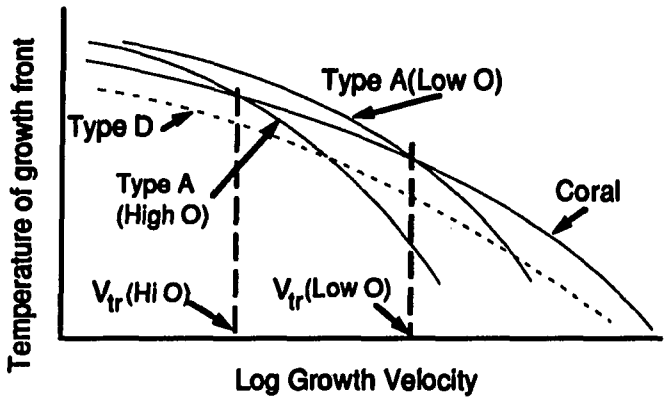

Figure 3. Relationship between growth temperature and growth velocity in high purity alloys. [V_{tr}: A⇒Coral transition velocity]

Results with S and Te doped alloys

When adding these elements it was found that the coral graphite no longer appears and in each case it is replaced by type D graphite. Apparently the coral mode is poisoned to the extent that the kinetic curve is lowered sufficiently that the alternate graphite form, type D, can grow at a significantly lower undercooling and it now can also grow at lower undercoolings than the type A at higher rates. The transition velocities from A to D are given in the following data.

Atmosphere	Oxygen Activity	V_{tr}(S added)	V_{tr}(Te added)
Ar + 10%H	Very low	50 um/s	< 1 um/s
Ar	low	50 um/s	$1 < V_{tr} < 4$ um/s
Ar + 10%O	High	20-50 um/s	-

It is seen that the S addition allows the type A morphology to grow to a significantly higher rate than the Te addition. In fact, the Te suppresses the type A formation even at the

slowest growth rate studied, 1 um/s, when under Ar + 10% H_2 atmosphere. Both elements must have an adverse effect upon the coral morphology, increasing the undercooling and moving its $T=\Phi(V)$ curve well down. From the Auger results, it was found that either S or Te adsorbs on the austenite/graphite interfaces of graphite flakes and therefore it is reasonable to assume that the kinetic curves are lowered over the conditions of the pure case. It is also known that the addition of Te promotes the formation of white structures at relatively low velocities but the S addition does not have this effect within the velocity range of this study. In order to explain these experimental results, the kinetic curves must be arranged similar to that shown in Fig. 4.

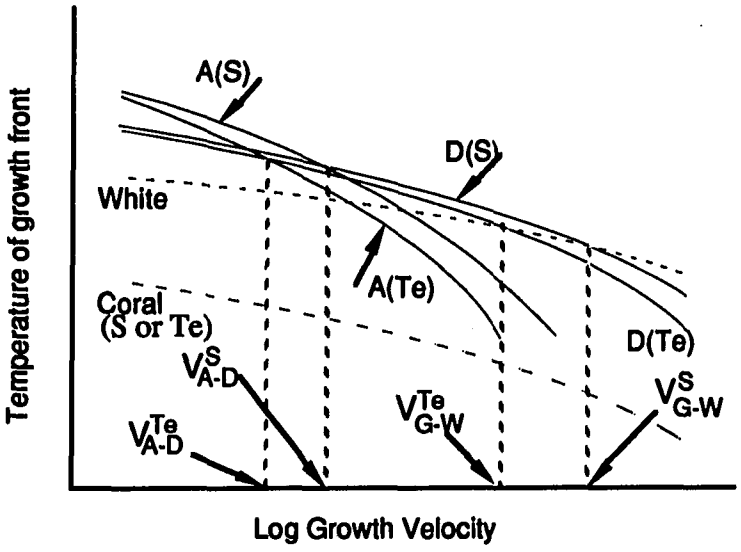

Figure 4. Relationship between growth temperature and growth velocity in gray (type A, D and Coral) and white structure. [S: S-added, Te: Te-added] [V_{A-D}: A⇒D transition velocity, V_{G-W}: G⇒W transition velocity]

In the present study, an attempt was made to figure out the mathematical functions describing the kinetic curves in Fig. 3 and 4 based on the eutectic growth model by Jackson

and Hunt (2) as modified by Magnin and Kurz (3). According to the eutectic growth model, the growth undercooling ΔT, the solidification rate V and the lamellar spacing λ are related by the relationship,

$$\Delta T = K_1 V\lambda + K_2/\lambda \qquad (1)$$

where K_1=function[m, C_o, f_α, f_β, D] and K_2=function[m, f_α, f_β, $(\Gamma\sin\theta)_\alpha$, $(\Gamma\sin\theta)_\beta$]. The variables in K_1 and K_2 have the same meaning as used by Magnin and Kurz (3). The modification of this model by Magnin and Kurz introduces a parameter ϕ which fixes the operating spacing λ as follows,

$$\lambda = \phi\lambda_{ex} \qquad (2)$$

where λ_{ex} is the spacing corresponding to the minimum in the ΔT-λ curve for a specific velocity V as shown in Fig. 5.

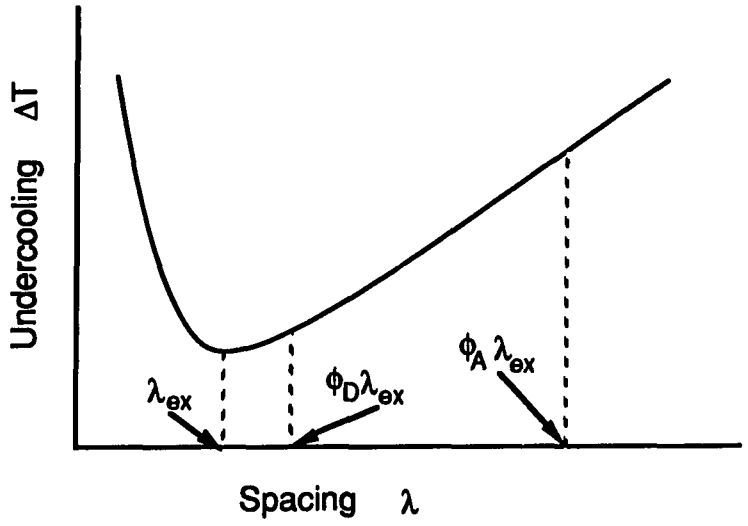

Figure 5. Relationship between undercooling and phase spacing according to the current model for irregular eutectic growth

At a given V, it is known that the type D will have λ much smaller than type A and therefore the situation should be as shown on Fig. 5 if both A and D follow the same

kinetic equation. This would require a larger ϕ value for type A, which is consistent with the experimentally observed fact that type A has much less branching than D, indicating that it is more difficult for the A to branch. A problem arises, however, when the experimental results previously obtained (1) are considered which show that the type D is undercooled about 15°C more than the type A. This means that the two morphologies cannot lie on the same curve as in Fig. 5. Therefore, in this study, the value of the constant K_2 was perturbed to see what would happen on the ΔT-λ curve. Only the constant K_2 was tested because of the expected effect of the impurity adsorption on the $\Gamma\sin\theta$ terms in K_2, whereas no significant effect is expected on the terms of K_1. The result is presented in Fig. 6 for two K_2 values differing by a factor of 5.

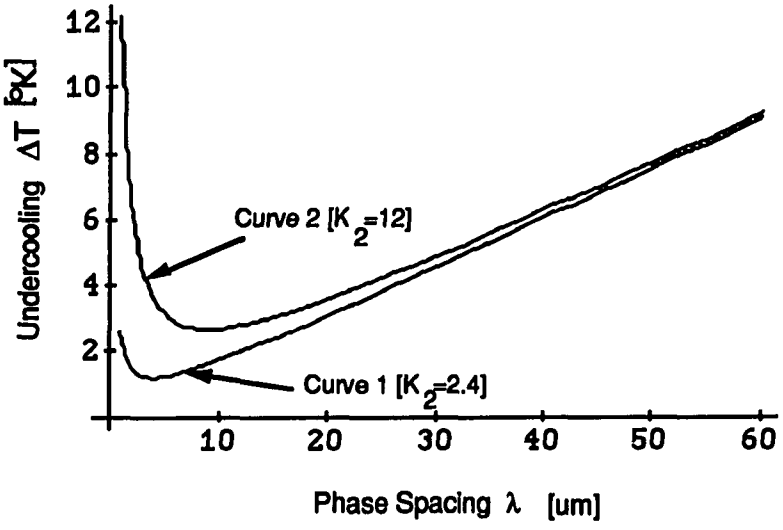

Figure 6. Undercooling versus phase spacing according to Equation (1) with K_1=0.15, V=1um/s and K_2=2.4 and 12 in Curve 1 and 2, respectively

The curve 1 is drawn for V=1um/s using the values suggested by Magnin and Kurz and the curve 2 is drawn in the same manner except for K_2. It can be seen that the two curves do not differ very much in the neighborhood of the operating range, $\lambda > \lambda_{ex}$. Since type D

graphite occurs only with the addition of S or Te and these elements are known to reduce the interface free energy, curve 1 in Fig. 6, which was drawn with smaller K_2 value, should apply to type D growth. This, however, gives rise to the same problem as raised in Fig. 5 with regard to the degree of undercooling. As shown in Fig. 6, curve 1, which is supposed to apply to type D growth, predicts less undercooling than curve 2 for type A growth for the observed cases of $\lambda_D < \lambda_A$, which is contrary to the experimental observation. This suggests that the growth behavior of both type A and D graphite cannot be fully explained by merely assigning different values for K_2 based on the currently available model for eutectic growth. The value of constant K_1 is seen to have a more pronounced effect on the ΔT-λ curve than K_2. But the material properties determining K_1 appear not to be much affected by the impurities which are responsible for the formation of type D structures and also for the change in the A$\Rightarrow$D transition velocities. The above arguments present evidence that the kinetic growth equation for type D graphite might be significantly different than for type A. Fredriksson and Wetterfall (4) have presented experimental data showing quenched growth interfaces where the flake graphite protrudes significantly ahead of the iron front. Both Jones(5) and Park(6) have also presented such evidence. Unfortunately, the evidence is not conclusive, because if a slight melting occurred just prior to quench, it would likely cause the graphite to protrude ahead of the iron. If, however, the graphite does protrude ahead of the iron, then the current model, as in Eqn. (1), could not be applicable and the type A structure would be expected to follow a different kinetic equation, which is also supported by the above arguments.

The very different morphologies of type A and D graphite also suggest that the two forms must follow different kinetic equations. In order to make comparison studies of type A and D graphite it is helpful to be able to grow both structures at the same rate. In addition, because type D is so fine, it is helpful to be able to grow it at the lowest possible

rates to produce the coarsest structures. It can be seen from Table 5, Part I, that using S doped alloys it should be possible to grow type A and D at growth rates of 10-20 um/s. However, as shown in Part IV, by the use of a combination of Te doping and a H_2 atmosphere the type A morphology can be suppressed sufficiently to allow the type D morphology to grow at rates as low as 1 um/s. Using this technique quenched growth fronts of type D graphite grown at 1 um/s have been produced in alloys containing both 3.93% C+1% Si and 3.4% C+2% Si. These morphologies appear essentially identical and Figs. 2 and 7 present typical photomicrographs. Figure 7a shows a longitudinal section of the type D morphology and Fig. 7b shows the transverse section. Figures 7 suggest that the D graphite constantly changes its growth direction with little difficulty, resulting in a plate-like graphite structure which appears to curl back and forth along the average growth direction and also at right angles to the growth direction. Figure 1 demonstrates that the graphite morphology of type A at the same growth rate, 1 um/s, in addition to being much thicker, is much more planar. Comparison of transverse sections in Fig. 7b and Fig. 4 in Part I shows that the type A graphite is close to a planar structure, while the ability of the type D graphite to curl produces a subdivision of the iron matrix into longitudinal cells. In Part III of this study, it is concluded that the freedom of type D graphite to change the growth direction is related to its extremely thin thickness plus the frequent fault formation. These large differences in the morphology of type D versus type A suggest that it is quite likely that the two forms would follow a different kinetic growth equation.

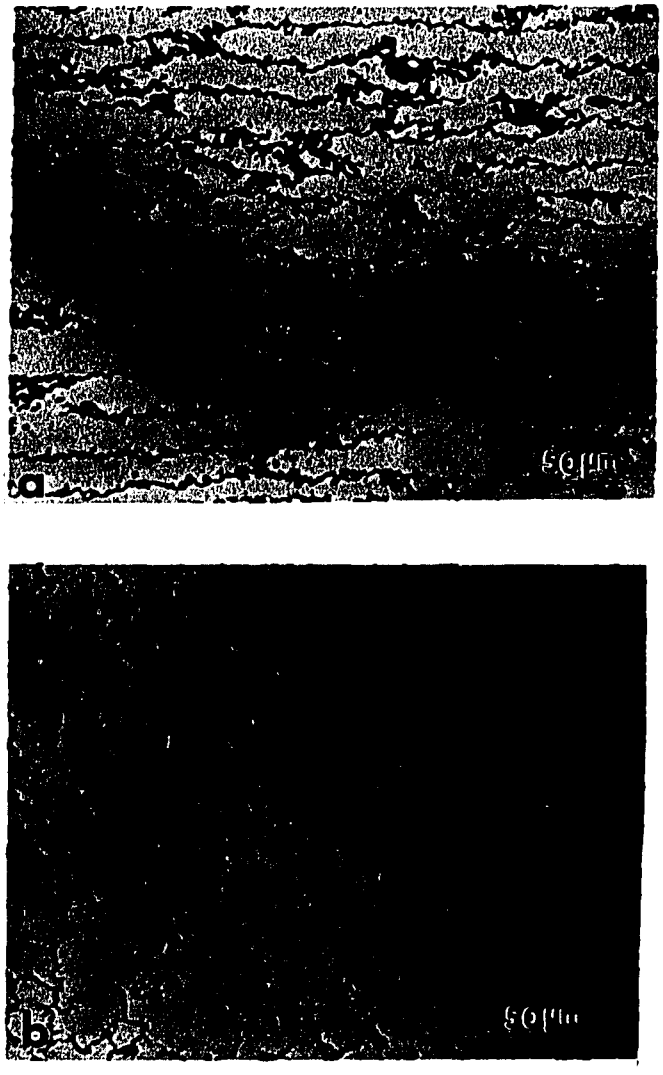

Figure 7. Optical micrograph of type D graphite grown from Te-doped alloys at 1 um/s, as polished, (a) longitudinal section, solidification direction to the left, 320X, (b) transverse section, 400X

Hillert and Subba Rao (7) has used two different growth models for type A and type D growth. The transition in graphite morphologies between A and D was experimentally verified in this study and others as well (7,8). The plate growth model, originally proposed by Zener (9), was used to simulate the coarse type A growth whereas the type D growth was described by the eutectic growth model which is similar to the modified Jackson and Hunt model. In both models, the relationship between growth temperature and velocity can be described by

$$T = T_E - aV^{1/2} \qquad (3)$$

where "a" is a constant differing in the two models and T_E is the equilibrium eutectic temperature. Equation (3), however, predicts that the type D growth always occurs at a higher temperature and dominates the solidification because the constant "a" for D growth is smaller than for A growth. In order to get the transition, Hillert took different values for T_E in Eqn. (3) between A and D growth. The resulting relationships between growth temperature and velocity is as shown in Fig. 8.

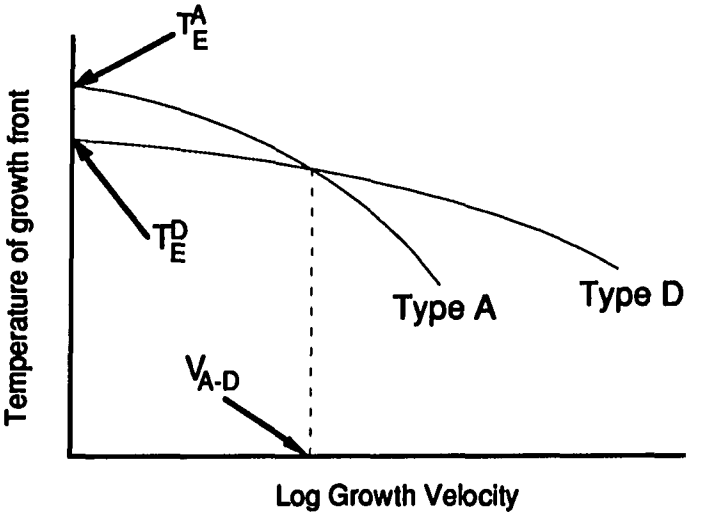

Figure 8. Growth temperature versus growth velocity in type A and D gray structure with different equilibrium eutectic temperatures, T_E^A for type A and T_E^D for type D

Although Fig. 8 predicts the A⇒D transition at the critical velocity, $V_{A\text{-}D}$, the assigning of different equilibrium temperatures for the two structures, A and D, which are almost identical except for the size and thickness of the graphite flakes, is yet to be justified.

In conclusion, it seems necessary that the current model for eutectic growth be further modified if it is to render an explanation of the experimental results with regard to the three different graphite morphologies occurring in cast iron solidification. Several problems of the current model recognized in this study can be summarized as follows:

1] The dramatic difference in the growth front shape between the graphite morphologies, as verified in Figs. 1 and 2, are not properly considered.

2] The effect of trace elements S, Te and O can only be incorporated into the currently accepted eutectic growth model through the $\Gamma\sin\theta$ terms. This approach is not sufficient to account for the dramatic changes in structure and transition velocities caused by the elements.

3] The model has been developed for the pure binary Fe-C system and therefore it does not take into account the probable influence caused by the ternary element Si which is present in a significant amount in alloys of this study and others.

Results of the Auger work

The Auger analysis was performed in Part II of this study to obtain experimental proofs which might be used to explain the mechanism by which the S and O caused the change in solidification microstructures. The Auger study was mainly concerned with the segregation of the elements S and O as observed on the iron/graphite interface regions of a directionally solidified sample. The major results are:

1] In course type A structures, the S lies on the broad faces and the O lies, in many cases, on a network of lines on the broad faces that appear to be graphite growth steps. The S is a monolayer thick and the O is a roughly 6~8 monolayer thick iron oxide.

2] In the thinnest type A structures, the S lies on the broad faces but no O is found. The S is a monolayer thick.

3] In the type D structures, the S lies on the broad face but no O is found and the S is a monolayer thick. (The same result as with the thinnest type A.)

4] In the commercial samples received from John Deere, the O is present on the type A interfaces even though the graphite thicknesses are thin relative to the case 1] and 2] above.

Before the significance of the Auger data can be evaluated, it is necessary to raise a fundamental question. Is the segregation pattern, as observed in the fracture sample, determined at the solidification front or during cooling in the solid state? In an attempt to resolve this question, previous studies (10,11) have been using a quenching technique to avoid the solid state diffusion. In cast iron, however, it was verified in this study that the martensitic phase transformation, induced on quenching into water or Ga-In eutectic, could lead to an erroneous conclusion either by crack formation or by opening up of the iron/graphite interfaces. The present study, therefore, used a milder air quenching to avoid the drastic phase transformation while achieving a moderately fast cooling rate down to the temperature regime where the diffusion rate is negligible. The segregation pattern of the samples thus prepared was qualitatively the same as that of the ordinary samples, both in type A and D graphite structure. Another important question is why the O is found in thick type A samples, along the steps in many cases, and not in the thin type A. There are three arguments:

1] The O is adsorbed on the growth steps of the graphite and this is why the $T=\Phi(V)$ curve for type A is lowered by high O as shown in Fig. 3. The Auger results showed that the degree of O adsorption was more extensive in high purity samples than in S-added samples and also that the interface regions of commercial type A samples consisted mostly of the O covered area, although the structure there was thinner than in the directionally solidified samples. Both phenomena suggest that the degree of O adsorption may inversely depend on the S content available in cast iron; the high purity samples had no S added and the commercial samples had other elements included which tied up the S in the form of sulfide particles, resulting in a lower S activity. The problem with this argument is, then, why the O is not observed on the thin type A samples of the directional solidification experiments, leading to the second argument.

2] The type A is a relatively thick piece of graphite and therefore there will be a significant difference in contraction on cooling across its thickness relative to the contraction in the surrounding iron. Since the linear thermal expansion coefficient of graphite along the "c" direction is about twice the value of matrix iron ($\alpha_{Fe} = \sim 10^{-5}$ cm/cm°C), it is possible that during cooling a gap might open up at the iron/graphite interface. If the oxygen potential in the atmosphere is high enough and also the temperature high enough, an iron oxide would form along the step. This view appears to be supported by the Auger results of the samples directionally solidified from S-added alloys. The O adsorption occurred only at the samples solidified at a low velocity, having coarse graphite structures. This theory is also consistent with the presence of the much thicker oxide than would be needed to just poison growth steps. On the other hand if this theory is correct, it is difficult to explain what is the mechanism for the O to lower the $T=\Phi(V)$ curve for type A.

3] The third possibility is associated with the crack formation even with the pearlite matrix due to the presence of the sharp tips of graphite flakes. During cooling, relatively large temperature gradients are present which can produce tensile stresses and the graphite tips will, then, produce stress concentrations and it is possible that cracks will form at the iron/graphite interfaces. The situation will become even worse if the sample has undergone the martensitic phase transformation because of the brittle martensite/retained austenite matrix. Once cracks are formed and create fresh surfaces, they may be contaminated by the O either present as an impurity in the quench operation, or when the samples were held in air before transfer to the Auger instrument, or when the samples were polished and etched to identify the interface position and evaluate the microstructures.

In an attempt to resolve the two important questions of the Auger results, a special experiment is planned for future study. The most important thing in the experiment is that we must be able to examine the segregation pattern right at the growing solid/liquid interface which has spent little time after solidification. Samples of type A (both coarse and fine) and type D graphite will be directionally solidified and quenched into air at the termination which provides a relatively fast cooling rate while avoiding the martensitic phase transformation. Auger fracture samples will be prepared from the sections containing quenched solid/liquid interfaces. A notch will be filed so that the fracture occurs along the longitudinal direction of a sample, thereby exposing the solid/quenched liquid interface region to be examined by Auger analysis. Initial work has shown that such an experiment produces a longitudinal fracture surface on which the growth front is clearly displayed. By analyzing the segregation variation starting directly on the growth front and moving away from it, more conclusive evidence will be obtained concerning the important question of whether the segregation observed in Auger analysis at locations away from the growth front reflects the segregation taking place on solidification at the growth front.

A second important question in the Auger analysis involves the presence of the O in type A graphite, i.e., does the observed O on the graphite interfaces originate in the solidification processing, or is it introduced on specimen handling after solidification. An experiment has been designed to answer this question, in which the specimen will be transferred to the Auger machine after solidification without having been exposed to an O environment. The experiments will do all specimen handling in a glove box and transfer the sample in sealed bags. The absence of O in these experiments will indicate that the O is introduced in the specimen handling because small microcracks are present at the iron/graphite interfaces in the solidified samples and these become contaminated, most probably in the etching step. The continued presence of O in these experiments will provide strong evidence that the O is forming in the solidification process.

Another effect the S or H causes on type A structure is the coarsening of intergraphite spacing, as can be verified in Figs. 4, Part I. Assuming the main effect of H is to reduce the O activity, these results mean that the space is coarsened by reduction of O and by addition of S. An important question here is why the S and O additions have an opposite effect on the graphite spacing. Before this question can be further considered the additional studies on the Auger analysis need to be completed in order to establish when and if O is being adsorbed on the iron/graphite interface.

GENERAL SUMMARY

Directional solidification studies have been carried out to examine the microstructural evolution in Fe-C-Si alloys. The structure was controlled either by small additions of Te and S or by control of the solidification atmosphere with H_2 or O_2 gases. In the directional solidification experiments, Fe-C-Si alloys can produce white or gray cast iron, and the gray iron can be made to exhibit three primary graphite morphologies, type A, D and coral graphite. The transitions between those structures were found to depend on the chemical composition and solidification velocity. This study utilized Auger electron microscopy to investigate the segregation pattern established on the iron/graphite interface, and also transmission electron microscopy to examine the planar defects present in flake graphite. The results of the present work can be summarized by the following conclusions.

1] The most evident effect of the impurities observed in the gray solidification is on the control of graphite morphologies and also on the transition velocities between them. The addition of either S or Te produces type D graphite as opposed to the coral graphite occurring in high purity alloys. The Te, however, suppresses the type A growth, thereby pushing The A⇔D transitions down to extremely low solidification rates, while the S moves the A⇔D transitions to higher solidification rates. Increased O or H in high purity alloys does not produce type D graphite but coral graphite still grows in an atmosphere of high O or H. The H, however, raises the A⇔coral transition solidification rates but the O suppresses the A⇔coral transition solidification rates. The relative changes in the kinetic growth equations of the various morphologies required by these transition rate changes have been discussed. It is concluded that current theoretical models are not adequate to explain the experimental results.

2] The Auger results show that the iron/graphite interface regions are contaminated by the adsorbed element S or O when the graphite grows in flake morphology, type A or

D, in both high purity alloys and S-added alloys. The O presence is, however, observed only in coarse type A graphite structure. Evidence is found that the O contamination can occur during cooling to room temperature, particularly in rapid quenching, and additional experiments are needed to find out when the O adsorption is occurring.

3] The TEM study has confirmed that both the type A and D graphite grow by the extension of basal growth layers. The thin type D flakes have been shown to have a much higher density of rotation stacking faults present between the basal layers compared to the thick type A flakes. In order to understand the curly nature of type D graphite as opposed to stiff planar type A graphite, it is needed in future study to look more carefully for twin defects in type D, especially in the D samples grown at 1 um/s which have a more well defined graphite structures.

4] Evidence is produced that the interaction of the H with Te, as opposed to independent action of H, is primarily responsible for the enhancement of Te effectiveness in promoting white iron growth.

REFERENCES

1. Verhoeven, J. D.; Park, J. S.; Jones, L. L. Met. Trans., 1989, 28A, 1867.

2. Jackson, K. A.; Hunt, J. D. Met. Trans., Aug., 1966, 236, 1129.

3. Magnin, P.; Kurz, W. Acta Met., 1987, 35, 1119.

4. Fredriksson, H.; Wetterfall, S. E. "The Metallurgy of Cast Iron", B. Lux et al. eds., Georgi, St. Saphorin, 1975, 277.

5. Jones, L. L. M. S. Dissertation, Iowa St. Univ., Iowa, U. S. A., 1985.

6. Park, J. S. M. S. Dissertation, Iowa St. Univ., Iowa, U. S. A., 1987.

7. Hillert, M.; Subba Rao, V. V. "The Solidification of Metals", ISI Publ. 110, 1967, 204.

8. Nieswaag, H.; Zuithoff, A. J. "The Metallurgy of Cast Iron", B. Lux et al. eds., Georgi, St. Saphorin, 1975, 327.

9. Zener, C. AIME Trans., 1946, 167, 550.

10. Johnson, W. C.; Smartt, H. B. Met. Trans. A, 1977, 8, 553.

11. Seah, M. P.; Hondros, E. D. Proc. R. Soc. Lond. A., 1973, 335, 191.

ACKNOWLEDGEMENTS

I thank my God for providing me with the power to finish this work which was beyond my ability.

I gratefully acknowledge my major professor, Dr. John D. Verhoeven, for his encouragement and guidance. He gave me a chance to continue the study in a situation where I almost had to give up and go back to my country without achieving my childhood dream. Particular thanks are due to Dr. Albert J. Bevolo for his kind cooperation in performing the painstaking Auger analysis. Special thanks are extended to the committee members, Dr. Rohit K. Trivedi, Dr. Scott Chumbley, Dr. John W Patterson Jr. and Dr. Mohan Singh Devgan. I am also indebted to Mr. Ed Gibson, L. L. Jones, L. Lincoln, F. Laab and H. Baker whose technical assistance was invaluable. I would like to thank Ken, Dan, Lee, Jeff, Kim, Yoo, Chuck and Han for their friendship.

Finally, I want to thank my parents and my brothers and sisters who have always supported me through prayer with many tears. Now I pray that I can be a good husband to my believing wife, Kim, and a good father to my son, Paul, who have suffered most during this work.

I am grateful to the John Deere Foundry, Waterloo, Iowa, for providing cast iron samples prepared form conventional casting. This work was funded by the office of Basic Energy Science of the United States Department of Energy (USDOE). It was performed at the Ames Laboratory, which is operated for the USDOE by Iowa State University under Contract No. W-7405-ENG-82.

APPENDIX

H-O interaction in molten Fe-C-Si Alloys

The experimental results of this study show that control of the solidification atmosphere with either H_2 or O_2 gas has a definite effect on the solidification microstructure. It turns out that the effect caused by one element is opposing the effect by the other in both gray and white solidification of Fe-C-Si alloys. In order for the gaseous elements in an atmosphere to have an influence on solidification, they must dissolve in the molten iron and be present in solution in the melt. The solubility of such diatomic gases as H_2, O_2, and N_2 in metals is always found experimentally to be proportional to the square root of the partial pressure of the gas in question, as long as its concentration in the solution is small (1). The square root dependency of solubility on pressure is an indication that the diatomic gases are present in atomic form when dissolved in solution according to reactions

$$H_{2(g)} = [H] + [H] \qquad (1)$$

$$O_{2(g)} = [O] + [O] \qquad (2)$$

For instance, the equilibrium constant of Eqn. (1) is given by

$$K = \frac{a_H^2}{P_{H_2}} \qquad (3)$$

For small concentrations of the dissolved H_2, its activity is proportional to the concentration so that Eqn. (3) may be written as

$$K = \frac{[\%H]^2}{P_{H_2}} \qquad (4)$$

Rearranging Eqn. (4) leads to the relationship

$$[\%H] = K\sqrt{P_{H_2}} \qquad (5)$$

which states that the quantity of H dissolving in a metal is proportional to the square root of the H_2 pressure outside the metal. Consequently, controlling the solidification atmosphere with either H_2 or O_2 gases provides a method of adjusting the atomic H or O concentration in the molten iron.

For the experiments of the present study, the major gaseous elements present in atmosphere beside the inert Ar may include H_2, O_2, CO, CO_2, and H_2O. The O_2 partial pressure can be determined by means of the equilibrium

$$H_2 + \frac{1}{2}O_2 = H_2O \qquad (6)$$

For Eqn. (6) the equilibrium constant K is given by

$$K = \frac{P_{H_2O}}{P_{H_2} P_{O_2}^{\frac{1}{2}}} \qquad (7)$$

and thus

$$P_{O_2} = \left(\frac{P_{H_2O}}{P_{H_2}}\right)^2 \frac{1}{K^2} \qquad (8)$$

At 1700°K, which is close to the furnace temperature 1450°C, $K = 5 \times 10^4$ (2). Substituting in Eqn. (8)

$$P_{O_2} = 4 \times 10^{-10} \left(\frac{P_{H_2O}}{P_{H_2}}\right)^2 \qquad (9)$$

The use of H_2 gases to increase the H_2 partial pressure in the atmosphere may thus significantly reduce the O_2 pressure by adjusting the $\frac{P_{H_2O}}{P_{H_2}}$ ratio in Eqn. (9). It can, therefore, be concluded that the H_2-rich atmosphere comes to raise the amount of [H] dissolving in molten iron at the expense of the reduced [O] concentration.

The fact that the effect caused by O in high purity alloys is substantially opposed by a strong H atmosphere suggests a possible H-O interaction present also in the molten cast iron. The interaction may contribute to the reduction of O activity which must be evident by the change in microstructure which was verified in this study. Concerning one of the possibilities of the H-O interaction, the increased H concentration in molten cast iron may have an effect on the O content through the following reaction,

$$[O] + 2[H] = H_2O_{(g)}. \qquad (10)$$

where the [] denotes the element present in atomic form in the melt and (g) the gaseous state. In dilute solution of [O] and [H], the equilibrium constant K for Eqn. (10) can be written as

$$K = \frac{P_{H_2O}}{[H]^2[O]} \qquad (11)$$

Equation (11) states that the high H activity in molten iron may greatly suppress the O activity, if the iron in contact with a gaseous atmosphere in which P_{H_2O} has a constant value. Epstein and coworkers (3) gave the relationship

$$\log K = \frac{10850}{T} - 8.01 \qquad (12)$$

to estimate the K value for Eqn. (11) if the P_{H_2O} is expressed in atm, [H] in ppm and [O] in wt. %. According to Eqn. (11), it is predicted that the formation of H_2O gases is inevitable as soon as the product $[H]^2[O]$ in the molten iron exceeds a definite value. The H_2O gas can be produced in two ways: (1) The [H] and [O] atoms can reach the outer surface by either diffusion or convection and react there to form H_2O molecules or (2) Gas bubbles may form in the liquid iron until the equilibrium set by Eqn. (11) is established. In either case, the O activity in the melt would be reduced. In this study, cavity formation was observed during the solidification, indicating that reactions such as represented by Eqn. (10) may be occurring somewhere in the melt. (Because of the high C content in Fe-C-Si

alloys, the bubble formation in this study may be largely due to the reaction [C] + [O] = $CO_{(g)}$, for which the equilibrium constant is written as $\log K = \frac{1168}{T} + 2.07$ in molten iron if [C] and [O] are in wt. % and CO in atm.) The most probable place for the bubble formation is, then, the interface between metal and Al_2O_3 containment tube or the solidification interface where the capillary pressure could be substantially reduced. This view is supported by the fact that probing of the melt with a small Al_2O_3 rod eliminated the cavity problems, most likely by providing the additional sites for the bubble formation which may reduce the degree of supersaturation of the melt with respect to the elements in question, i.e., [C] and [O] for CO gases and [H] and [O] for H_2O gases.

REFERENCES

1. Fast, J. D. "Interaction of Metals and Gases", Academic Press, New York and London, 1965, 121.

2. Fast, J. D. "Interaction of Metals and Gases", Academic Press, New York and London, 1965, 47.

3. Epstein, H.; Chipman, J.; Grant, N. J. Trans. AIME, 1957, 209, 597.